Spring 2015

Failure analysis of high performance ballistic fibers

Jennifer S. Spatola
Purdue University

PURDUE UNIVERSITY
GRADUATE SCHOOL
Thesis/Dissertation Acceptance

This is to certify that the thesis/dissertation prepared

By Jennifer S. Spatola

Entitled
FAILURE ANALYSIS OF HIGH PERFORMANCE BALLISTIC FIBERS

For the degree of Master of Science in Materials Science Engineering

Is approved by the final examining committee:

Weinong Wayne Chen
Chair

Carlos J. Martinez

Jeffrey P. Youngblood

Volkan Ortalan

To the best of my knowledge and as understood by the student in the Thesis/Dissertation Agreement, Publication Delay, and Certification Disclaimer (Graduate School Form 32), this thesis/dissertation adheres to the provisions of Purdue University's "Policy of Integrity in Research" and the use of copyright material.

Approved by Major Professor(s): Weinong Wayne Chen

Approved by: David Bahr 4/15/2015
Head of the Departmental Graduate Program Date

FAILURE ANALYSIS OF HIGH PERFORMANCE BALLISTIC FIBERS

A Thesis

Submitted to the Faculty

of

Purdue University

by

Jennifer S. Spatola

In Partial Fulfillment of the

Requirements for the Degree

of

Master of Science in Materials Science Engineering

May 2015

Purdue University

West Lafayette, Indiana

ACKNOWLEDGEMENTS

I would like to express my gratitude to:

Dr. Wayne Chen, for supporting me throughout my time here at Purdue, and for being very understanding of my limitations within the materials engineering field.

Matthew Hudspeth, for showing me how the experiments were done, and for the information regarding the tensile failure strength of the fibers, which was not my part of the research.

And…

My mom, for always being there.

TABLE OF CONTENTS

Page

LIST OF TABLES

LIST OF FIGURES

Figure Page

Appendix Figure

Appendix Figure Page

Appendix Figure Page

Appendix Figure Page

ABSTRACT

Spatola, Jennifer S., MSMSE. Purdue University, May 2015. Failure Analysis of High Performance Ballistic Fibers. Major Professor: Dr. Wayne Chen.

High performance fibers have a high tensile strength and modulus, good wear resistance, and a low density, making them ideal for applications in ballistic impact resistance, such as body armor. However, the observed ballistic performance of these fibers is much lower than the predicted values. Since the predictions assume only tensile stress failure, it is safe to assume that the stress state is affecting fiber performance. The purpose of this research was to determine if there are failure mode changes in the fiber fracture when transversely loaded by indenters of different shapes. An experimental design mimicking transverse impact was used to determine any such effects. Three different indenters were used: round, FSP, and razor blade. The indenter height was changed to change the angle of failure tested. Five high performance fibers were examined: Kevlar® KM2, Spectra® 130d, Dyneema® SK-62 and SK-76, and Zylon® 555. Failed fibers were analyzed using an SEM to determine failure mechanisms. The results show that the round and razor blade indenters produced a constant failure strain, as well as failure mechanisms independent of testing angle. The FSP indenter produced a decrease in failure strain as the angle increased. Fibrillation was the dominant failure mechanism at all angles for the round indenter, while through thickness shearing was the failure mechanism for the razor blade. The FSP indenter showed a transition from fibrillation at low angles to through thickness shearing at high angles, indicating that the round and razor blade indenters are extreme cases of the FSP indenter. The failure mechanisms observed with the FSP

indenter at various angles correlated with the experimental strain data obtained during fiber testing. This indicates that geometry of the indenter tip in compression is a contributing factor in lowering the failure strain of the high performance fibers. TEM analysis of the fiber failure mechanisms was also attempted, though without success.

CHAPTER 1. INTRODUCTION

1.1 Introduction

Body armor, such as bullet proof vests, clothing, and helmets, is an essential component in use within the military and law enforcement arenas. Lightweight armor is needed to retain ease of movement and speed in battle or other dangerous conditions. Modern body armor is composed of an impact resistant multiply fabric. This multiply fabric is made up of woven or knitted high performance polymer fibers [1], [2]. High velocity impact resistant, lightweight armor has been researched since WWII. Nylon was the dominate fiber used until 1972, when other, more effective high performance fibers replaced it. These fibers include aramid fibers, such as Kevlar® and Twaron®, ultra high molecular weight polyethylene, that is Dyneema® and Spectra®, and more recently PBO, commercially known as Zylon® [1]–[3].

The ballistic limit of the fabric used in body armor can be evaluated by determining the V_{50} value of the fabric; i.e. the minimum velocity required for projectile penetration to occur. Predictions of this V_{50} value have been determined through numerical modelling (using a 3-D computer recreation of what may occur during projectile impact) [4]–[6], as well as with analytical modelling (using mathematical equations) [2], [7], [8]. However, when compared with experimental results, these predicted V_{50} values are higher that what is observed during the experiment [2], [9], [10]. This means that there is a discrepancy in the predicted ballistic limit for armor and the actual ballistic limit observed during impact testing. One researcher showed discrepancies of at most 7% [9], while another reported a difference of at least 11% [11]. There must be some parameter not accounted for or an incorrect assumption that is affecting these observed results [11].

One such reason could be that the predicted values may assume that each fiber within the armor is perfect in structure, thus giving the maximum value possible. This means that there are no defects in the fiber; that is, everything is in alignment within the fiber, the fiber is perfectly uniform in thickness and length, etc., which is not realistic. This could explain why the predicted ballistic limit values are higher than the observed results [12].

Another reason may be that the fibers within the armor have different strengths, due to defects present in the fibers. Therefore, weaker fibers would break first, putting more stress on the stronger fibers, which leads to failure well before the predicted values [11].

It may also, be that there is some type of fiber stress not being accounted for, thus causing an increase in the predicted ballistic limit. This is a strong possibility, since most research focuses on the armor as a whole and lacks single fiber failure criteria [13]. Therefore, analysis of the individual high performance fibers is important to understand the performance of the ballistic fabric as a whole, and may help to explain the gap in the predicted and observed results. The research presented in this thesis will focus on that possibility, through the use of different projectile shapes and loading angles to determine the stress state effects on the failure of these high performance fibers.

CHAPTER 2. BACKGROUND

2.1 Background

High performance polymer fibers are characterized by high tensile strength, high energy absorption (the ability to absorb and spread out energy before failure occurs), and low weight. Examples include, poly (*p*-phenylene terephthalamide) fibers (Kevlar®), ultra high molecular weight polyethylene fibers (Dyneema® and Spectra®), and, more recently, poly (*p*-phenylene benzobisoxazole) fibers (Zylon®) [1], [3].

2.1.1 Poly (*p*-phenylene terephthalamide) Fibers

Poly (*p*-phenylene terephthalamide), or PPTA, consists of two benzene rings and two amide groups in the backbone of the molecule, as shown in Figure 1 below. Rotation of the molecule is limited due to the benzene rings within the molecular backbone, giving PPTA a very rigid structure. The para position of the amide groups on the benzene rings give PPTA its extended chain structure. This allows parallel alignment and sheet packing, giving PPTA a high tensile strength and modulus. The amide groups facilitate hydrogen bonding with adjacent PPTA chains, leading to efficient packing and high degree of crystallinity, as well as an efficient load transfer [14]–[16].

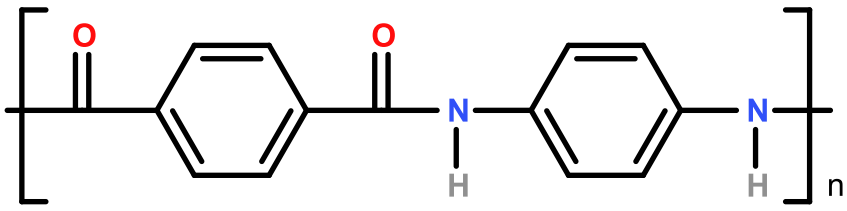

Figure 1: Molecular structure of PPTA.

The high crystallinity of PPTA is determined by how organized the molecular chains are within the fiber; i.e. how well the chains line up with each other. Figure 2a, shows a representation of what a crystalline region would look like: the molecular chains line up with one another to give a neat and ordered pattern. In Figure 2b, the chains are randomly aligned, in no particular pattern, thus giving a disordered appearance or an amorphous region.

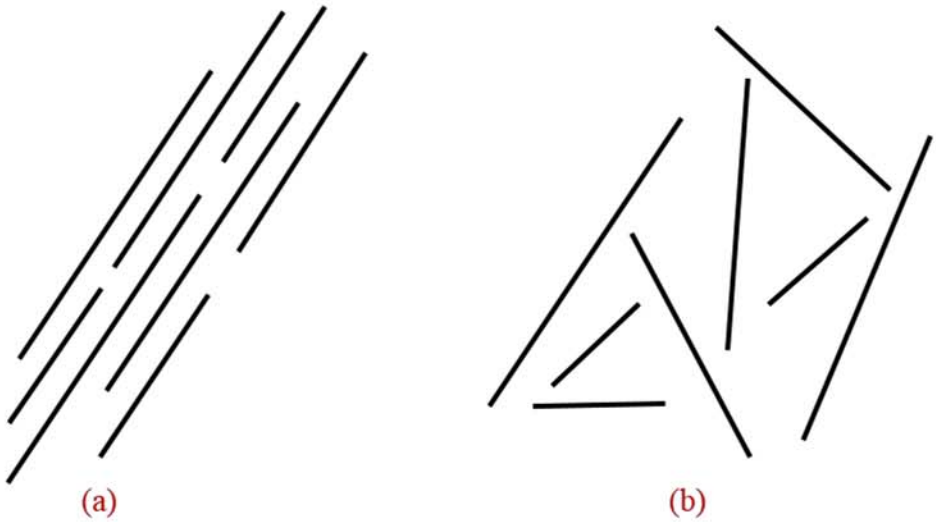

Figure 2: Schematics of a) crystalline region (molecular chain alignment) and b) amorphous region (random chain alignment).

PPTA fibers have a fibrillar skin-core structure (Figure 3). Each fibril consists of chains oriented along the fiber axis, connected to adjacent chains through hydrogen bonding and weak van der Waals forces. The skin is composed of uniformly oriented fibrils parallel to the fiber axis (Figure 3b), while the core has a radially oriented, pleated structure parallel to the fiber axis, which is the direction of chain orientation (Figures 3c and 3d). This pleated structure is comprised of rigid sheets formed by interlocking fibrils (fibrils connected by smaller tie-fibrils). These pleated sheets form in the hydrogen bonding plane, with each sheet component at an equal but opposite angle, creating the pleated look of the core.

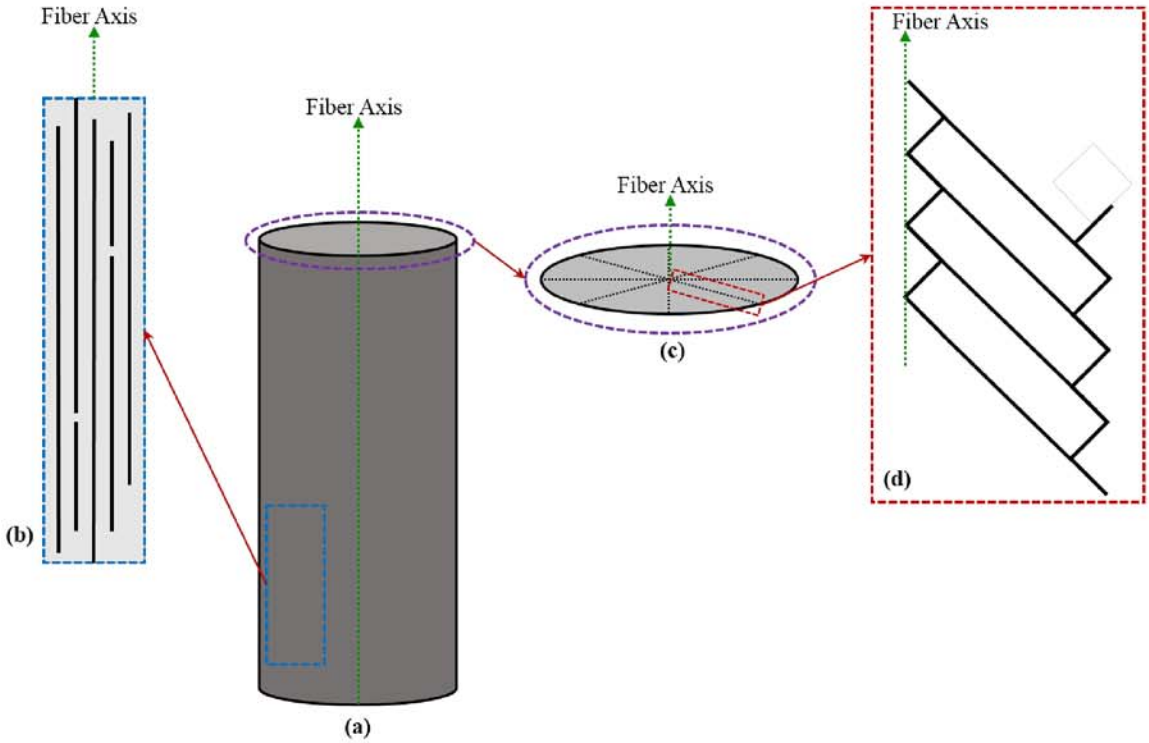

Figure 3: Schematic of: a) PPTA fiber, b) chain alignment of skin, c) radially oriented pleats within the core, and d) overview of the pleat structure within the core.

TEM dark field imaging shows that the pleated structure has a spacing of 500-600nm, interspaced with defect layers of 35nm. This defect layer is created by a rotation of the molecular chains within the fibril causing a decrease in the hydrogen bonding between adjacent chains, and therefore an imperfect alignment of those chains within the fibril. This causes some of the fibrils to be oriented differently than the rest, and as a result, creates the defect layer. Extended molecular chains span this defect layer, creating the high tensile modulus of PPTA[14]–[26]. However, it should be noted that defects caused by the imperfect alignment of fibrils produces interfibrillar stress, which lowers the tensile strength and can cause premature failure of the fiber [17]–[19], [22].

While PPTA fibers have a high tensile strength, they have a very low compressive strength, especially compared to other high performance fibers. This weak compressive strength is controlled by the lateral bonds within the fiber, i.e. the weak van der Waals forces and hydrogen bonds connecting fibrils together. Compression of the fiber initiates

a shear stress, causing narrow bands to form on the surface of the fiber at oblique angles to the fiber axis, or kink. This is due to a sudden change in the main chain direction in relation to the fiber axis. These kink bands form on the fiber surface and move inwards. Since the PPTA fibers consist of a rigid molecular chain structure, the kink bands contain completely separated blocks of chains, resulting in the loss of tensile strength, and eventually causing fiber failure [19], [21], [22].

During loop compression, once the single kink bands are uniformly distributed along the fiber, cross bands form. The wedge shaped area that occurs between the crossed kink bands allows for further fiber compression through the formation of larger kink bands. Further compression causes failure at the point of fiber extension as well as delamination, and propagates inward toward the original compressed section [19]. Axial compression causes massive lateral displacement of entire fiber segments, which follow the slip planes created by the hydrogen bonds. These segment displacements occur along the kink bands, are uniform in size, and at a constant angle. It should be noted that compressive stress failure is due to poor interfibrillar adhesion and not from bond breakage, i.e. failure due to poor lateral packing within the fiber, causing fibril splitting (breaking of the hydrogen bonds between molecular chains), not due to bond breakage within the molecular chains themselves [17], [19], [22].

The failure mechanisms of PPTA are: fibrillation (most common), pointed break, and transverse striation breaks. Fibrillation is a reduction in diameter of fibrils and the separation of fibrils along the longitudinal fiber axis. A pointed break has significant necking and a reduction in the fiber diameter, tapering at the fractured fiber end; attributed to the deformation of the crystalline phase. Transverse striation breaks are kink bands that occur due to misalignments of the molecular chains within the fibrils. These mechanisms are not strain-rate dependent, but do depend on fibril alignment within the fiber [24].

The properties of PPTA include: high tensile strength and modulus, high thermal stability, good impact resistance, and good chemical resistance. It has a higher tensile strength and modulus by weight than both glass and steel, making it a good lightweight alternative for these materials in industry [14], [19], [20], [23], [27]. For example PPTA is used in cables, fiber optics, helicopter blades, and structural components in aerospace applications, as well as for bullet proof vests [16], [17], [23], [28].

PPTA is made commercially by Teijin as Twaron®, and by DuPont under the name of Kevlar® [6], [22], [24], [25]. Since Kevlar® is studied within this research, it will be the focus of the rest of this discussion. There are multiple versions of Kevlar®, differing in crystallinity and how aligned the crystalline structures are, such as Kevlar® 29, 49, 119, and 149. These differences produce fibers with different mechanical properties, as shown in Table 1, below [24], [25]. Kevlar® 29 has a crystallinity of 80-85%, while Kevlar® 49 and 149 have a crystallinity of 90-95% [24]. In Kevlar® 29, 49, and 119 not all of the chains line up symmetrically; some have a cis conformation, reducing the number of hydrogen bonds between adjacent chains. However, Kevlar® 149 has a perfect alignment between the chains. This allows for more hydrogen bonds, causing greater crystal growth and a larger crystal size within the fiber [25].

Table 1: Various mechanical properties for different types of Kevlar®[24], [25], [29].

Kevlar® Fiber	**Crystallinity (%)**	**Chain Alignment**	**Specific Density (g/cm^3)**	**Tensile Modulus (GPa)**	**Elongation at Break (%)**	**Decomp. Temp. in Air (°C)**
29	80-85	Imperfect	1.44	78	3.1	427-482
49	90-95	Imperfect	1.44	113	2.47	427-482
119		Imperfect	1.44	61	4.1	427-482
149	90-95	Perfect	1.44	138	1.5	427-482

2.1.2 Ultra High Molecular Weight Polyethylene Fibers

Ultra high molecular weight polyethylene, also known as ultra high strength polyethylene and high performance polyethylene, is a thermoplastic homopolymer composed of linear high density polyethylene (Figure 4), with a molecular weight of at least 3 million [12],

[24], [30]–[39]. Ultra high molecular weight polyethylene abbreviations include: HMPE, HPPE, UHMWPE, and UHSPE, the latter of which will be used throughout the rest of this thesis. UHSPE has a high level of crystallinity (85% or more) and is composed of fully extended chains oriented along the fiber axis. This leads to its high level of crystalline orientation (more than 95%), creating a very anisotropic crystalline structure, and gives UHSPE its high tensile strength and modulus [24], [30]–[37], [40].

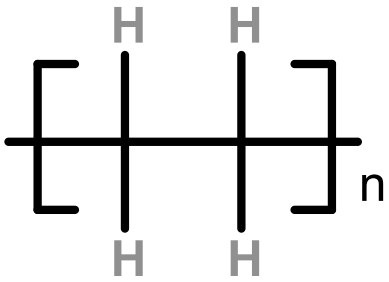

Figure 4: Molecular structure of UHSPE.

UHSPE fibers are uniform and fibrillar in nature and are produced through gel spinning [24], [30]–[34], [36], [41]–[43]. The drawing speed of the fibers determines the structure the fibers have. If they are drawn at a low speed, such as 10 m/min, they will have a skin-core structure, comprised of a thick skin of shish-kebab structures and a stacked lamellae crystal core. In these fibers, the shish-kebab structures have a negative effect on the mechanical properties, such as poor tensile strength. If UHSPE fibers are drawn at a high speed (100 m/min) they will have a thin skin and thick core structure, homogeneously made up of shish-kebab structures aligned parallel to the fiber axis. In this type of fiber, the shish-kebab structure has a positive effect on the mechanical properties, and is generally the way UHSPE fibers are produced [33], [41]–[43]. Therefore, the structure of UHSPE fibers is considered to comprise of a thin skin and thicker core homogeneously composed of shish-kebab structures (Figure 5). In the skin, the size of the shish-kebabs is smaller laterally than in the core, and consist of an interlocking structure (Figure 5a). In the core, the shish-kebabs are isolated and spaced roughly equidistant from each other (Figure 5b) [33], [43].

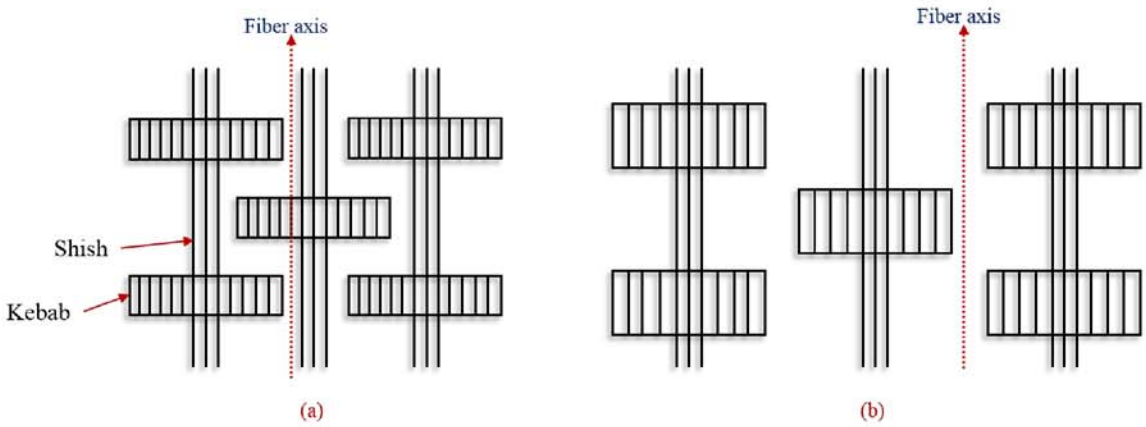

Figure 5: UHSPE shish-kebab structure for the (a) skin and (b) core.

This shish-kebab structure is the origin of the fibrillar morphology of UHSPE, as well as the high tensile strength. The fibrils are created by the transformation of kebabs to shishs, parallel to the fiber axis, as shown in Figure 6 [43], [44]. As the draw ratio increases, the lateral size of the shish-kebabs decrease. This is due to kebabs transforming into extended chains and then being incorporated into the shishs, through interchain slippage. Once there are only shishs left (kebabs extremely small), the fibrillar structure of UHSPE can be discerned [43]. This transformation of kebabs to shishs extends the length of the shishs, allowing the fibrils to stretch, and contributes to the high tensile strength of UHSPE fibers [24], [43].

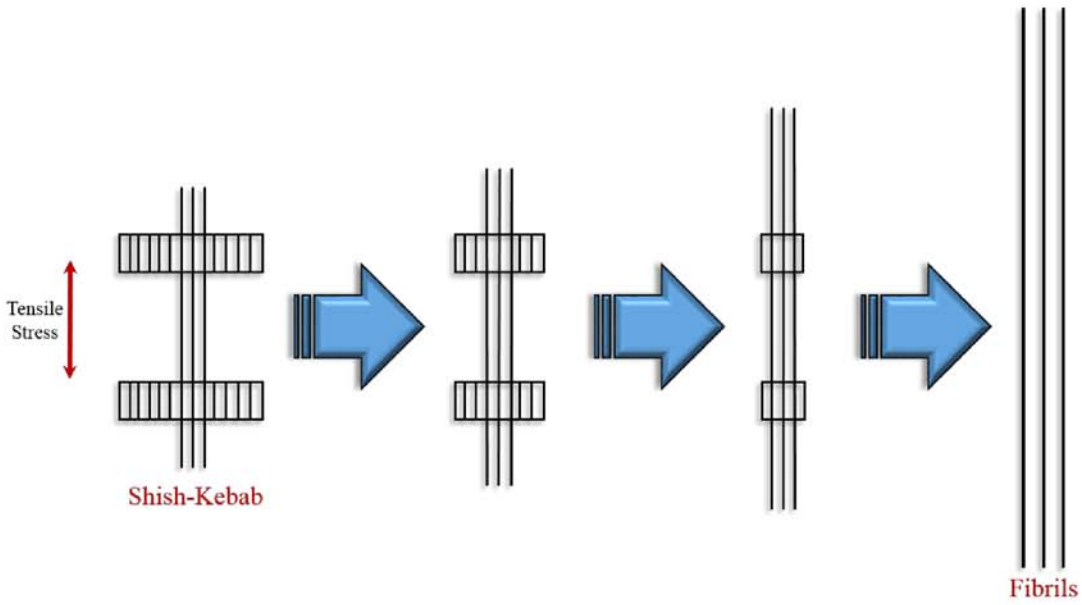

Figure 6: Fibril formation within UHSPE.

The failure mechanisms within UHSPE are dependent on the strain-rate [24], [45]. These mechanism are plate formation, fibrillation, and crazing. Plate formation occurs due to slippage between the crystalline regions of the fiber caused by weak interfibrillar bond adhesion at low strain rates. Fibrillation is the separation of fibrils lengthwise along the fiber, and is seen prominently at low strain rate and, to a lesser extent, at high strain rates as well. Crazing is surface cracking, and is only seen at high strain rates [24]. Within UHSPE fibers, the skin is the main determining factor in failure; cracks begin at the skin and propagate until fiber failure [33], [41]–[43]. In this thesis, only fibrillation was observed in the UHSPE fibers; no plate formation or crazing.

The properties of UHSPE include: high impact toughness, even at low temperatures, high abrasion resistance, low density, cyclic fatigue and radiation resistance, as well as good chemical and corrosion resistance [30], [32], [37], [39], [46]. These properties allow it to be used in a variety of ways including: mechanical components, such as gears [46]; biomedical applications for hip, knee, and shoulder joints [30], [38], [39], [47], [48]; truck beds [39]; FDA and Kosher approved food surfaces [30], [39]; and ballistic applications, such as body armor [37], [48], [49].

UHSPE has a very high tensile strength and modulus when compared with other polymer fibers, especially PPTA [24], [30], [40], [50]. Recently its tensile strength was recorded at 7Gpa, with a tensile modulus of 230GPa [12]. In the past, however the average tensile strength and modulus were about 5GPa and 200GPa, respectively [31]. It has a low density of 0.97 g/cm^3, much lighter than PPTA (1.44 g/cm^3) [45].

UHSPE is manufactured commercially by DSM, in the Netherlands, and by Honeywell (formally AlliedSignal Corporation), in the United States. DSM produces UHSPE under the name Dyneema® and has various versions denoted by SK## following Dyneema®. Honeywell produces UHSPE under the name of Spectra® [24], [31], [34], [36], [37].

2.1.3 Poly (*p*-phenylene benzobisoxazole) Fibers

Recently developed by Dow Chemical Company, poly (*p*-phenylene benzobisoxazole), also called PBO, is a rigid-rod polymer that packs laterally into crystallized polymer chains, allowing for a high degree of orientation parallel to the fiber axis [34], [51]–[53] (Figure 7). PBO is commercially produced as Zylon®, by the Toyobo Company of Osaka, Japan [10], [34] and is the strongest commercial synthetic polymer fiber available, as it requires more energy than PPTA and UHSPE to break [3], [34], [52]. It has a high tensile strength of 5.6GPa, which is three times greater than the strongest steel (piano wire), with only one-fifth the weight, and a high tensile modulus of 350GPa [2], [34], [51], [54]. These excellent tensile properties are determined by the covalent bonds in the backbone of the PBO molecule, since that is the direction of the tensile stress [55]. This makes it an optimal fiber for use in lightweight body armor.

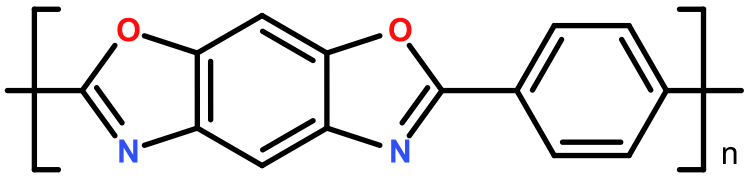

Figure 7: Molecular structure of PBO.

Other properties include: good abrasion resistance, excellent thermal stability as well as a very good solvent resistance [34], [51], [54]. Unfortunately, PBO has a poor resistance to moisture, radiation, and UV light [34], [53], [56], [57]. It also has a higher density than PPTA and UHSPE, which may deter its use in applications where weight is an important factor. While PBO has excellent tensile properties, it has poor compressive properties and fails for the same reasons PPTA does, poor interfibrillar adhesion from weak Van der Waals forces and hydrogen bonding [17], [34], [55]. A comparison of mechanical properties of the high performance fibers mentioned above and steel is below in Table 2.

Table 2: Comparison of mechanical properties of various types of Kevlar®, Dyneema® SK-76, Zylon® 555 and steel [5], [13], [25], [29], [31], [34].

	Density (g/cm3)	**Tensile Strength (GPa)**	**Tensile Modulus (GPa)**	**Elongation at Break (%)**
Kevlar® 29	1.44	2.58	78	3.1
Kevlar® 49	1.44	3.6-4.1	113	2.47
Kevlar® 119	1.44	2.96	61	4.1
Kevlar® 149	1.47	3.4	138	1.5
Kevlar® KM2	1.44	3.88	84.62	
Dyneema® SK-76	0.97	~5	~200	
Zylon® 555	1.54	5.8	180	3.5
Steel	7.8	2.8	200	1.4

Despite the good tensile properties of PBO, PBO body armor has performance and durability problems. In 2003, this issue was brought to the attention of the National Institute of Justice (NIJ), a department within the Department of Justice that conducts objective evaluations of materials/products. There were three separate incidents of bullet penetration of Second Chance Ultima® armor, composed of Zylon® fibers, harming the police officers wearing this armor. The first reported incident occurred in Forest Hills, Pennsylvania, and caused serious injury to the police officer. The other two reported incidents caused serious injury and death [58], [59].

It was determined that the massive reductions in tensile strength were caused by a severe reduction in molar mass. This molar mass reduction is due to chain scission from

hydrolysis; that is molecular chain breakage caused by water. Therefore, the more moisture in the environment, the greater the degradation of the molecular structure, and the lower the tensile strength [56], [57].

2.1.4 Previous Research on High Performance Fibers

Over the years high performance polymer fibers have be analyzed with various tests and for different purposes. Research on the general structural makeup of these fibers were performed with SAXS/WAXD machines to determine any structural changes (crystalline and amorphous region) during deformation, as well as crystalline orientation within fibrils, through the use of x-ray diffraction patterns [20], [25], [51], [54], [60]. An atomic force microscope was used to glean three dimensional, real space information on the internal structure of Kevlar® on a nanometer scale [23]. Transmission electron microscopes (TEM), using high resolution and dark field imaging as well as electron diffraction techniques were used to gain structural information, such as the skin and core structural makeup in UHSPE and the pleat periodicity within the core of PPTA [33], [36], [41]–[43], [61], [62]. Scanning electron microscopes (SEM) were used to measure the fiber and fibril diameter, and to look at surface damage, such as kink bands, after stress testing [12], [19], [44]. Finally, Raman spectroscopy was used to determine local stress distributions within the fiber during fiber pull, by measuring C-C bond stretching (changes in the Raman spectrum peaks) [31].

The stress-strain relationship to the failure of high performance polymer fibers was also researched. Findings determined that failure occurred as a result of intramolecular (interfibrillar) failure and that the crystalline orientation within the fibers affected the strength (higher stress resistance in direction of orientation) [12], [18], [35], [45]. The modification of high performance fibers to change mechanical properties, such as tensile modulus and residual strength, was also researched [17], [25], [37], [38], [47]. For example, UHSPE was annealed for various periods of time to determine how temperature/time affects the tensile modulus of the fiber; the modulus goes down as the time at that temperature increases. Results indicated that UHSPE can be used below

70°C for an extensive period of time, but can only for 7 hours between 70-100°C [37]. Also, the effect of the projectile's temperature on the energy absorption ability of UHSPE fibers in armor during impact was researched. Results indicated that the temperature affects only a small area around the projectile/fiber interface, which is dissipated quickly, and that there is no effect on the energy absorbing capabilities of the fabric, since most of the energy is absorbed by the fibers away from the impact region [50].

Ballistic impact research on these fibers is limited. Some of this research includes determining the effect of ballistic impact on different types of woven fabric using numerical modeling software, such as LS-DYNA, and experimental comparison [1]–[3], [5], [6], [48]. A marginal, if any, amount of research has been done on the ballistic impact on individual fibers to determine V_{50} and energy requirement for failure. In this research, it was determined that approximately 130J is required for failure of PPTA fibers, while 160J was needed for UHSPE fibers [40].

While there are numerous articles on the structure of high performance fibers, there is very little, by comparison, on the failure of single fibers during high velocity impact [11], [24], [45]. Most of the high velocity impact research focuses on fabric or cloth, and how the type of weave or knit affects the impact response [1]–[3], [6]. For example, Tran, et al. determined that the knit fabric had the worst impact resistance, while a the basket weave fabric showed the best resistance [6]. The little research done on single fiber failure during high velocity impact does not adequately address the gap between the predicted values and the lower observed values. This single fiber research assumed that the high performance fibers fail only in tension and have no other loading effects [13], [63]. Walker and Chocron, believed that fiber bounce was responsible for the observed decrease in performance from the predicted value, though this model also assumes pure tension failure in fibers [11].

Research is currently being conducted to determine if there are local stress concentration effects on the fiber in the absence of wave mechanics, in order to determine if fiber

bounce is the cause of the discrepancy between the predicted value and observed value, as postulated by Walker and Chocron in their 2011 article. Preliminary results show that fiber bounce is not responsible for the gap, but that there are local stress concentrations, produced during impact, that cause fiber failure to occur at a lower value than predicted [13], [63]. More research on the impact response of single fibers as well as the reasons behind the failure of high performance fibers during impact needs to be pursued.

2.2 Scope of Thesis

Research was conducted with high performance ballistic fibers to determine if the projectile geometry and/or the loading angle has any effect on local stress concentrations in the fiber at impact. In simpler terms: to determine if the shape of the projectile and/or the angle created at the fiber/indenter interface during impact affects the failure of the fiber.

The objective of this thesis is to analyze the failure mechanisms of high performance ballistic fibers to determine if projectile geometry and/or the angle created during the impact affects fiber failure. Specifically, Kevlar® KM2, Dyneema® SK-76, and Zylon®555 fibers are analyzed in thesis.

Chapter 3 is comprised of the experimental design as well as the procedures used during the testing and analysis of the fibers.

Chapter 4 contains a brief overview of the data results gathered from fiber testing conducted to determine failure strain as a function of angle.

Chapter 5 analyzes, compares, and discusses the fiber failure mechanisms observed using a scanning electron microscope.

Chapter 6 discusses the attempt to use transmission electron microcopy to analyze failure mechanisms of the high performance fibers.

Chapter 7 discusses possible future work that could be built upon this research.

CHAPTER 3. EXPERIMENT

3.1 Experimental Purpose

This experimental design created a geometric condition identical to transverse impact, but without the high rate of impact. The purpose of this design was two-fold: 1) determine the effects of projectile shape on the failure of high performance fibers, through the use of different types of indenters; 2) understand the effect of local stress concentrations that develop around the projectiles during transverse impact on high performance fiber failure, by varying the angle between the indenter and fiber, as well as observing any changes in the failure mode.

This experimental design was conducted in a two part research study. Part I focused on the failure strain values associated indenter geometry and angle of impact of high performance fibers during transverse impact. Part II analyzed the failure mechanisms observed in the failed fibers from Part I. A brief description of Part I is given below, though Part II is the main focus of this thesis.

3.2 Experimental Setup

3.2.1 Part I

In this part, Kevlar® KM2, Spectra® 130d, Dyneema® SK-62 and SK-76, and Zylon ® 555 were used for the failure strain analysis. Fibers were carefully removed from the fiber bundles, by isolating a single fiber and very carefully sliding it out lengthwise from

the bundle. The single fiber was then placed in the loading device. This device is capable of producing various deflection angles. To alter the angle of failure, either the starting height of the indenter or the placement of the fiber gripping mechanisms (the outer parts of the device) are changed. To reduce the possibility of slippage, carbon tape was used within the gripping mechanisms. These mechanisms use a 2kN pneumatic grip, or bollard, type system that is customarily used in longitudinal fiber tests (Figure 8).

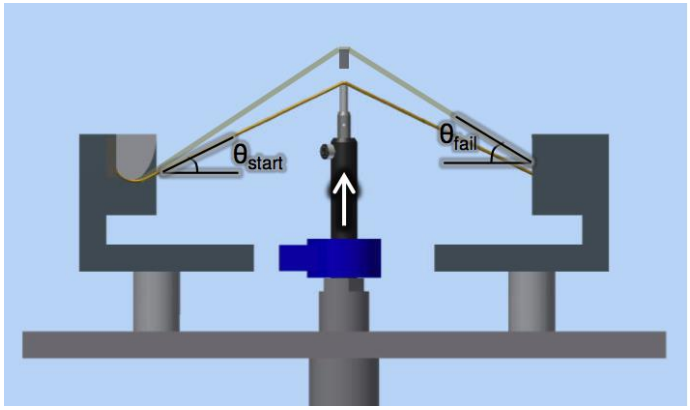

Figure 8: Schematic of experimental setup [13].

Three indenter shapes were used: 0.30 caliber round head, with a radius of curvature of 3.8mm; 0.30 caliber fragment simulating projectile (FSP), with a radius of curvature of ~20µm; and a high carbon steel razor blade with a radius of curvature of ~2.3µm (Figure 9). The razor blade was changed out for each test run, to minimize any blade dulling effects that might occur. Five different angles were tested (10^o, 20^o, 30^o, 40^o, and 50^o) by increasing the starting height of the indenter [13].

Figure 9: Indenters used in experimental testing. From left to right: FSP, round, and razor blade [13].

The controlled vertical displacement of the indenter was measured by an 810 Material Testing System (MTS), while the vertical load produced on the indenter was measured with a force transducer (Interface 1500ASK-25). An oscilloscope (Tektronix DPO4032) at a frequency of 250Hz, simultaneously tracked both signals and recorded them on a computer.

Displacement data was used to determine failure strain of the high performance fiber, by utilizing computer design software, such as Matlab, and the known geometries of the experimental setup.

3.2.2 Part II

Each failed fiber sample, was put in a sample bag and labeled. There were a total of eight test runs for each indenter at each angle tested for all types of fibers. Fracture surfaces from Kevlar® KM2, Dyneema® SK-76, and Zylon® 555 were imaged by a scanning electron microscope (SEM) to better understand the failure mechanisms observed in the fibers.

To prepare the fibers for viewing in the SEM, the fractured ends of each fiber were attached to an aluminum base using cyanoacrylate (superglue), at a point away from the

failed end (Figure 10). Once the superglue had dried, the samples were coated in a thin layer of gold using a SPI sputter coater, in an effort to reduce any charging effects that may occur within the SEM and damage the sample. A Hitachi s-4800 SEM was used with an accelerating voltage of 10kV. If charging occurred, the accelerating voltage was reduced to 5kV. At least three fractured fiber ends, from different test runs, were used from each fiber type. This gave a total of 135 fractured fiber ends imaged.

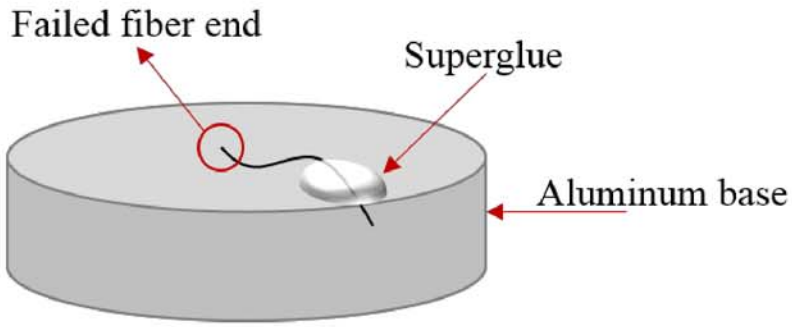

Figure 10: Prepared SEM sample.

CHAPTER 4. PART I RESULTS

4.1 Strain Data

For the round indenter tests, the failure strain was very similar to pure longitudinal tensile stress testing. This indicates that angle change has no effect on the failure of the fibers when the projectile is round. This is not surprising since its radius of curvature is quite large, and angle change would not make any significant difference in the local stress concentration at the fiber/indenter interface [13].

For the razor blade indenter tests, there was a severe reduction in failure strain, though the values were similar for all testing angles. This is due to the extreme stress concentration at the indenter face, caused by its very small radius of curvature, and is thus unaffected by angle change.

However, for the FSP indenter there was a decrease in failure strain as the angle between the indenter and fiber increased. At a high angle (50^o), the failure strain was similar to the razor blade, while at the low angle (10^o), the failure strain was similar to the round indenter (Figure 11). However, in Figure 11c, only the 10^o razor blade data for Zylon® 555 fibers is shown, due to fiber breakage during the loading process. This shows that the stress concentration developed at the contact site is affected by angle. It should be noted that with FSP indenters, failure always occurs at one of the indenter corners, due to the corner creating a localized stress concentration within the fiber. For FSP indenter testing, results showed than the SK-76 and Zylon®555 fibers had a failure strain greater than KM2 (Figure 12).

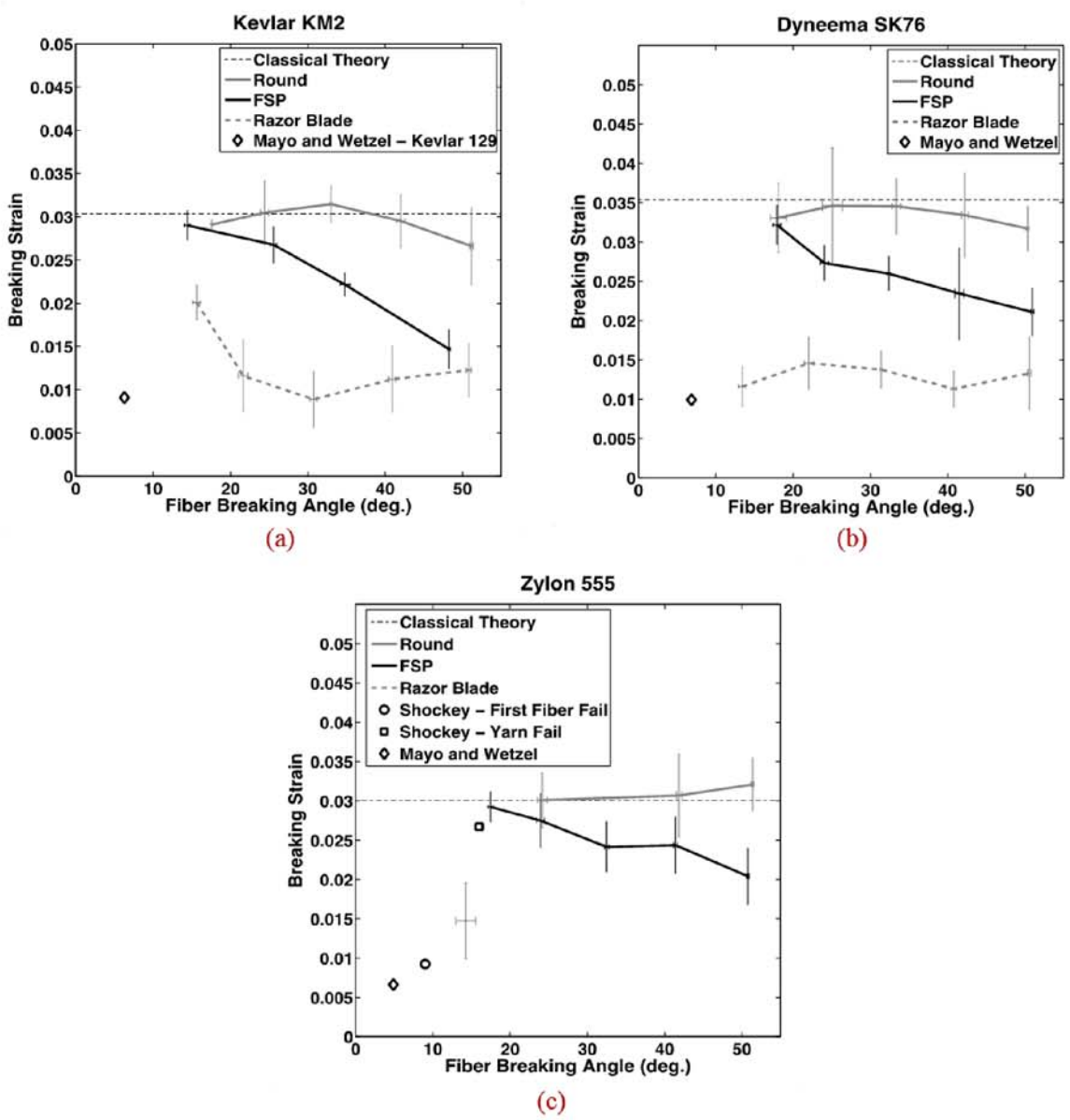

Figure 11: Failure strain as a function of angle for a) Kevlar® KM2, b) Dyneema® SK-76, and c) Zylon® 555 [13].

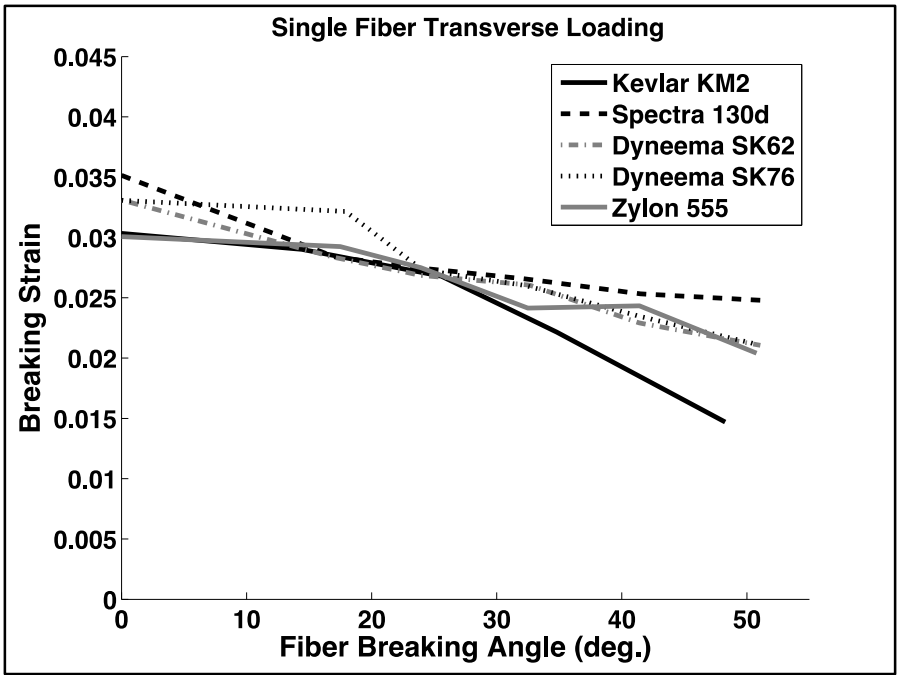

Figure 12: Failure strain as a function of angle comparison for all fiber types using the FSP indenter [13].

CHAPTER 5. SEM FAILURE MODE ANALYSIS AND DISCUSSION

5.1 Overview of Fiber Failure

This section analyzes the observed failures in Kevlar® KM2, Dyneema® SK-76, and Zylon®555, through the use of a SEM. To reduce clutter and keep this thesis flowing, the majority of the images used for the failure analysis can be found in the Appendix, as well as a more detailed analysis of the fiber failure.

Overall, it was observed that the razor blade produced through thickness shearing, while the round indenter produced fibrillation in all fiber types, regardless of the angle tested. It was also determined that in general the FSP indenter produced a transition from fibrillation, at low angles, to through thickness shearing, at high angles, for all fiber types.

5.2 Fiber Failure Analysis

For both KM2 and SK-76 fibers, the round indenter failure mechanism is fibrillation dominant, which is the typical failure mechanism for these fibers in tension. The razor blade indenter failure mechanism shows localized failure in the form of through thickness shear, or "cut" look. This shear failure occurs as a result of the very small radius of curvature of the razor blade compared to the diameter of the fiber, causing a highly localized stress concentration to develop at the fiber/indenter interface. These mechanisms are consistent for all angles tested, indicating that there should be no change in strain values due to angle change. However, the overall failure strain values for the razor blade indenter should be much lower than round indenter, due to the high stress

concentration at the fiber/indenter interface. This correlates with the strain data obtained in Part I, indicating that the results are correct (Figure 13).

Since the FSP indenter caused a decrease in failure strain as the angle was increased, some type of failure mode change within the KM2 and SK-76 fibers is expected. This is confirmed in Figure 14, shown below. At low angles fibrillation dominates in both KM2 and SK-76, similar to the round indenter. As the angle is increased the failure mechanism transitions to a "cut" look indicative of local shearing, as seen in the razor blade indenter. This transition indicates that there must be a local stress concentration around the contact boundary of the fiber and indenter, i.e. the fiber/indenter interface. The failure mechanism results for KM2 and SK-76 (Figure 14) correlate with the experimental strain data from Part I, as shown in Figure 13a and 13b, respectively. The round indenter produced only fibrillation, regardless of angle change, therefore no strain change occurs. The razor blade produced through thickness shearing for all angles testing, therefore constant strain at a lower strain value occurs.

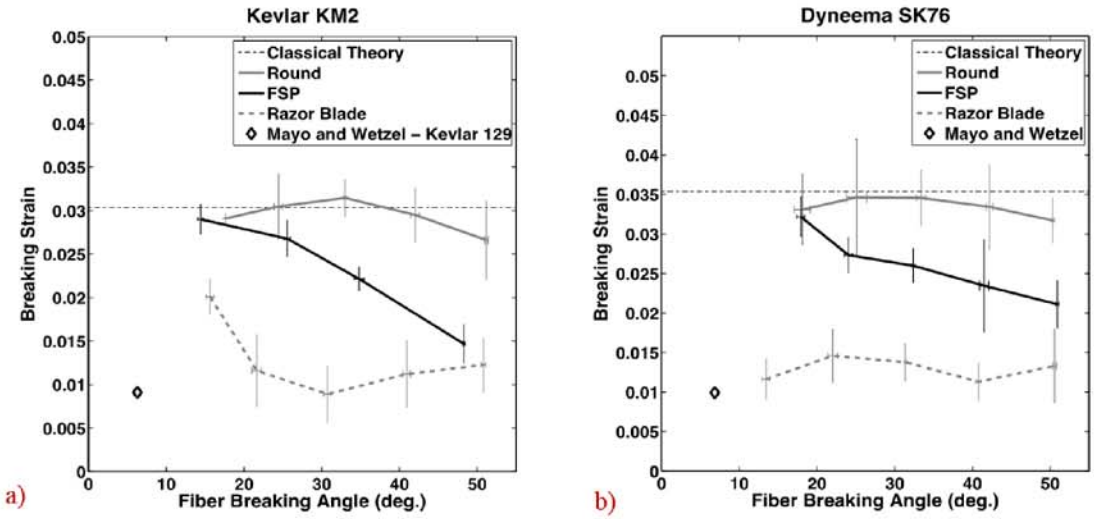

Figure 13: Failure strain as a function of angle for a) Kevlar® KM2 and b) Dyneema SK-76 [13].

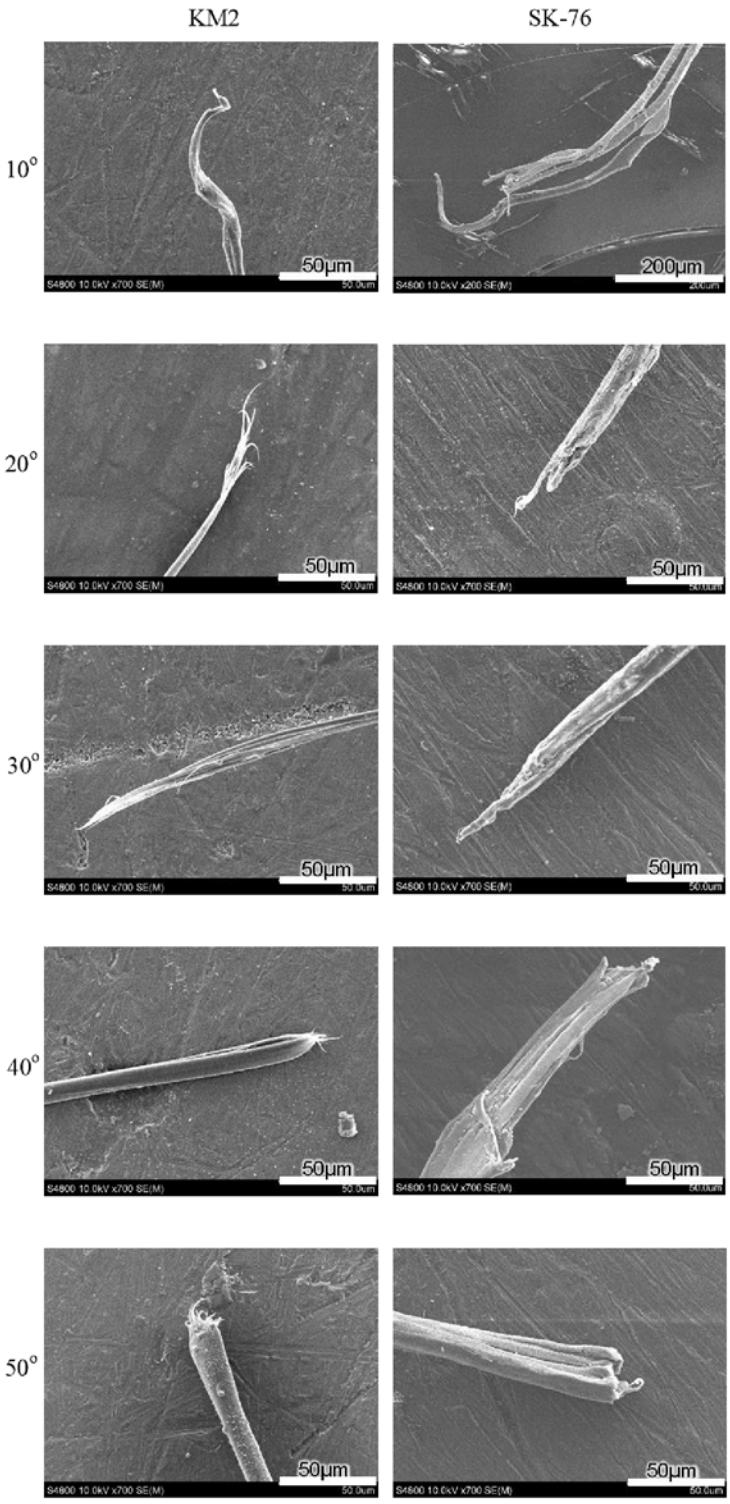

Figure 14: SEM images of the FSP failure mechanism transition for Kevlar® KM2 and Dyneema® SK-76 at all testing angles.

For FSP indenter testing, the fiber always fails at the corner of the FSP indenter. The FSP corner has a small radius of curvature compared to the diameter of the fiber and thus creates a highly localized stress concentration at the fiber/indenter corner interface. In other words, the indenter is only touching a small amount of the surface area of the fiber, concentrating the stress within that area. This significantly affects the failure strain of the fiber, as well as the failure mechanism present, especially at high angles; lower angles offer more surface area to interface with, like the round indenter, and therefore have a higher strain value, while higher angles have the least amount of surface area available, like the razor blade indenter, and a much lower strain value. This indicates that the failure mechanisms may not be dependent on the indenter geometry, since this failure transition is not seen with the round and razor blade indenters. Instead these failure mechanisms may depend on the geometry created by transverse wave propagation during transverse impact. The FSP indenter produced failure changes from fibrillation at low angles to shearing at high angles, shown in Figures 15 and 16; accordingly the strain values decrease with increasing angle, as shown in Figure 12 and 13.

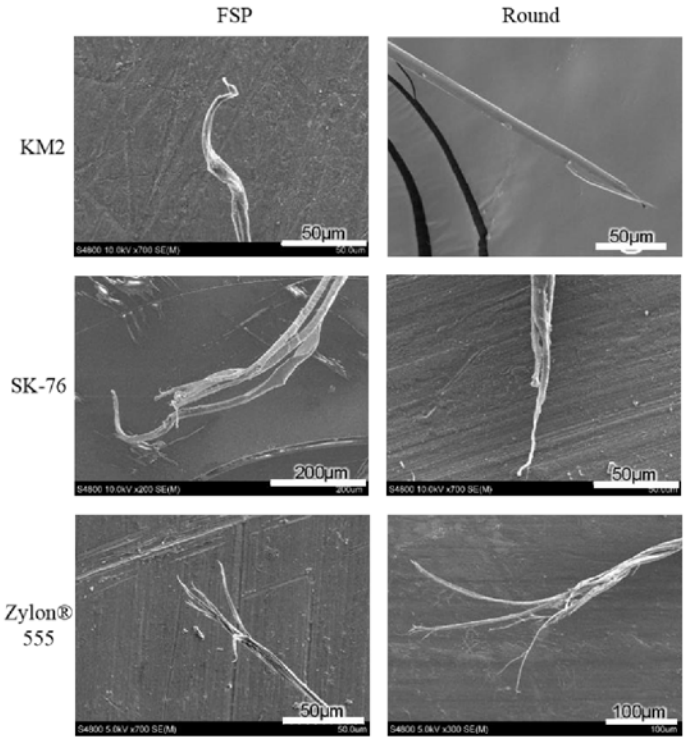

Figure 15: SEM images comparing FSP and round indenter failure mechanisms at 10° for Kevlar® KM2, Dyneema® SK-76, and Zylon® 555.

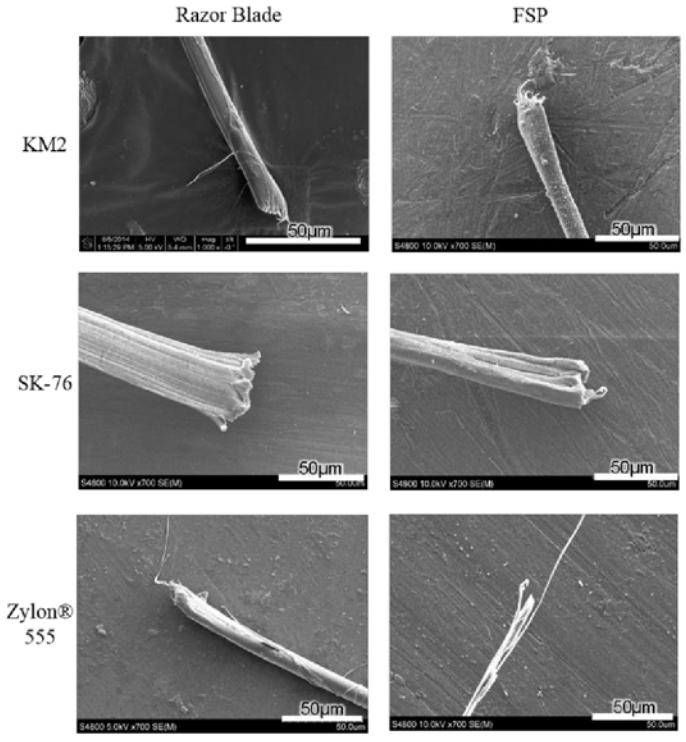

Figure 16: SEM images comparing FSP and razor blade indenter failure mechanisms at 50° for Kevlar® KM2, Dyneema® SK-76, and Zylon® 555.

Based off the failure strain data from the previous section, the similarity of PBO failure to PPTA, as well as the failure mechanism correlation between KM2 and SK-76, one would expect Zylon® 555 to exhibit similar fiber failure mechanisms as Kevlar® KM2 for each indenter.

However, this was not entirely the case. For failure with the round indenter, fibrillation was still seen, though the severity of it decreased as the angle increased. For the razor blade indenter, shear failure was the predominant mechanism, with some fibrillation present, but to a lesser extent than the round indenter. As the angle increased, the cut look became more pronounced, the number of fibrils decreased, until at the high angle just one thin fibril present within the cut look.

The FSP indenter produced a transition somewhat similar to that in KM2 and SK-76: at low angles, failure is similar to the round indenter; at high angles, it is similar to the razor blade (Figure 17). However, in the 30^{o} sample, massive amounts of fibrillation occurred, more so than in the 10^{o} samples, where fibrillation is expected to dominate. This is an inconsistency within the failure mechanism transition trend, especially since the other angles follow this transition. It can also be seen in this figure that the 50^{o} angle fiber, while having the cut look with tiny fibril, also has a fractured appearance, which is not seen in the razor blade failure mechanisms (see Figure 16).

However, it should be noted that the SEM imaging of these Zylon® 555 fibers revealed inconsistencies between the fibers, even with the same indenter and angle. For example, using the FSP indenter at 10^{o} produced varying degrees of fibrillation, though still extensive. Therefore, the rule of majority was applied to these results; i.e. whatever type of failure was present for most of the fibers imaged, is what the results are.

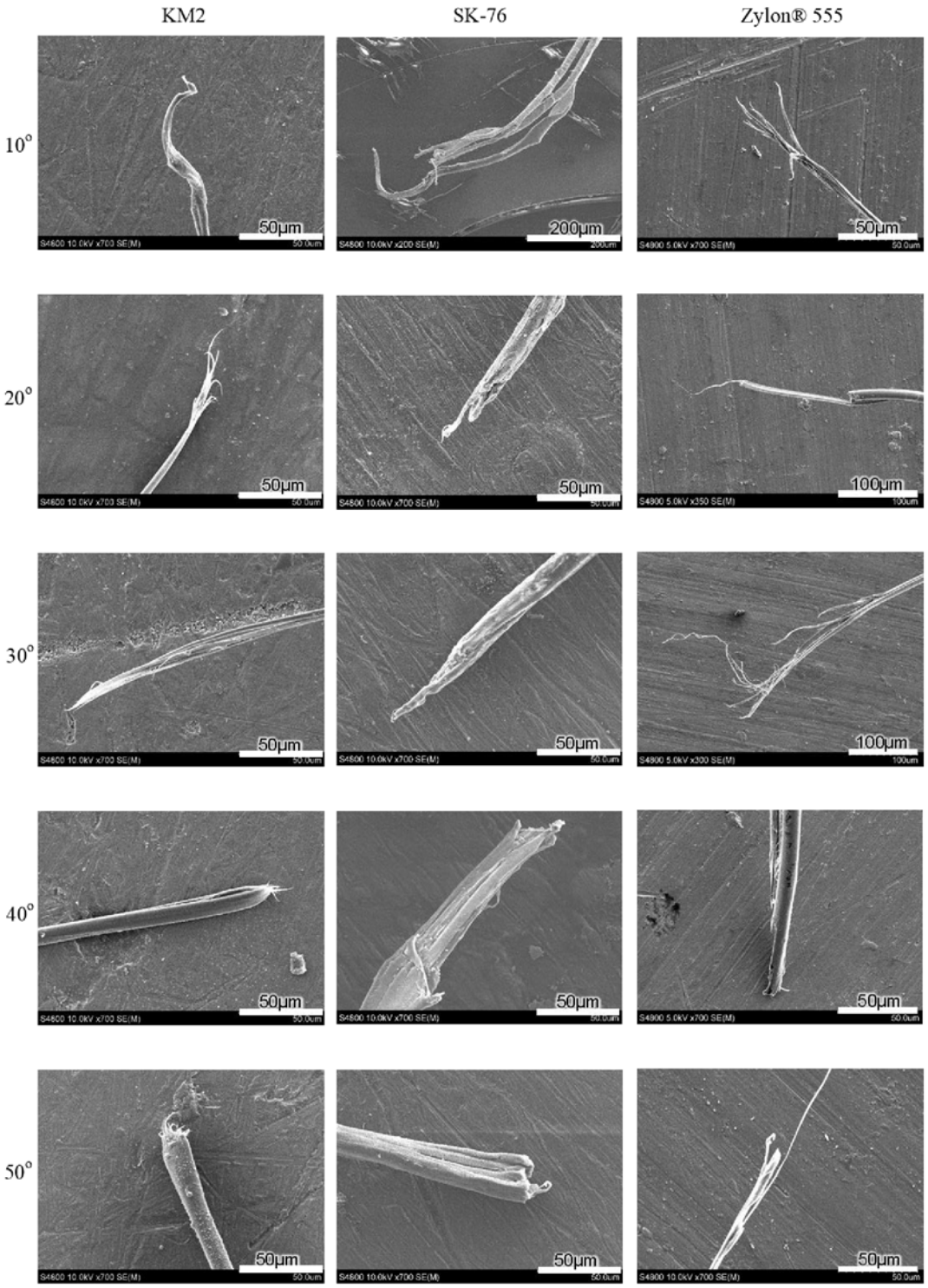

Figure 17: SEM images comparing failure mechanism transition from low to high angles for Kevlar® KM2, Dyneema® SK-76, and Zylon® 555.

There are many possible reasons for the differences in FSP indenter failure mechanisms between Zylon® 555 and both KM2 and SK-76, as compared in Figure 17. One reason is that the angle created by the FSP corner at the Zylon® 555 fiber/indenter interface (Figure 18) is greater than the ones created on the KM2 and SK-76 fibers. This causes a smaller stress concentration at the contact site than in the KM2/SK-76 fibers, and therefore only partial shear occurs. This may explain the part cut/part fibrillation of the Zylon® 555 fibers at 20^o and 40^o, but the total and massive fibrillation at 30^o is inconsistent with this explanation, as well as with the rest of the research in general.

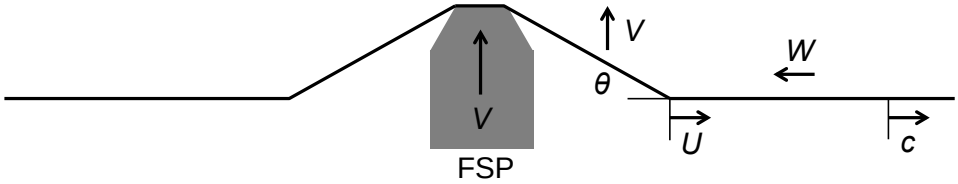

Figure 18: Schematic of the transverse impact on a fiber of an FSP indenter [13].

Also, there may be something about the molecular structure of PBO that affects the failure. For example, PBO has a stronger molecular chain backbone (greater rigidity) than PPTA and USHPE, which allow for greater crystalline alignment. This could lead to higher failure strain values. However, this explanation may not be likely for this type of testing as it has similar interfibrillar adhesion to PPTA (hydrogen bonding between chains to form sheets and therefore fibrils) and therefore performs poorly under compression, like PPTA.

The poor moisture resistance of PBO, may also be the cause of the inconsistencies observed in this research. The molecular degradation, or chain scission, that occurs as a result of water in the air may cause premature failure, as well as varying degrees of degradation within the fibers. Each fiber may have been exposed to different amounts of moisture depending on where in the original fiber bundle it was, therefore causing the inconsistencies seen, even within the same degree and indenter. This seems like the probable culprit, as previous research has shown decreasing tensile strength as a result of contact with moisture from the environment [56], [57].

It should be noted that the failure mechanisms observed in Zylon® 555, correlate well with the experimental strain data provided from Part I, in Figure 19 below, despite the inconsistencies observed within the Zylon® 555 fiber tests, and only the 10° razor blade data. Also, based on the overall trend in Zylon® 555, the razor blade data would be expected to drop, similar to the data of the KM2 and SK-76 from Figure 13. As shown in Figure 15, the low angle FSP indenter strain corresponds with the round indenter values; the same for high angle FSP indenter and razor blade strain values (Figure 16). At 30°, where massive fibrillation occurs, there is a jump downward in value. This is unexpected since there is a more fibrillation present than at 10° and a jump up in value would be assumed. However, the general trend is a reduction in failure strain, consistent with the transition seen from fibrillation to through thickness shearing. This is similar to the trend seen in KM2 and SK-76, and indicates that the testing method and failure mechanisms observed are correct (Figure 12 and 17). There must be a reason outside of the actual testing method for the inconsistencies observed during the failure analysis.

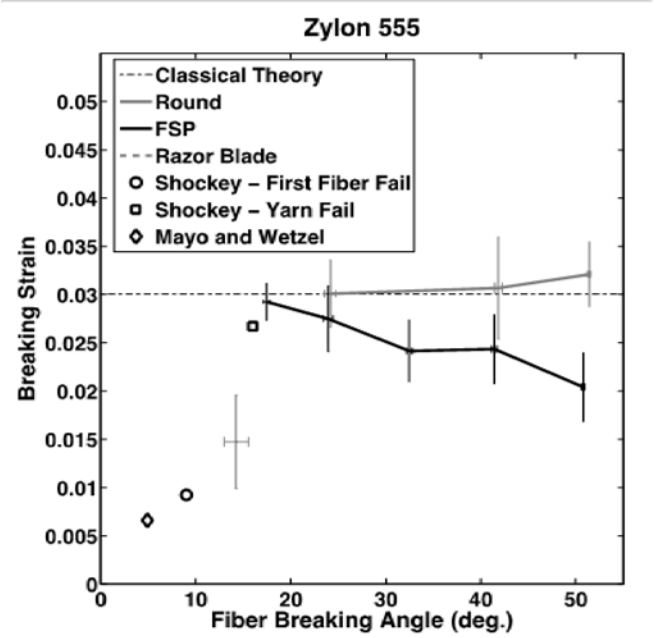

Figure 19: Failure strain as a function of angle for Zylon® 555 [13].

Testing error, or the accidental mistakes occurring during the testing and analysis of the fibers, is such a reason, especially since inconsistencies exist even within the same

indenter/angle test. One such error is accidental fiber pre-stress: the fiber had a stress applied before the test run, thus changing how the fiber will fail. Another possible error is a mistake in test set up, such as the fiber placed not quite in the center of the indenter causing inconsistent loading, and thus giving incorrect results. Accidental damage to the fiber after failure is another possible source of test error. Such damage may accidentally occur during SEM sample prep, thus changing the look of the fiber, and by extension the results. More research needs to be done before these "majority" results can be used for a general description of the Zylon® 555 fibers.

CHAPTER 6. TEM FIBER ANALYSIS

6.1 TEM Sample Preparation and Procedure

Transmission Electron Microscopy (TEM) was also used in an attempt to gain atomic level insight into the structure and failure mechanisms of high performance fibers. Kevlar® KM2 and Dyneema® SK-76 fibers, before any stress was applied, were imaged.

To prepare the KM2 and SK-76 fibers for viewing in the TEM, they were sent to Helmut Gnaegi, a TEM sample preparation expert with Diatome Ltd. in Switzerland. The fibers were embedded into an epoxy resin and ultra-thin sections were cut with an ultrasonic knife. Both axial and longitudinal sections were then placed on a flat carbon grid (c-flat grid), and mounted onto a nickel TEM grid. Due to the small size of the fibers, multiple fibers were place on each TEM grid made. There were a total of 10 KM2 grids, and 3 SK-76 grids available for analysis. Both cross-sectional and longitudinal samples were sectioned and analyzed (Figure 20), with a mixture of the two in each TEM grid provided. Please note that the samples were not stained, to make sure the heavy metal present in the stain did not interfere with the sample analysis.

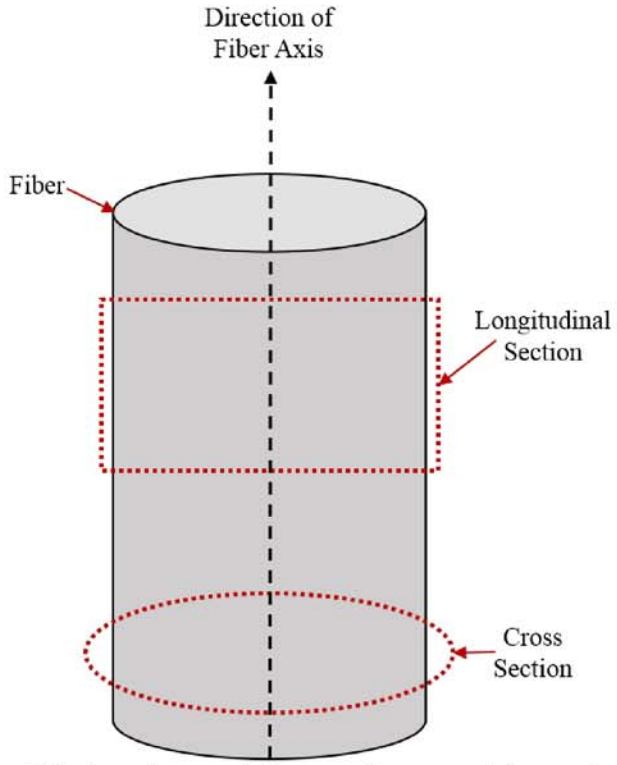

Figure 20: Schematic of the two types of fiber sections used for analysis in the TEM.

A FEI Technai-20 TEM was used to image the samples at an accelerating voltage of 100kV with the objective aperture on setting 1 (the biggest aperture), to reduce the possibility of electron beam damage, i.e. burning of the sample. For Kevlar® KM2, two of the TEM grids were analyzed, while all three grids were analyzed for Dyneema® SK-76. For each grid analyzed, multiple images were taken of both cross-sectional and longitudinal fiber samples.

It should be noted, that a FEI Nova 200 NanoLab DualBeamTM-FIB/SEM, was used in an attempt to make TEM samples, with Dyneema SK-76, using the lift out method. This method involves the cutting of a section of the fiber using an ion-beam and then attaching that section to a TEM grid. Unfortunately, the ion beam caused extreme damage to the fibers, even to sections not being cut; it burned parts of the fibers away. This made it an unusable method for making TEM samples of high performance polymer fibers. Figures 21 and 22 below, show the severe damage inflicted by the ion-beam, during fiber sectioning and sample attachment to a TEM grid, respectively.

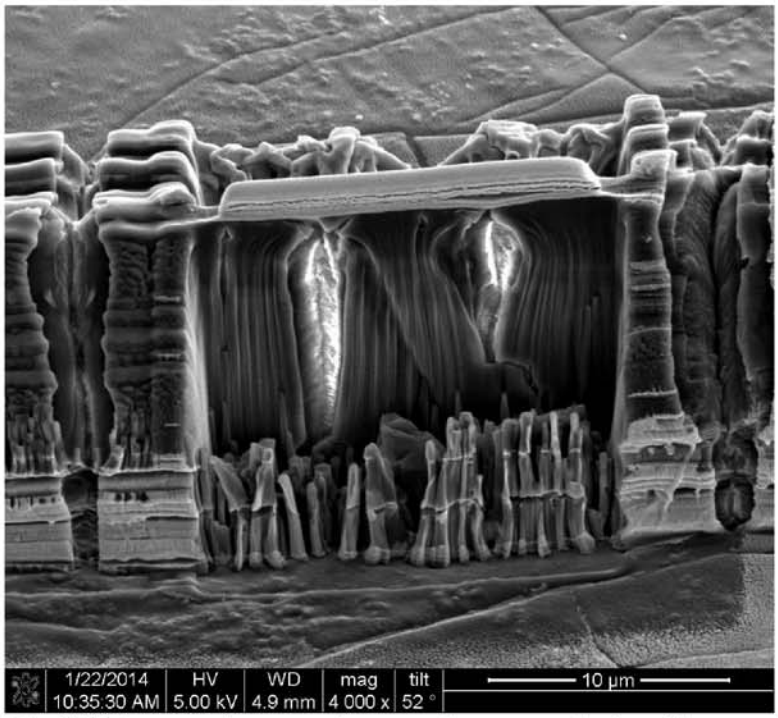

Figure 21: FIB image of severe damage that arose during fiber sectioning.

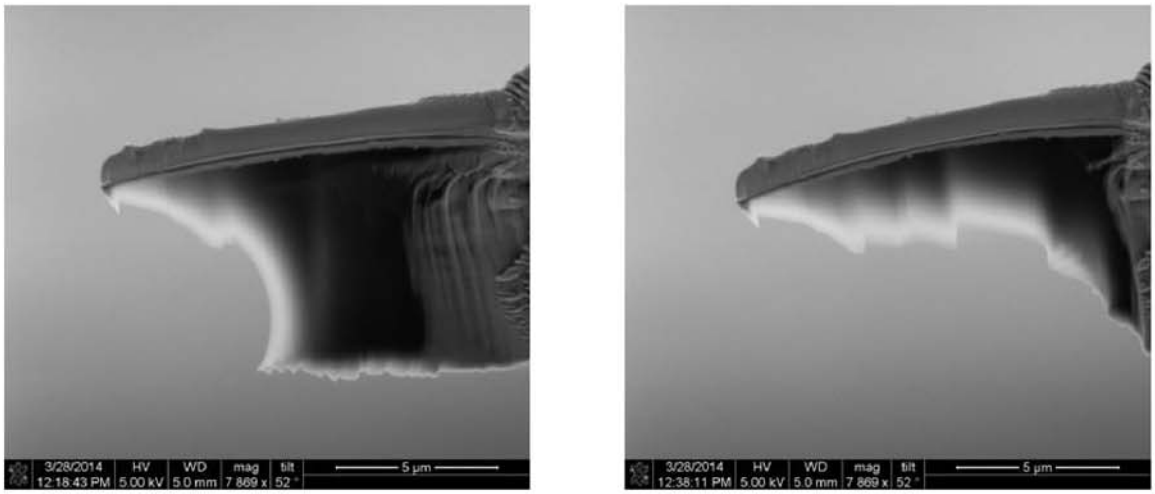

(a) (b)

Figure 22: FIB image of damage that occurred during the attaching of the fiber section to a TEM grid: a) just after attachment; b) a bit later in the attachment process.

6.2 Fiber Analysis

Only Kevlar® KM2 and Dyneema® SK-76 fibers were analyzed, because once imaging began, it became clear that problems had occurred during the sample sectioning process. In Figures 23 and 25 below, folding, tearing, and knife striations can be observed for both the KM2 and SK-76 cross-sections, respectively. It should be noted that the folds occur along the direction of the cut, implying that the sectioning caused the folds, and they are not part of the structure of the fibers, i.e. fiber damage. Figure 24, shows the edge of the KM2 fiber from Figure 23 with increasing magnification. There is no structure discernable, even at very high magnification (Figure 24d).

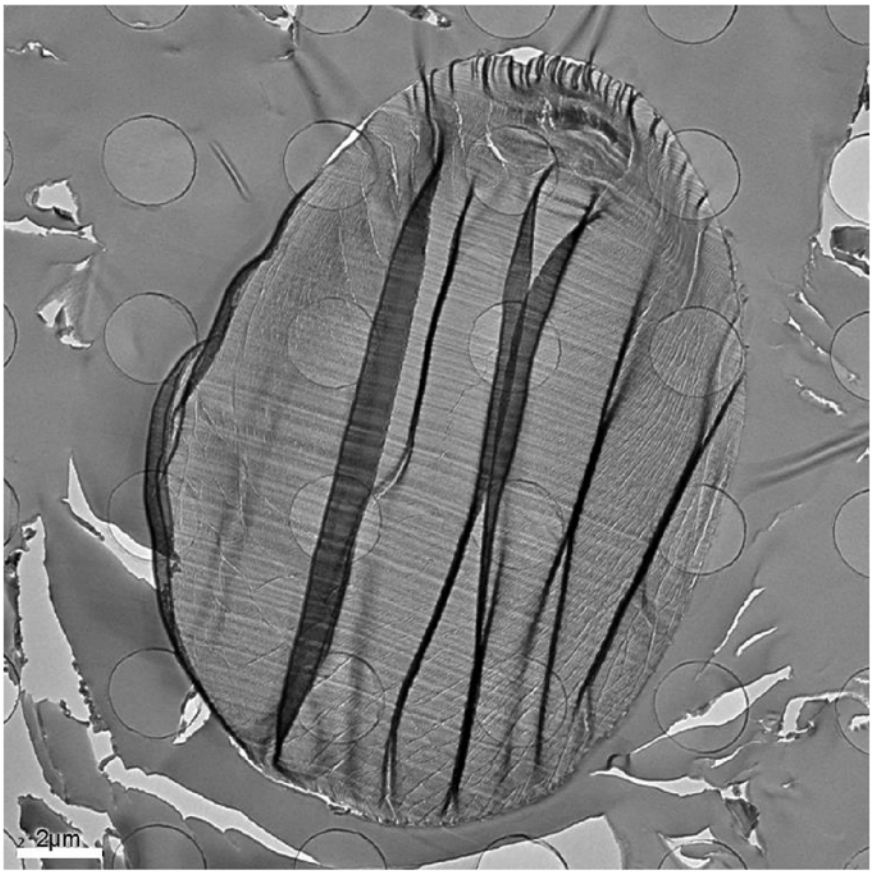

Figure 23: Cross-sectional TEM image of Kevlar® KM2 fiber, showing damage produced during sectioning.

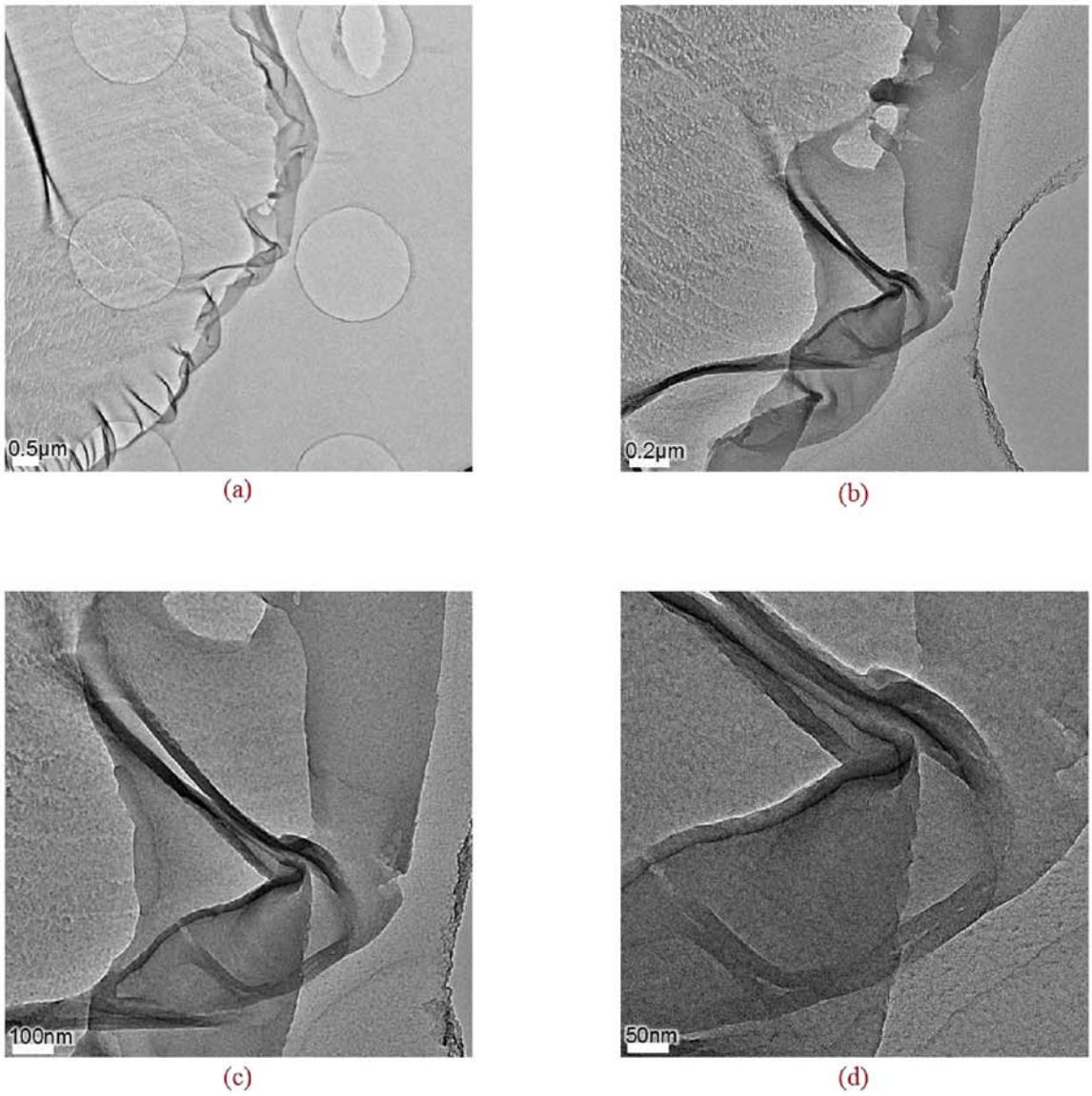

Figure 24: Multiple TEM images of cross-sectional sample of Kevlar® KM2 at increasing magnification: a) 1100x; b) 2100x; c) 4000x; d) 29,000x.

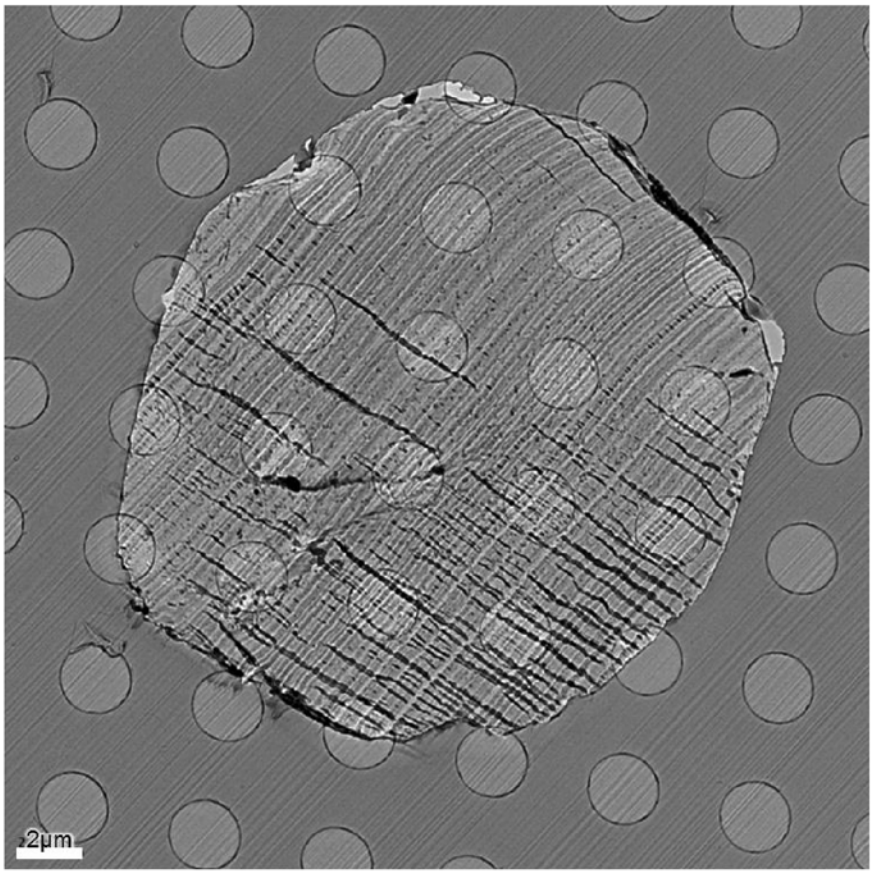

Figure 25: Cross-sectional TEM image of Dyneema® SK-76 fiber, showing damage created during sectioning.

This is also seen with the longitudinal samples of the KM2 and SK-76, shown in Figures 26 and 27, respectively. For the KM2 sample, massive tearing can be seen, as well as much more folding, though smaller in size than that in the cross-sectional view. Knife striations, however, are not observed, though their directionality can be surmised by the folding toward the bottom left corner of the image. The SK-76 sample, on the other hand, does have observable knife striations, in the vertical direction within the image. There is also major tearing and holes within the fiber section. However, the folding is more uniform and distinctive than that seen in the KM2 sample. This may be due to the shish-kebab structure of the UHSPE, being folded onto itself, or just from a stretching of that structure by the knife during sectioning, thus erasing the fine detail necessary to determine its structure.

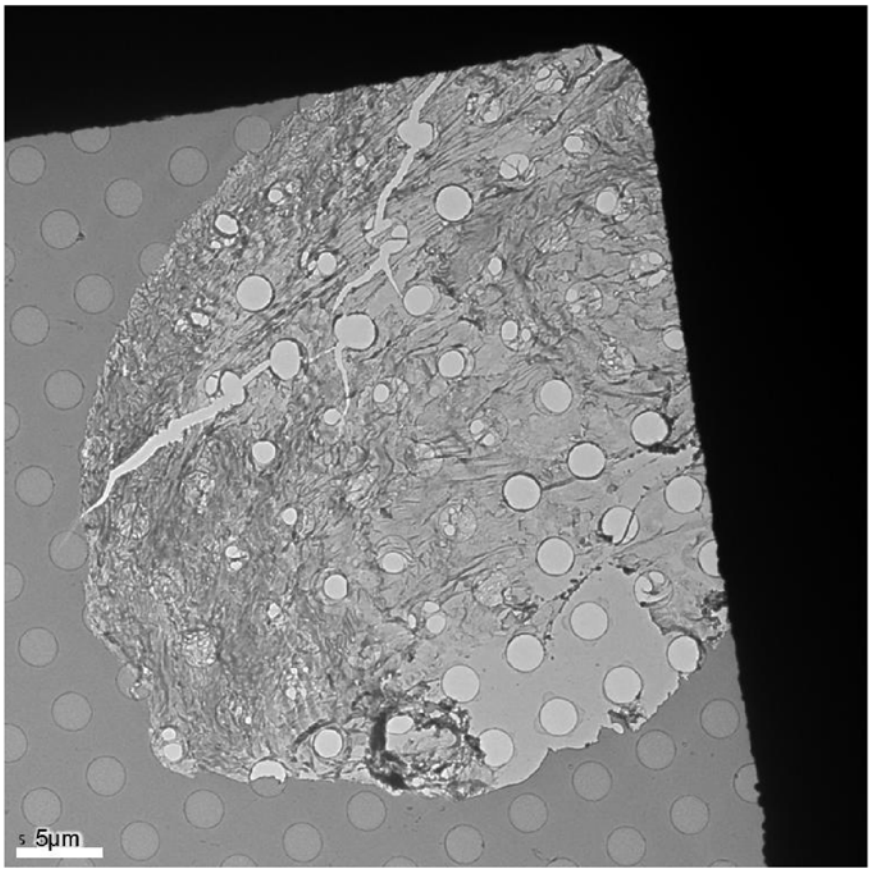

Figure 26: Longitudinal TEM image of a Kevlar® KM2 fiber, showing damage created during sectioning.

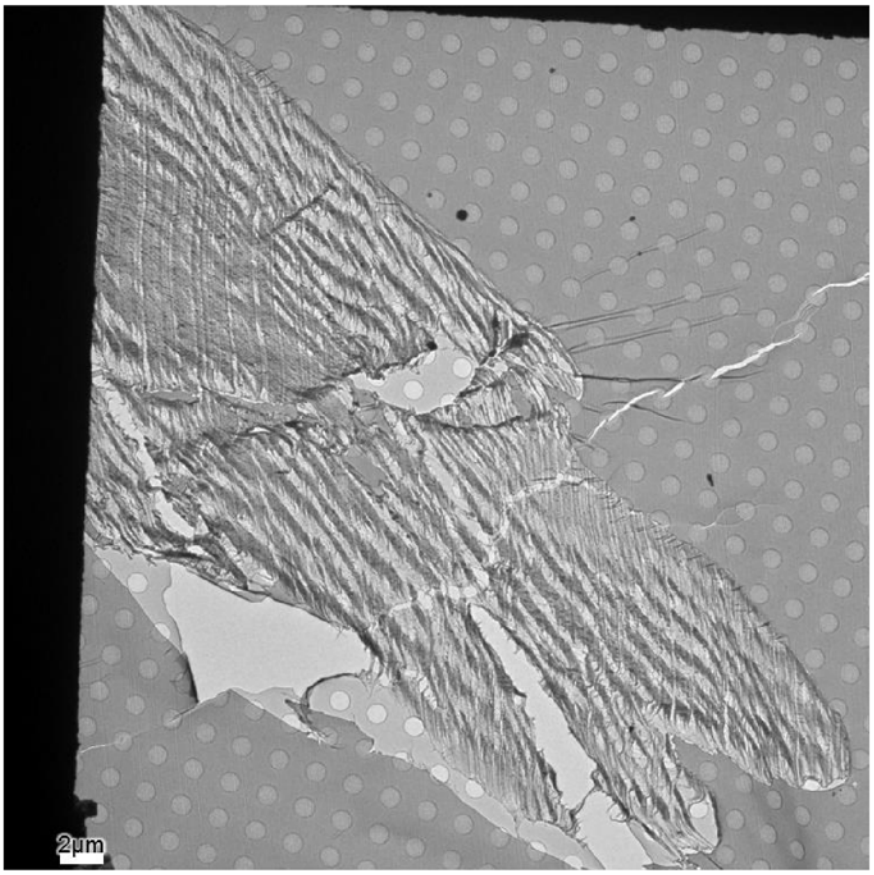

Figure 27: Longitudinal TEM image of a Dyneema® SK-76 fiber, showing damage created during sectioning.

As with the cross-sectional images, no definite fiber structure can be determined, even with increasing the magnification (Figure 28). However, the darker folds seem to be evenly spaced within the fiber, indicating that this may be the periodic shish-kebab structure that was described in Ohta, et al. [33], [43]. Nevertheless, while the dark bands are suspected to be the periodic shish-kebab structure, this cannot be confirmed, as at higher magnifications, no definite structure is observed (Figure 28c and 28d).

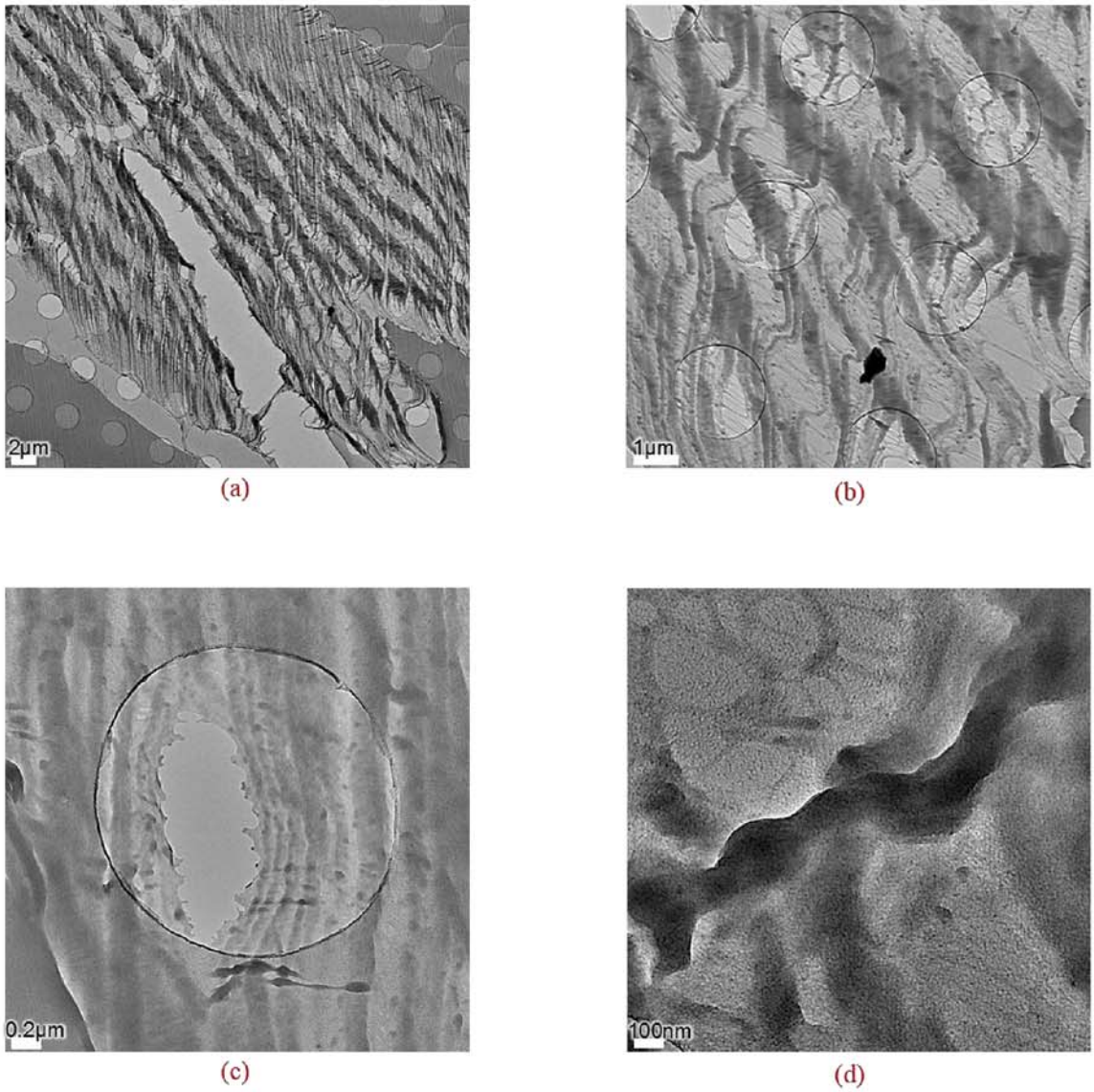

Figure 28: Multiple TEM images of longitudinal sample of Dyneema® SK-76 at increasing magnification: a) 570x; b) 2100x; c) 7000x; d) 15,000x.

This damage may have occurred due to ductile deformation caused by TEM sample preparation at room temperature; i.e. the UHSPE and PPTA fibers are very pliable at room temperature, so during sectioning the knife will "pull" the sample with it as it cuts through the fiber. Polishing the fiber/epoxy block face at temperatures below the glass transition temperature as well as staining the block faces, may reduce, if not eliminate, this damage.

During the cryo-polishing process, the temperature of the fiber/epoxy block is lowered to at or below the glass transition temperature of the high performance fiber, to restrict any fiber movement during polishing (exposing the fiber within the epoxy resin block and creating a uniform surface for staining, imaging, and sectioning). Staining makes the fiber stiffer and easier to cut (as well as providing more boundary definition within the fiber) [36], [64], [65]. An example of such a procedure was provided by Robert Cieslinski, from The Dow Chemical Company and based on the procedures used by Ohta, et al. and Brown, et al. [33], [41]–[43], [64]. The TEM sample preparation steps are:

1. Embed fibers into an epoxy resin and let cure for approximately 8 hours at 60^{o}C.

2. At room temperature, trim the fiber/epoxy sample to an appropriate shape (a trapezoidal or rectangular block generally 400µm long by 200 µm wide).

3. Cryo-polish the block face by removing 5-10µm of the face at cryogenic temperatures (Sure Freeze spray method) prior to staining. Cryo-polishing can also be done with a cryo-ultramicrotome @ -120°C.

4. Prepare the RuO_4 staining solution: place 0.2g of ruthenium trichloride into a glass bottle with a screw lid and add 10mL of 5.25% aqueous sodium hypochlorite (bleach).

5. Attach the sample blocks to a glass slide with double sided tape and place inside the bottle, in order to suspend the block face approximately 1 inch above the staining solution.

6. Place the glass jar in the fume hood and expose the samples at room temperature between 2 to 3 hours, depending on the material (2 hours is recommended for UHSPE). Longer staining may be required for other materials.

7. Slice ultra-thin sections of the fiber at room temperature and transfer these sections to a TEM grid. Please note that the first 10-15 sections will be stained too much and not slice well. Therefore use the sections sliced afterwards for TEM imaging.

The cryo-polishing in step 3, above, is the critical step to getting undamaged fiber sections. Since fiber damage occurred during the analysis of before applied stress Kevlar® KM2 and Dyneema® SK-76 fibers, Zylon® 555 fibers were not tested, nor was any after failure fibers of the KM2 or SK-76.

CHAPTER 7. FUTURE POSSIBILITIES

7.1 Future Work

The failure mechanism results mentioned in the previous chapter were performed in a quasi-static state, to see if the localized stress concentration around the indenter during impact has an effect on failure strain. The failure mechanisms observed correlated well with the failure strain data, indicating that they are correct. Therefore research at high velocity impact should be done to determine if the failure mechanisms observed in the quasi-static state hold for the high velocity state as well. If these observations hold true, then it would confirm the assertion that the geometry produced by transverse wave propagation at impact is a contributing factor in lowering the failure strain of high performance fibers during a high velocity impact. If the observations did not hold, then the fibers could be analyzed to determine what any difference may be and why that difference occurred.

This experimental method can also be applied to other high performance fibers, such as nylon, spider silk, and an updated form of PBO, known as M5, to determine if they follow the same type of failure as the high performance fibers used in this current research. Also, comparing various types of Kevlar® would eliminate any molecular variance effects that may be the cause of failure mechanisms differences and would help to determine if degree of crystallinity and orientation within the fiber has an effect on its failure mechanisms.

The TEM could also be attempted in furthering the understanding of the mechanisms behind high performance fiber failure by using cryo-sectioning to create the samples, thus

eliminating the damage seen at room temperature sectioning. Once these cryo-sectioned samples were made, a TEM could be used to analyze high performance fibers, before stress is applied, after stress is applied (but before fiber failure), and after failure, could show what is happening within a fiber on an atomic level that causes the failure. It could also give detailed insight into the failure mechanisms of through thickness shearing and fibrillation. The TEM can also be used to give a more detailed description of the fiber structure, degree of crystallinity, and degree of crystalline orientation.

These above research possibilities can ultimately be applied to numerical models in order to more accurately predict the ballistic failure of high performance fibers, and by extension, body armor. Most numerical models only consider a small section of the system in question at high velocity impact, such as a segment of ballistic cloth, and they assume that the fibers fail under tensile stress only, which as the above research has shown, is not the case. Incorporating the results from this thesis, as well as any high velocity data done in the future would improve the ballistic performance predictions and reduce, if not eliminate, the gap between predicted and experimental results. Once all the failure effects on the high performance fibers are accounted for, sections of fabric could be modeled and eventually entire bulletproof vests. Currently there is very limited research related to modeling entire bulletproof vests [5], [11].

LIST OF REFERENCES

LIST OF REFERENCES

[1] M. J. N. Jacobs and J. L. J. Van Dingenen, “Ballistic protection mechanisms in personal armour,” *J. Mater. Sci.*, vol. 36, pp. 3137–3142, 2001.

[2] S. Leigh Phoenix and P. K. Porwal, “A new membrane model for the ballistic impact response and V50 performance of multi-ply fibrous systems,” *Int. J. Solids Struct.*, vol. 40, no. 24, pp. 6723–6765, Dec. 2003.

[3] M. Grujicic, G. Arakere, T. He, W. C. Bell, B. a. Cheeseman, C. F. Yen, and B. Scott, “A ballistic material model for cross-plied unidirectional ultra-high molecular-weight polyethylene fiber-reinforced armor-grade composites,” *Mater. Sci. Eng. A*, vol. 498, pp. 231–241, 2008.

[4] B. a. Cheeseman and T. a. Bogetti, “Ballistic impact into fabric and compliant composite laminates,” *Compos. Struct.*, vol. 61, pp. 161–173, 2003.

[5] S. Chocron, T. Kirchdoerfer, N. King, and C. J. Freitas, “Modeling of Fabric Impact With High Speed Imaging and Nickel-Chromium Wires Validation,” *J. Appl. Mech.*, vol. 78, no. September 2011, p. 051007, 2011.

[6] P. Tran, T. Ngo, E. Yang, P. Mendis, and W. Humphries, “Effects of architecture on ballistic resistance of textile fabrics: Numerical study,” *Int. J. Damage Mech.*, vol. 23, no. 3, pp. 359–376, 2014.

[7] M. Mamivand and G. H. Liaghat, “A model for ballistic impact on multi-layer fabric targets,” *Int. J. Impact Eng.*, vol. 37, no. 7, pp. 806–812, 2010.

[8] C. Ha-Minh, A. Imad, F. Boussu, and T. Kanit, “On analytical modelling to predict of the ballistic impact behaviour of textile multi-layer woven fabric,” *Compos. Struct.*, vol. 99, pp. 462–476, 2013.

[9] X. Chen, F. Zhu, and G. Wells, “An analytical model for ballistic impact on textile based body armour,” *Compos. Part B Eng.*, vol. 45, no. 1, pp. 1508–1514, 2013.

[10] E. Pineda, C. Hogue, and W. Goldsmith, “Ballistic Properties of Zylon for Application to Firearm Projectile Protection,” 2003.

[11] J. D. Walker and S. Chocron, “Why Impacted Yarns Break at Lower Speed Than Classical Theory Predicts,” *J. Appl. Mech.*, vol. 78, no. September 2011, p. 051021, 2011.

[12] J. Wang and K. J. Smith, “The breaking strength of ultra-high molecular weight polyethylene fibers,” *Polymer (Guildf).*, vol. 40, no. January 1997, pp. 7261–7274, 1999.

[13] M. Hudspeth, D. Li, J. Spatola, W. Chen, and J. Zheng, “Quasi-Indenter Angle Manuscript, Part I: The effects of off-axis loading on the failure strain of various high-performance fibers,” *Text. Res. J.*, no. submitted, pp. 1–22.

[14] M. G. Dobb, D. J. Johnson, and B. P. Saville, “Supramolecular structure of a high-modulus polyaromatic fiber (Kevlar 49),” *J. Polym. Sci. Polym. Phys. Ed.*, vol. 15, pp. 2201–2211, 1977.

[15] M. Panar, P. Avakian, R. C. Blume, K. H. Gardner, T. D. Gierke, H. H. Yang, and E. I. P. De Nemours, “Morphology of Poly (p-Phenylene Terephthalamide) Fibers,” *J. Polym. Sci. Polym. Phys. Ed.*, vol. 21, no. 3075, pp. 1955–1969, 1983.

[16] M. G. Dobb, D. J. Johnson, a. Majeed, and B. P. Saville, “Microvoids in aramid-type fibrous polymers,” *Polymer (Guildf).*, vol. 20, pp. 1284–1288, 1979.

[17] A. Mathur and A. N. Netravali, “Modification of mechanical properties of Kevlar fibre by polymer infiltration,” *J. Mater. Sci.*, vol. 31, pp. 1265–1274, 1996.

[18] M. G. Northolt, “Tensile deformation of poly(p-phenylene terephthalamide) fibres, an experimental and theoretical analysis,” *Polymer (Guildf).*, vol. 21, pp. 1199–1204, 1980.

[19] M. G. Dobb, D. J. Johnson, and B. P. Saville, “Compressional behaviour of Kevlar fibres,” *Polymer (Guildf).*, vol. 22, pp. 960–965, 1981.

[20] S. Ran, D. Fang, X. Zong, B. S. Hsiao, B. Chu, and P. M. Cunniff, “Structural changes during deformation of Kevlar fibers via on-line synchrotron SAXS/WAXD techniques,” *Polymer (Guildf).*, vol. 42, pp. 1601–1612, 2001.

[21] R. J. Morgan, C. Pruneda, and W. J. Steele, “The Relationship between the Physical Structure and the Microscopic Deformation and Failure Processes of Poly (p-Phenylene Terephthalamide) Fibers,” *J. Polym. Sci. Polym. Phys. Ed.*, vol. 21, pp. 1757–1783, 1983.

[22] R. Edmunds and M. A. Wadee, “On kink banding in individual PPTA fibres,” *Compos. Sci. Technol.*, vol. 65, pp. 1284–1298, 2005.

[23] S. F. Y. Li, A. J. McGhie, and S. L. Tang, “Internal structure of Kevlar® fibres by atomic force microscopy,” *Polymer (Guildf).*, vol. 34, no. 21, pp. 4573–4575, 1993.

[24] D. L. Languerand, H. Zhang, N. S. Murthy, K. T. Ramesh, and F. Sansoz, “Inelastic behavior and fracture of high modulus polymeric fiber bundles at high strain-rates,” *Mater. Sci. Eng. A*, vol. 500, pp. 216–224, 2009.

[25] Y. Rao, A. J. Waddon, and R. J. Farris, “Structure-property relation in poly(p-phenylene terephthalamide) (PPTA) fibers,” in *Polymer*, 2001, vol. 42, no. 13, pp. 5937–5946.

[26] R. Hagege, M. Jarrin, and M. Sotton, “Direct Evidence of Radial and Tangential Morphology of High-Modulus Aromatic Polyamide Fibers,” *J. Microsc.*, vol. 115, no. 1, pp. 65–72, 1979.

[27] K. Haraguchi, T. Kajiyama, and M. Takayanagi, “Uniplanar Orientation of Poly (p-phenylene Terephthalamide) Crystal in Thin Film and Its Effect on Mechanical Properties,” *J. Appl. Polym. Sci.*, vol. 23, pp. 903–914, 1979.

[28] J. F. Graham, C. McCague, O. L. Warren, and P. R. Norton, “Spatially resolved nanomechanical properties of Kevlar fibers,” *Polymer (Guildf).*, vol. 41, pp. 4761–4764, 2000.

[29] DuPont, “Technical Guide for Kevlar,” 1990.

[30] Y. Cohen, D. M. Rein, and L. Vaykhansky, “A novel composite based on ultra-high-molecular-weight polyethylene,” *Compos. Sci. Technol.*, vol. 57, no. 96, pp. 1149–1154, 1997.

[31] K. Prasad and D. T. Grubb, “Direct observation of taut tie molecules in high-strength polyethylene fibers by Raman spectroscopy,” *J. Polym. Sci. Part B Polym. Phys.*, vol. 27, pp. 381–403, 1989.

[32] A. G. Fisch, N. Da Silveira, N. S. M. Cardozo, A. R. Secchi, J. H. Z. Dos Santos, and J. B. P. Soares, “Direct production of ultra-high molecular weight polyethylene with oriented crystalline microstructures,” *J. Mol. Catal. A Chem.*, vol. 366, pp. 74–83, 2013.

[33] Y. Ohta, H. Murase, and T. Hashimoto, “Effects of spinning conditions on the mechanical properties of ultrahigh-molecular-weight polyethylene fibers,” *J. Polym. Sci. Part B Polym. Phys.*, vol. 43, pp. 2639–2652, 2005.

[34] M. Afshari, D. J. Sikkema, K. Lee, and M. Bogle, “High Performance Fibers Based on Rigid and Flexible Polymers,” *Polym. Rev.*, vol. 48, pp. 230–274, 2008.

[35] M. Hudspeth, X. Nie, and W. Chen, “Dynamic failure of Dyneema SK76 single fibers under biaxial shear/tension,” *Polym. (United Kingdom)*, vol. 53, no. 24, pp. 5568–5574, 2012.

[36] C. Oudet and H. H. Kausch, “An electron microscopy study of the polyethylene fibres,” *J. Mater. Sci. Lett.*, vol. 10, pp. 1061–1065, 1991.

[37] X. Liu and W. Yu, “Evaluation of the tensile properties and thermal stability of ultrahigh-molecular-weight polyethylene fibers,” *J. Appl. Polym. Sci.*, vol. 97, pp. 310–315, 2005.

[38] D. Jauffrès, O. Lame, G. Vigier, and F. Doré, “Microstructural origin of physical and mechanical properties of ultra high molecular weight polyethylene processed by high velocity compaction,” *Polymer (Guildf).*, vol. 48, pp. 6374–6383, 2007.

[39] J. M. Kelly, “Ultra-High Molecular Weight Polyethylene*,” *J. Macromol. Sci. Part C Polym. Rev.*, vol. 42, no. 3, pp. 355–371, 2002.

[40] D. J. Carr, “Failure mechanisms of yarns subjected to ballistic impact,” *J. Mater. Sci. Lett.*, vol. 18, pp. 585–588, 1999.

[41] T. Hashimoto, H. Murase, and Y. Ohta, “A new scenario of flow-induced shish-kebab formation in entangled polymer solutions,” *Macromolecules*, vol. 43, pp. 6542–6548, 2010.

[42] H. Murase, Y. Ohta, and T. Hashimoto, “A new scenario of shish-kebab formation from homogeneous solutions of entangled polymers: Visualization of structure evolution along the fiber spinning line,” *Macromolecules*, vol. 44, pp. 7335–7350, 2011.

[43] Y. Ohta, H. Murase, and T. Hashimoto, “Structural Development of Ultra High Strength Polyethylene Fibers,” *J. Polym. Sci. Part B Polym. Phys.*, vol. 48, pp. 1861–1872, 2010.

[44] Y. Sakai and K. Miyasaka, “Development of fibrillar texture during simultaneous biaxial drawing of ultra-high-molecular-weight polyethylene dried gels,” *Polymer (Guildf).*, vol. 31, no. 002, pp. 51–57, 1990.

[45] P. Schwartz, A. Netravali, and S. Sembach, “Effects of Strain Rate and Gauge Length on the Failure of Ultra-High Strength Polyethylene Fibers,” *Text. Res. J.*, vol. 56, no. 8, pp. 502–508, 1986.

[46] H. C. Kuo and M. C. Jeng, “Effects of part geometry and injection molding conditions on the tensile properties of ultra-high molecular weight polyethylene polymer,” *Mater. Des.*, vol. 31, pp. 884–893, 2010.

[47] K. S. Kanaga Karuppiah, A. L. Bruck, S. Sundararajan, J. Wang, Z. Lin, Z. H. Xu, and X. Li, "Friction and wear behavior of ultra-high molecular weight polyethylene as a function of polymer crystallinity," *Acta Biomater.*, vol. 4, pp. 1401–1410, 2008.

[48] S. Chocron, A. E. Nicholls, A. Brill, A. Malka, T. Namir, D. Havazelet, H. Van Der Werff, U. Heisserer, and J. D. Walker, "Modeling unidirectional composites by bundling fibers into strips with experimental determination of shear and compression properties at high pressures," *Compos. Sci. Technol.*, vol. 101, pp. 32–40, 2014.

[49] P. J. Hazell, G. J. Appleby-Thomas, X. Trinquant, and D. J. Chapman, "In-fiber shock propagation in Dyneema®," *J. Appl. Phys.*, vol. 110, 2011.

[50] D. C. Prevorsek, Y. D. Kwon, and H. B. Chin, "Analysis of the temperature rise in the projectile and extended chain polyethylene fiber composite armor during ballistic impact and penetration," *Polym. Eng. Sci.*, vol. 34, no. 2, pp. 141–152, 1994.

[51] S. Ran, C. Burger, D. Fang, X. Zong, S. Cruz, B. Chu, B. S. Hsiao, R. A. Bubeck, K. Yabuki, Y. Teramoto, D. C. Martin, M. A. Johnson, and P. M. Cunniff, "In-Situ Synchrotron WAXD/SAXS Studies of Structural Development durng PBO/PPA Solution Spinning," *Macromolecules*, vol. 35, pp. 433–439, 2002.

[52] C. Burger, S. Ran, D. Fang, D. Cookson, K. Yabuki, Y. Teramoto, P. M. Cunniff, P. J. Viccaro, B. S. Hsiao, and B. Chu, "Time-Resolved Structural Studies in Fiber Processing," *Macromol. Symp.*, vol. 195, pp. 297–302, 2003.

[53] J. N. Uju and L. L. O. Ox, "Development and Evaluation of Polybenzoxazole Fibrous Structures," *NASA Tech. Memo.*, p. 22, 1995.

[54] S. Ran, C. Burger, D. Fang, X. Zong, B. Chu, B. S. Hsiao, Y. Ohta, K. Yabuki, and P. M. Cunniff, "A Synchrotron WAXD Study on the Early Stages of Coagulation during PBO Fiber Spinning," *Macromolecules*, vol. 35, no. 27, pp. 9851–9853, 2002.

[55] M. Lammers, E. a. Klop, M. G. Northolt, and D. J. Sikkema, "Mechanical properties and structural transitions in the new rigid-rod polymer fibre PIPD (`M5') during the manufacturing process," *Polymer (Guildf).*, vol. 39, no. 24, pp. 5999–6005, 1998.

[56] A. L. Forster, P. Pintus, G. H. R. Messin, M. A. Riley, S. Petit, W. Rossiter, J. Chin, and K. D. Rice, "Hydrolytic stability of polybenzobisoxazole and polyterephthalamide body armor," *Polym. Degrad. Stab.*, vol. 96, no. 2, pp. 247–254, Feb. 2011.

[57] J. Chin, A. Forster, C. Clerici, L. Sung, M. Oudina, and K. Rice, “Temperature and humidity aging of poly(p-phenylene-2,6-benzobisoxazole) fibers: Chemical and physical characterization,” *Polym. Degrad. Stab.*, vol. 92, no. 7, pp. 1234–1246, Jul. 2007.

[58] D. J. Daniels and S. V Hart, “Status Report to the Attorney General on Body Armor Safety Initiative Testing and Activities,” *NIJ Spec. Rep.*, 2004.

[59] “Supplement I : Status Report to the Attorney General on Body Armor Safety Initiative Testing and Activities Status Report to the Attorney General on Body Armor Safety Initiative,” *NIJ Spec. Rep.*, 2004.

[60] S. Ran, X. Zong, D. Fang, B. S. Hsiao, B. Chu, P. M. Cunniff, and R. a. Phillips, “Studies of the mesophase development in polymeric fibers during deformation by synchrotron SAXS/WAXD,” *J. Mater. Sci.*, vol. 36, pp. 3071–3077, 2001.

[61] M. G. Dobb, D. J. Johnson, and B. P. Saville, “Direct observation of structure in high-modulus aromatic fibers,” *J. Polym. Sci. Polym. Symp.*, vol. 58, pp. 237–251, 1977.

[62] G. Srinivasan and D. H. Reneker, “Structure and morphology of small diameter electrospun aramid fibers,” *Polym. Int.*, vol. 36, pp. 195–201, 1995.

[63] M. Hudspeth, W. Chen, and J. Zheng, “Quasi-Indenter Angle Manuscript, Part II: Why the Smith theory over-predicts instant rupture velocities during fiber transverse impact,” *Text. Res. J.*, no. submitted, pp. 1–19.

[64] G. M. Brown and J. H. Butler, “New method for the characterization of domain morphology of polymer blends using ruthenium tetroxide staining and low voltage scanning electron microscopy (LVSEM),” *Polymer (Guildf).*, vol. 38, no. 15, pp. 3937–3945, 1997.

[65] D. Montezinos, B. G. Wells, and J. L. Burns, “The use of ruthenium in hypochlorite as a stain for polymeric materials,” *J. Polym. Sci. Polym. Lett. Ed.*, vol. 23, pp. 421–425, 1985.

APPENDIX

APPENDIX

A.1 Kevlar® KM2 Fiber Failure

Kevlar ® KM2 fibers were tested with the razor blade, round, and FSP indenters at angles between 10^o and 50^o. The failed ends of these fibers were then imaged with a SEM to determine the failure mode present.

A.1.1 Razor Blade

For the razor blade indenter at 10^o, KM2 showed almost complete through thickness shearing, with some fibrillation at the tips, and a slight amount of splitting along the fiber axis (Figure A1). Figure A1a and A1c show this slight tip fibrillation as well as the small degree of fiber splitting. Figure A1b, however, shows a larger amount of fiber splitting (into two longer strands) as well as the slight fibrillation on the each cut tip.
Based on these observations, it was concluded that the main failure mechanism for this angle was through thickness shearing.

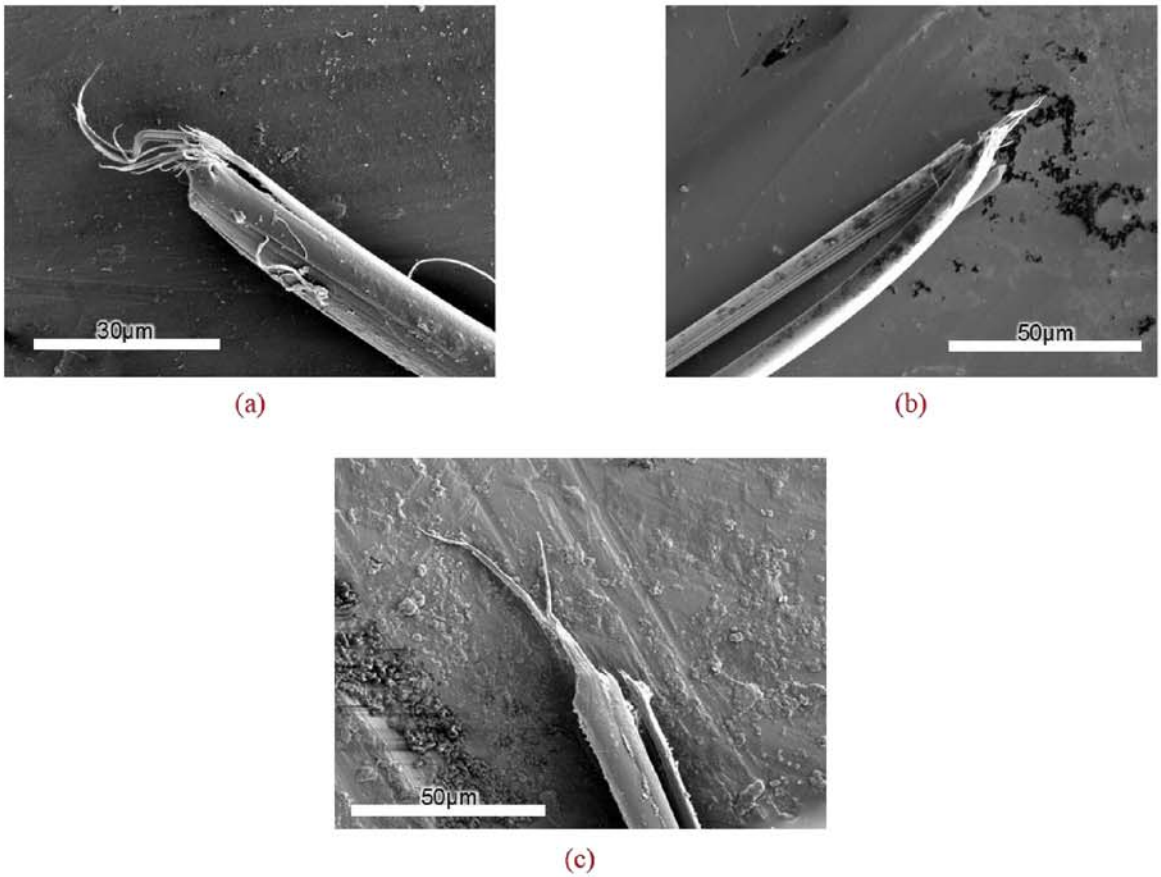

(a) (b)

(c)

A 1: SEM image of Kevlar® KM2 fiber failure with the razor blade at 10°.

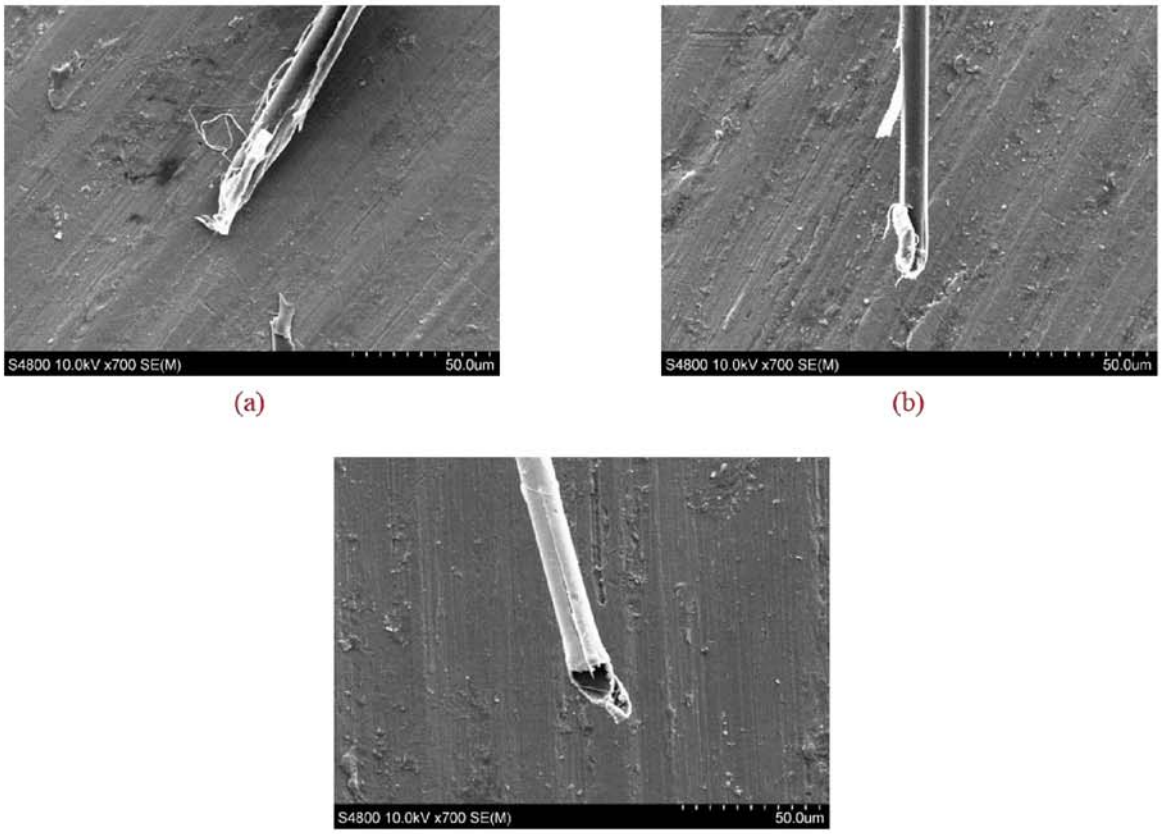

(a) (b)

(c)

A 2: SEM image of Kevlar® KM2 fiber failure for three fibers with the razor blade at 20°.

For 20°, the main failure mechanism observed is definitely through thickness shearing (Figure A2). It should be noted, however, that a slight peeling effect is observed, which indicates a slight amount of fibrillation occurring at the skin region of the fiber.

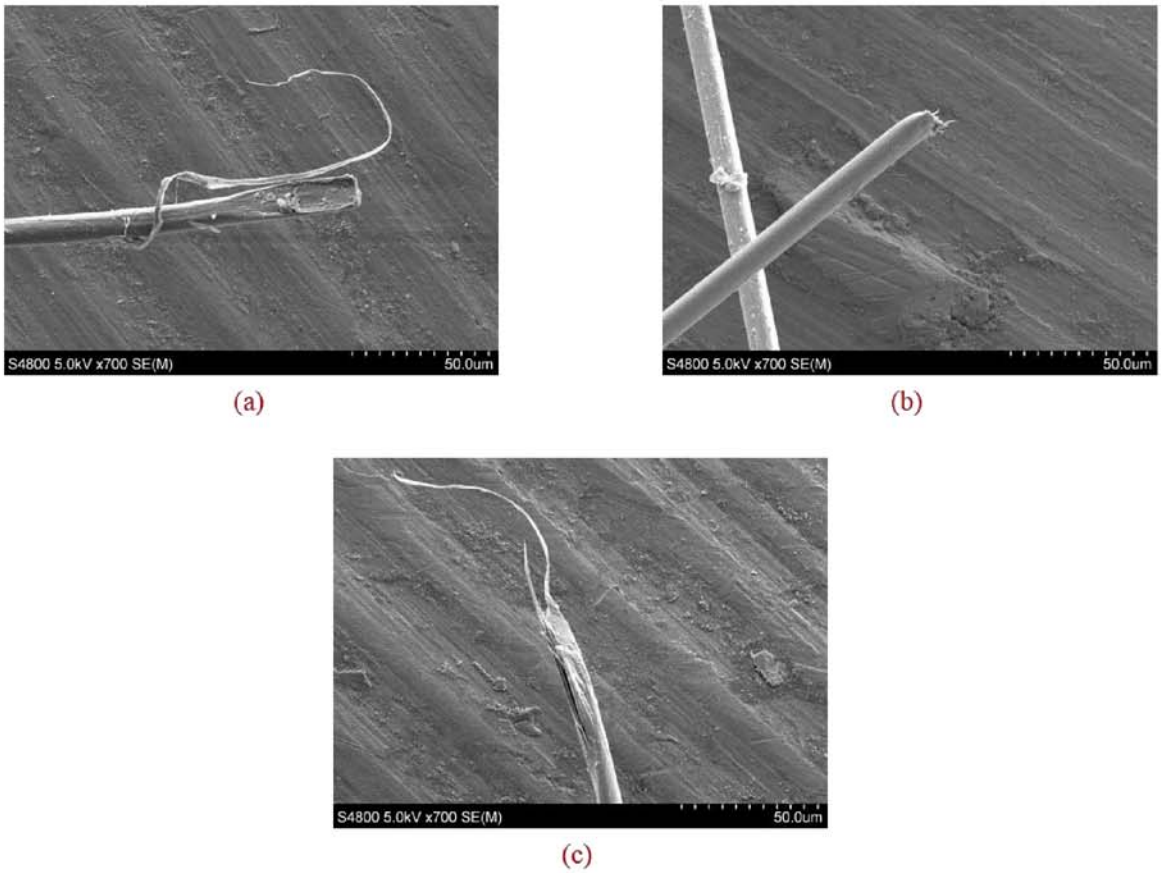

(a) (b)

(c)

A 3: SEM image of Kevlar® KM2 fiber failure for three fibers with the razor blade at 30°.

At 30°, the observed failure is quite similar to that seen at the previous angle; through thickness shearing, with a small amount of fibrillation from the skin present (Figure A3). However, the ends of these fibers have the appearance of a flat head screw driver. This indicates that through thickness shearing occurred at an angle, instead of perpendicular to the fiber, as seen at higher angles.

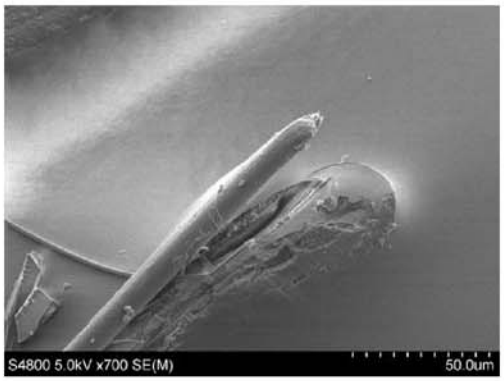

(a)

(b)

(c)

A 4: SEM image of Kevlar® KM2 fiber failure for three fibers with the razor blade at 40°.

At 40°, the KM2 fibers have a normal cut appearance (Figure A4). Therefore, it can be concluded that through thickness shearing is the failure mechanism at this angle.

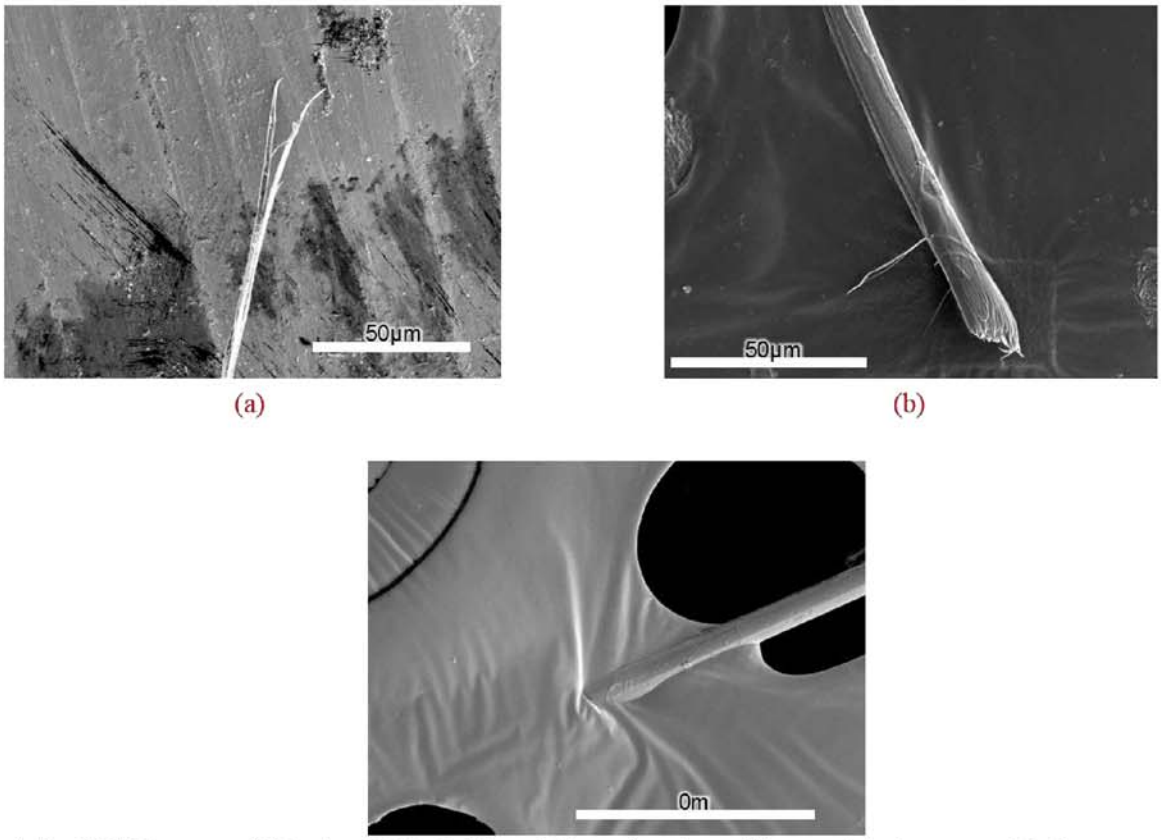

A 5: SEM image of Kevlar® KM2 fiber failure for three fibers with the razor blade at 50°.

In Figure A5, for 50°, the failure observed is a little inconsistent. Figure A5a, shows a splitting of the fiber at the failure end, while Figure A5b shows through thickness shearing. Unfortunately in Figure A5c, the failure mechanism cannot be confirmed, since the fiber tip is covered. However, based on observations of the fiber up until the covered tip (no fibrillation, splitting, thinning, etc.), it is likely that it is through thickness shearing. A few more samples would need to be tested to confirm this, though it is in agreement with the data provided in Part I.

A.1.2 Round Indenter

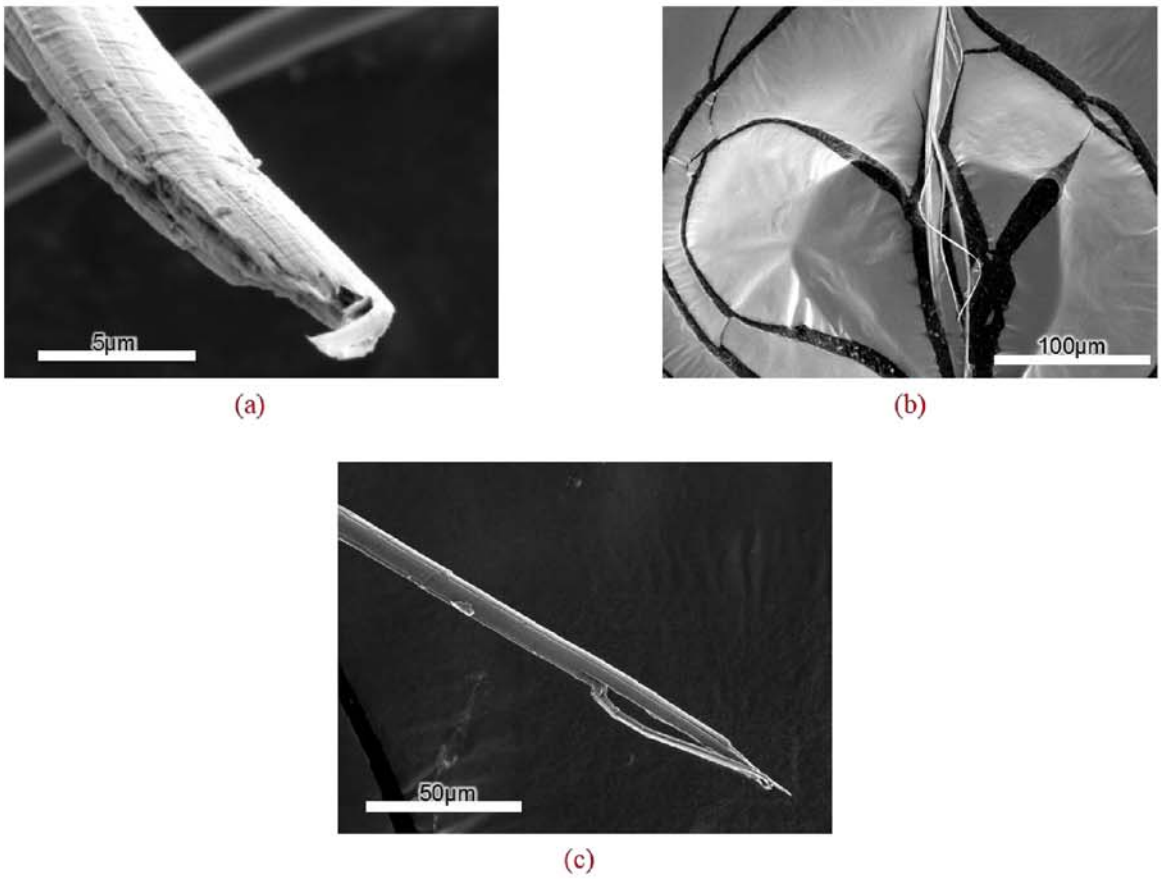

(a) (b)

(c)

A 6: SEM image of Kevlar® KM2 fiber failure for three fibers with the round indenter at 10°.

At 10°, the round indenter caused fibrillation and some fracturing of the KM2 fiber ends (Figure A6). Figure A6a, shows the fractured end with a small curved fibril at the very tip, almost as if the fiber started to fibrillate, but left half of the fiber snapped, causing the jagged, fractured look. Figure A6b and A6c showed only fibrillation. Based on these observations, as well as the data from Part I (showing the higher failure strain than the razor blade), fibrillation is concluded to be the main failure mechanism at this angle.

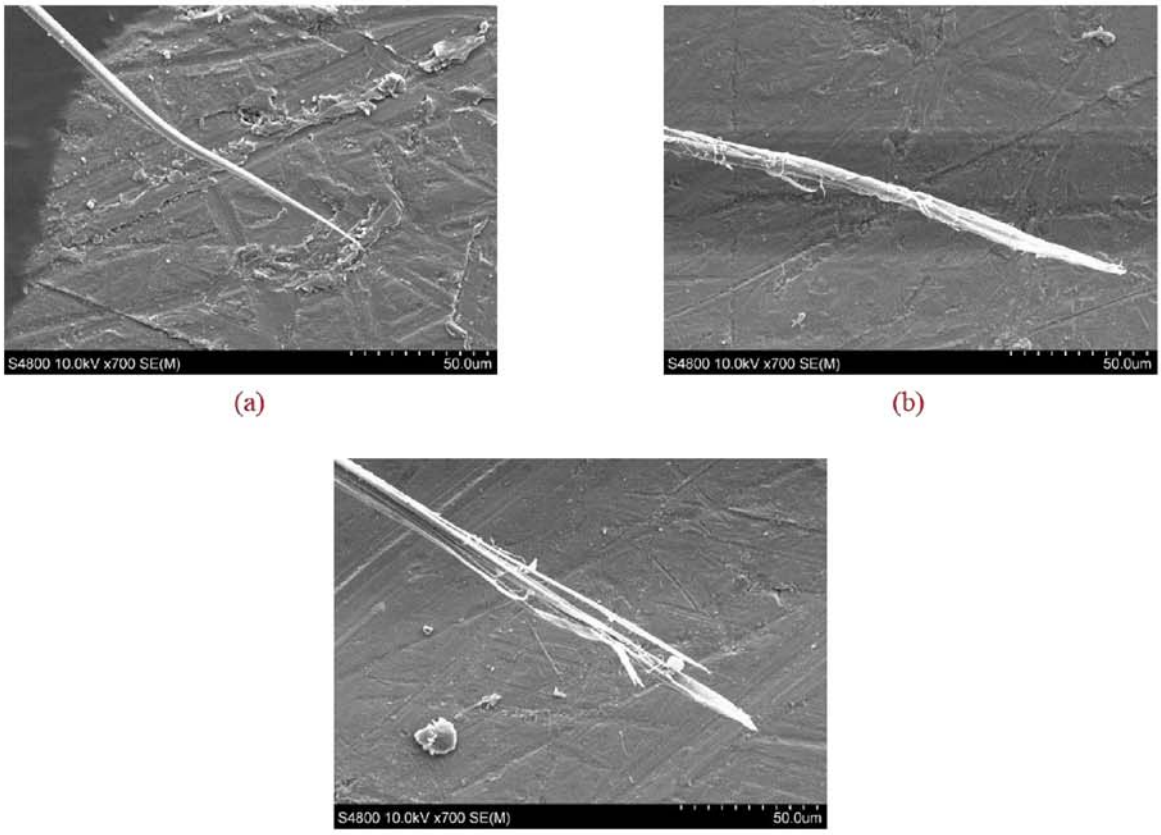

(a) (b)

(c)

A 7: SEM image of Kevlar® KM2 fiber failure for three fibers with the round indenter at 20°.

For 20°, the main failure mechanism is fibrillation (Figure A7). All of the images in Figure A7 show fibrillation, though in Figure A7a, it is in the form of fiber thinning, i.e. the fiber diameter gets smaller, tapering off at the end.

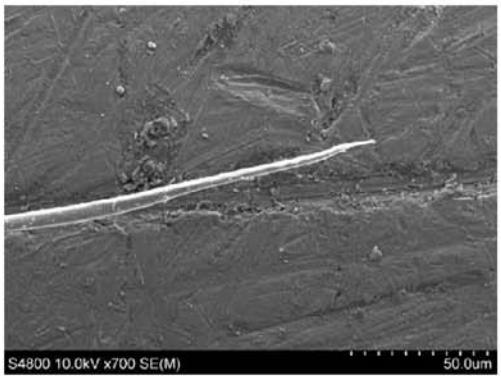

(a)

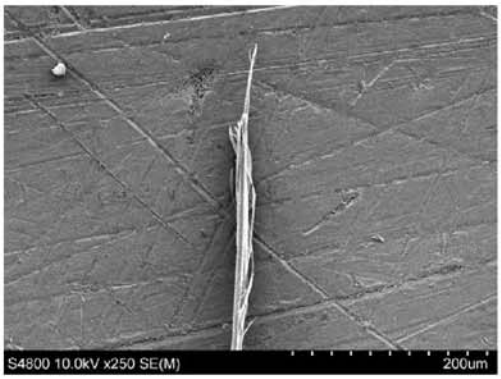

(b)

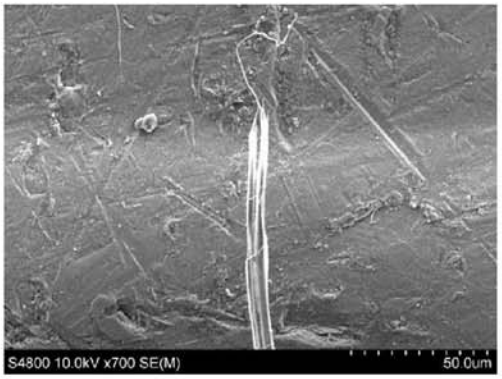

(c)

A 8: SEM image of Kevlar® KM2 fiber failure for three fibers with the round indenter at 30°.

For the round indenter at 30°, there is thinning as well as thin fibrils present in the failed fibers (Figure A8). This indicates, that fibrillation is the main failure mechanism that occurs at the angle.

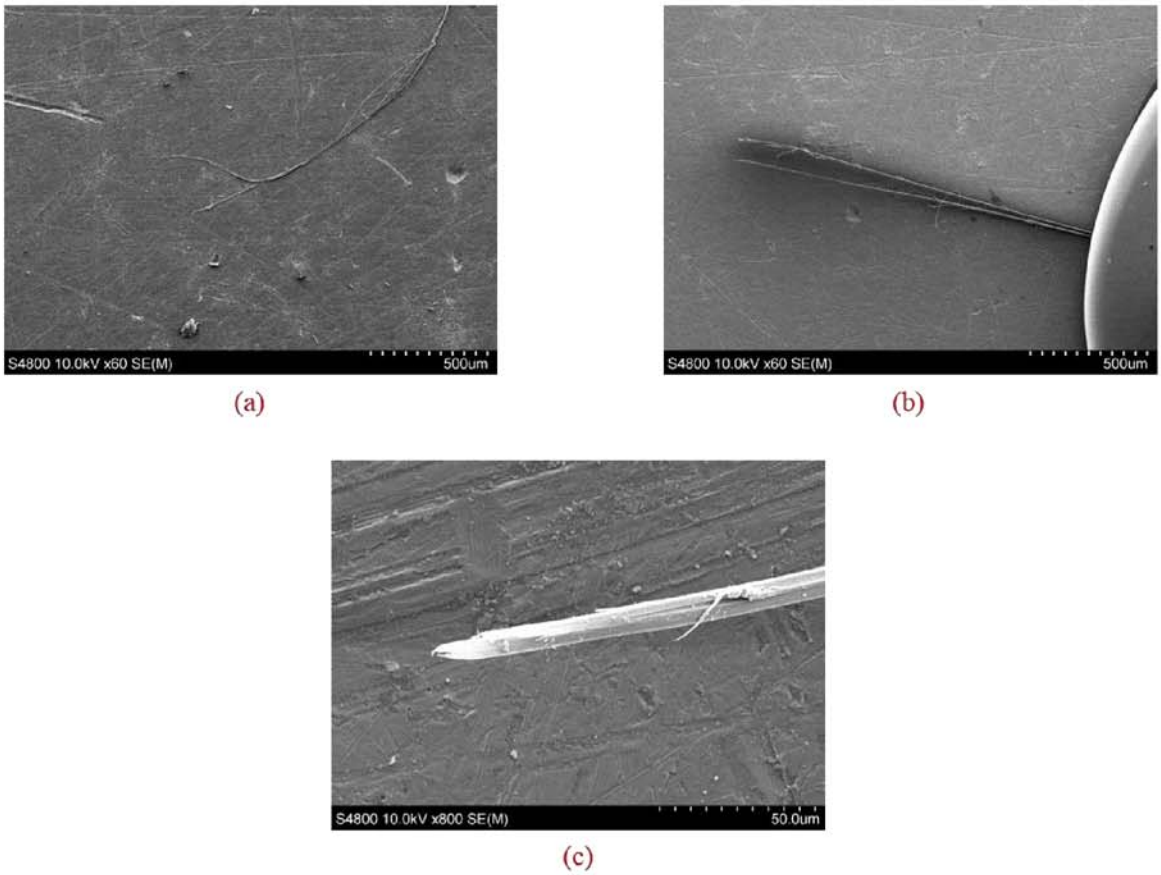

A 9: SEM image of Kevlar® KM2 fiber failure for three fibers with the round indenter at 40°.

For 40°, there is some inconsistency in the fiber failure observed (Figure A9). Figure A9a shows fibrillation occurring along a large portion of the fiber, while Figure A9b shows some fiber splitting with small fibrils visible. Figure A9c, on the other hand, shows only a slight amount of fiber thinning before failure occurred. Despite these discrepancies, the main failure mechanism can be determined to be fibrillation; as thinning and the small amount of fibrillation in Figure A9c and A9b respectively are considered a type of fibrillation.

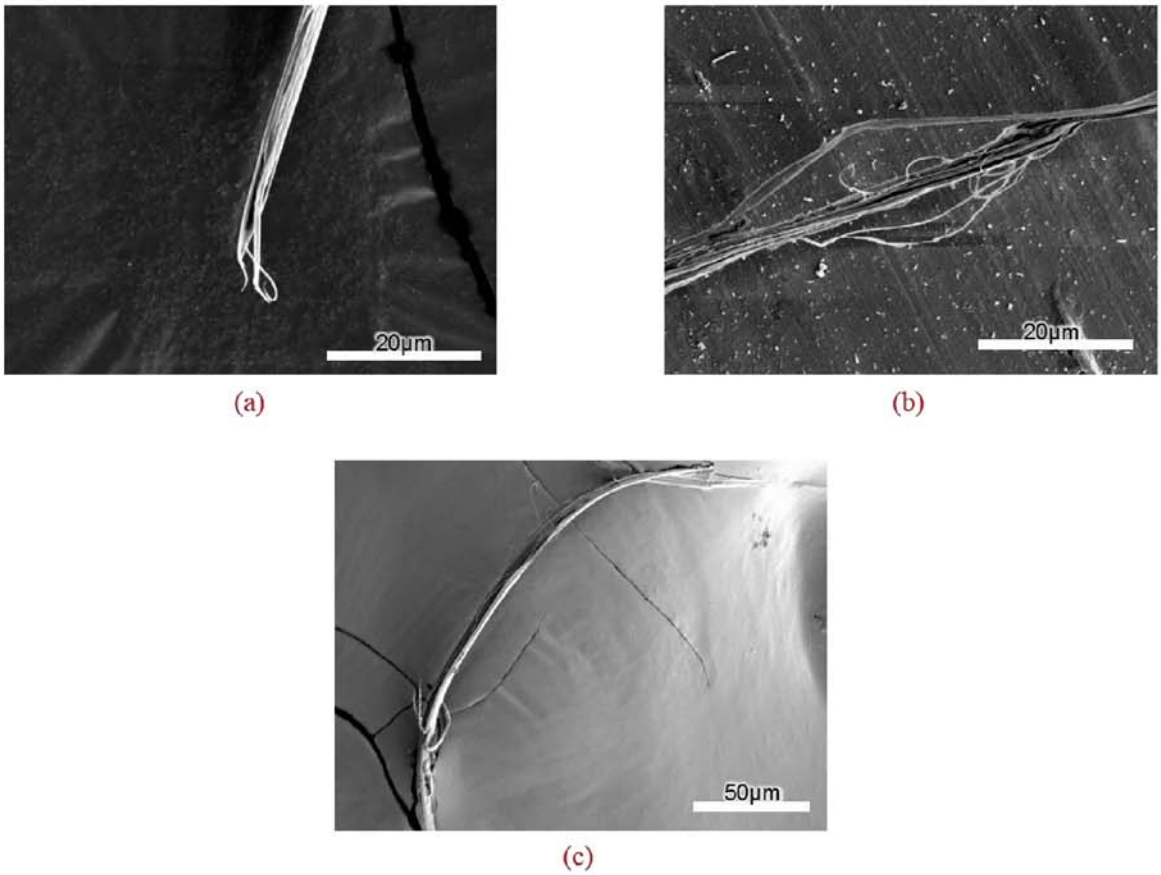

(a) (b)

(c)

A 10: SEM image of Kevlar® KM2 fiber failure for three fibers with the round indenter at 50°.

At the 50° angle, the main failure mechanism is fibrillation (Figure A10). All of the images show fibrillation occurring at the site of fiber failure, though some are more extensive than others.

A.1.3 FSP Indenter

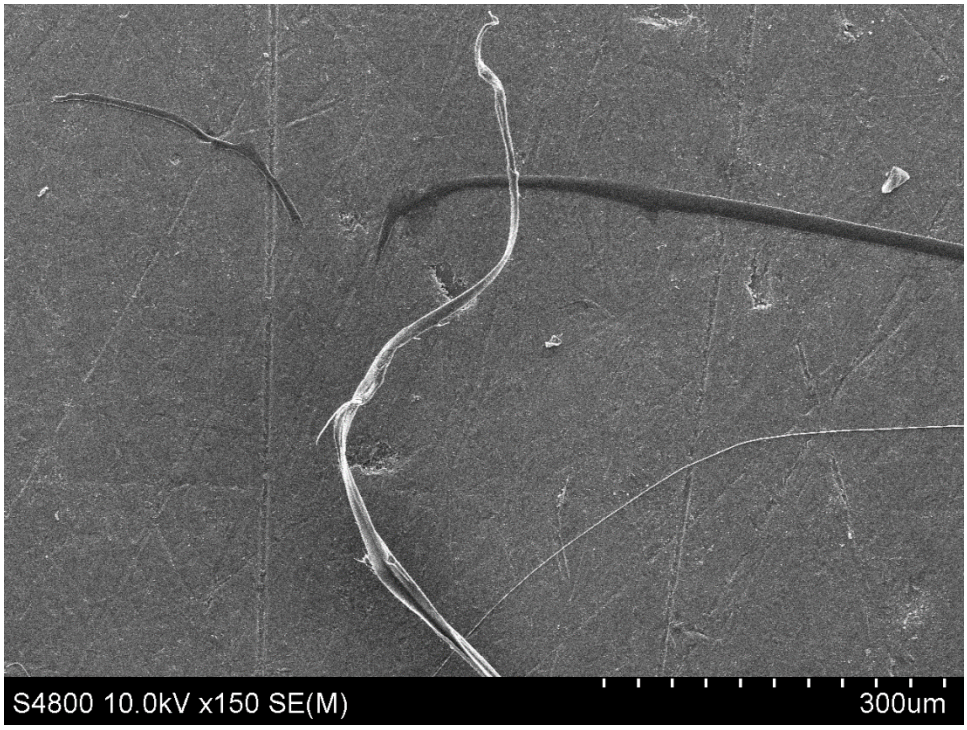

A 11: SEM image of Kevlar® KM2 fiber failure with the FSP indenter at 10°.

For the FSP indenter at 10°, KM2 failure occurs by fibrillation (Figure A11). The image shows a slight fibrillation of the fiber as well as thinning of the fiber end. More samples are needed to confirm this type of failure.

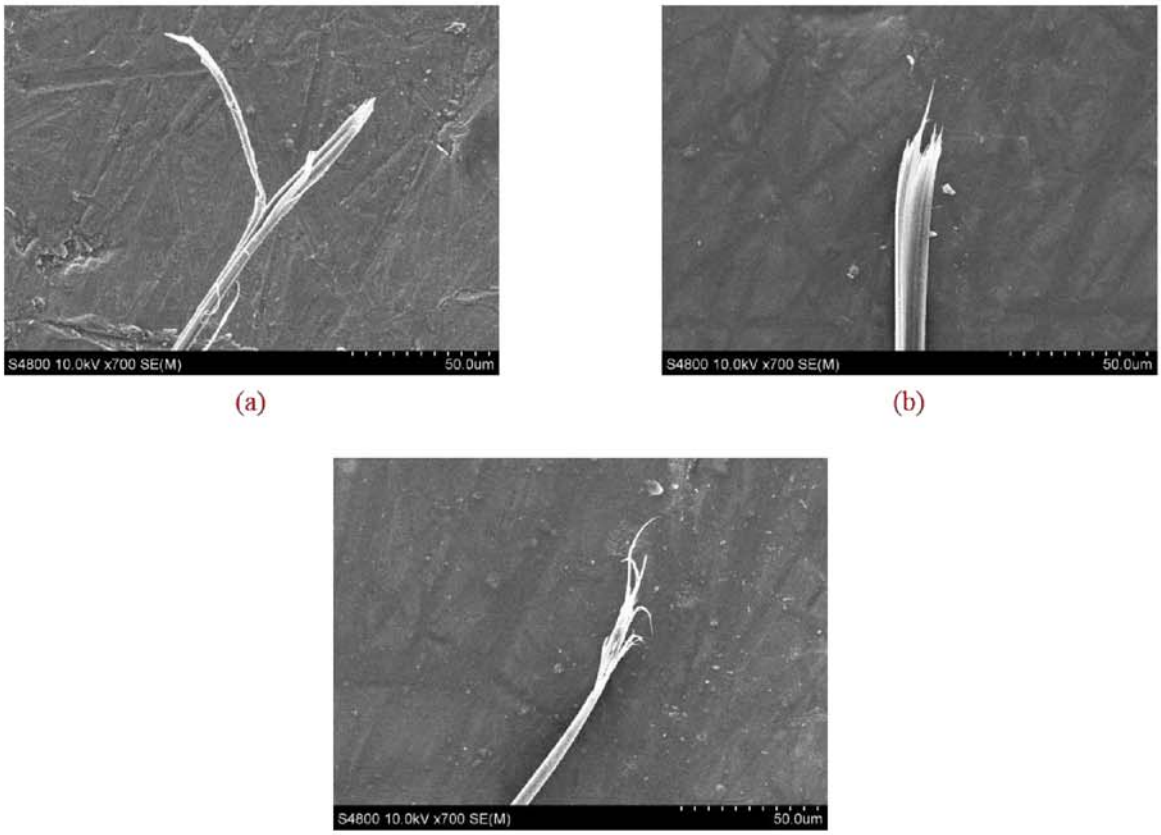

(a) (b)

(c)

A 12: SEM image of Kevlar® KM2 fiber failure for three fibers with the FSP indenter at 20°.

Figure A12 shows KM2 failure at 20°, due to fibrillation. Figure A12a and A12c show this fibrillation, while Figure A12b only shows a slight fibrillation on the end. Despite this small difference in failure, it can be assumed that the failure of KM2 at 20° is due to fibrillation, similar to the round indenter.

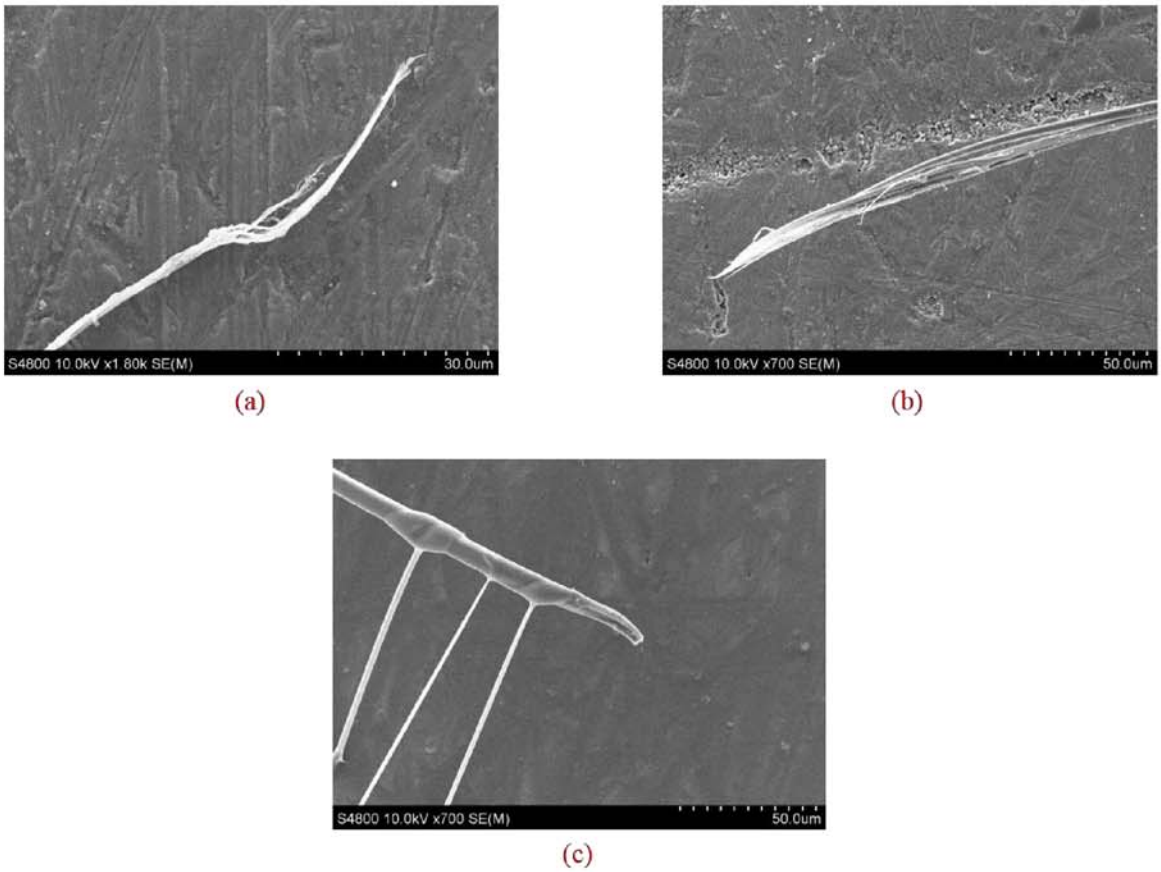

A 13: SEM image of Kevlar® KM2 fiber failure for three fibers with the FSP indenter at 30°.

At 30°, KM2 shows less fibrillation as well as a more cut appearance (Figure A13). It should be noted that in Figure A13c, some of the superglue got on the end of the fiber, sealing it together. However, there is a crevice on the end of the fiber, indicating where there was fibrillation originally. Therefore, it can be concluded that KM2 still fails by fibrillation, but is starting to transition into the cut look indicative of the razor blade.

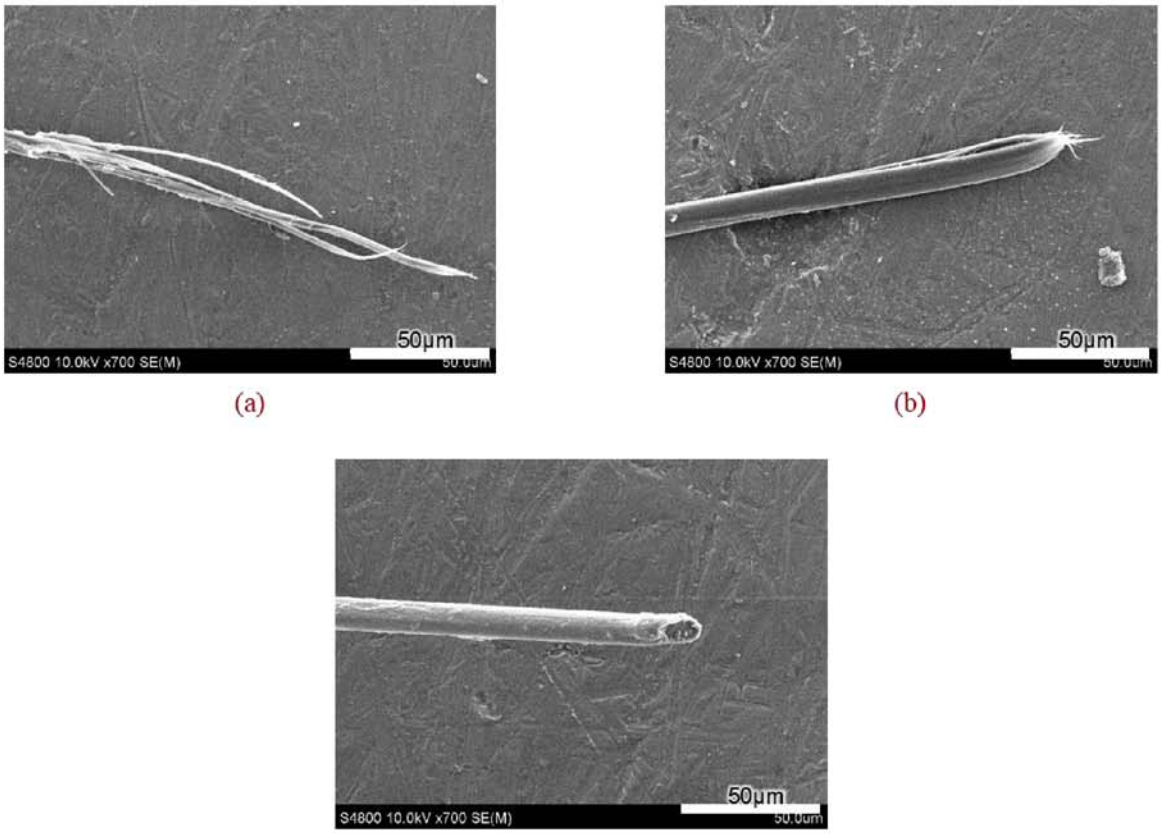

(a) (b)

(c)

A 14: SEM image of Kevlar® KM2 fiber failure for three fibers with the FSP indenter at 40°.

The failure mechanism for Kevlar® KM2 at 40° is slightly unclear (Figure A14). In Figure A14a, the fiber shows fibrillation, while in Figure A14b, there is a cut appearance, with a tiny amount of fibrillation on the ends. In Figure A14c, there is a total cut look, without any fibrillation present. Despite this difference in failure mechanism at 40°, KM2 is concluded to fail by mostly through thickness shearing, since both Figure A14b and A14c, have a cut appearance, and the data provided in Part I of this research is in line with this conclusion.

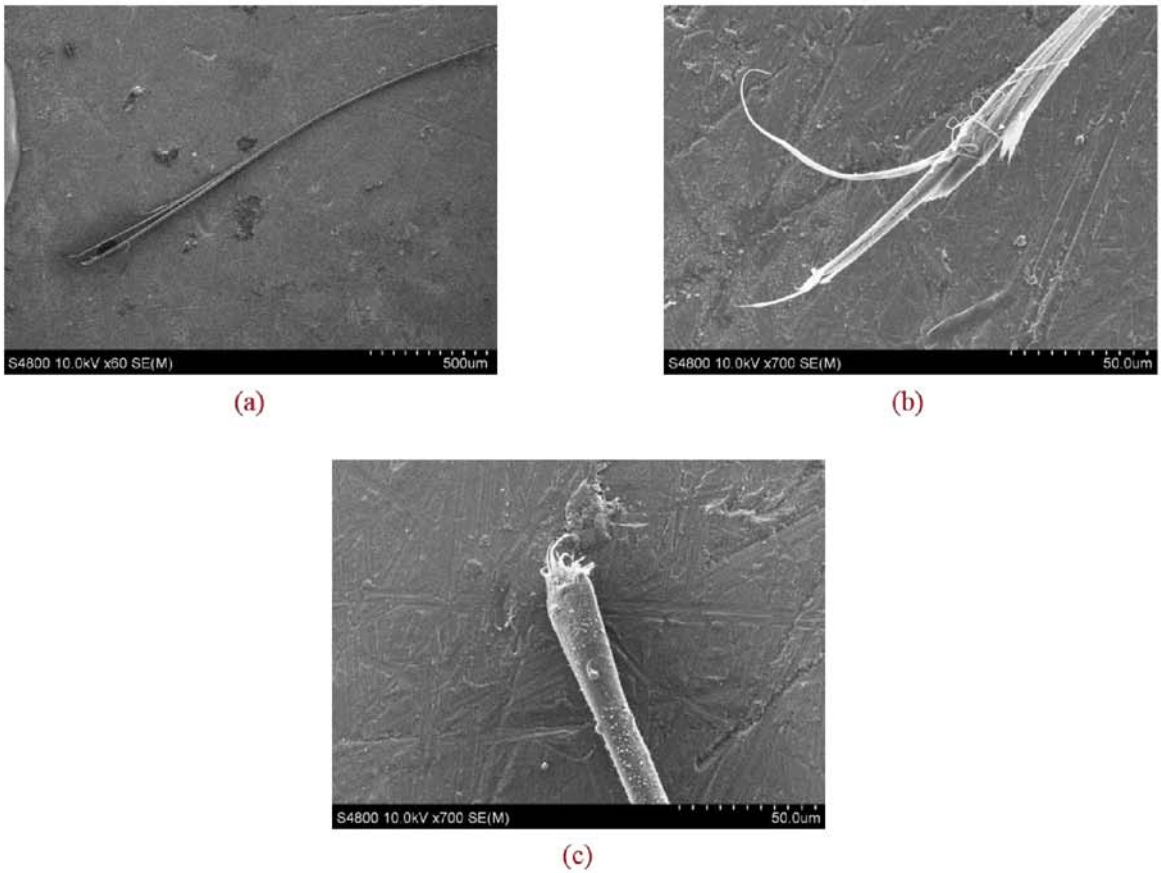

(a) (b)

(c)

A 15: SEM image of Kevlar® KM2 fiber failure for three fibers with the FSP indenter at 50°.

At 50°, there is a difference in failure mechanisms present as well. In Figure A15a, the fiber splits into two towards the failure end, but each split has a cut look on the tips, with only slight fibrils protruding. In Figure A15b, the fiber shows fibrillation on the tip of the fiber, while in Figure A15c, there is a cut appearance, with only a slight amount of fibrillation on the failed fiber tip. Based on the data gathered in Part I, as well as the cut look in Figure A15a and A15c, the most likely failure mechansim at this angle is through thickness shearing with a slight fibrillation at the tip.

A.2 Dyneema® SK-76 Fiber Failure

Dynnema® SK-76 fibers were tested with the razor blade, round, and FSP indenters at angles of 10°-50°. The failed ends of these fibers were then analyzed using a SEM to determine the failure mode present.

A.2.1 Razor Blade

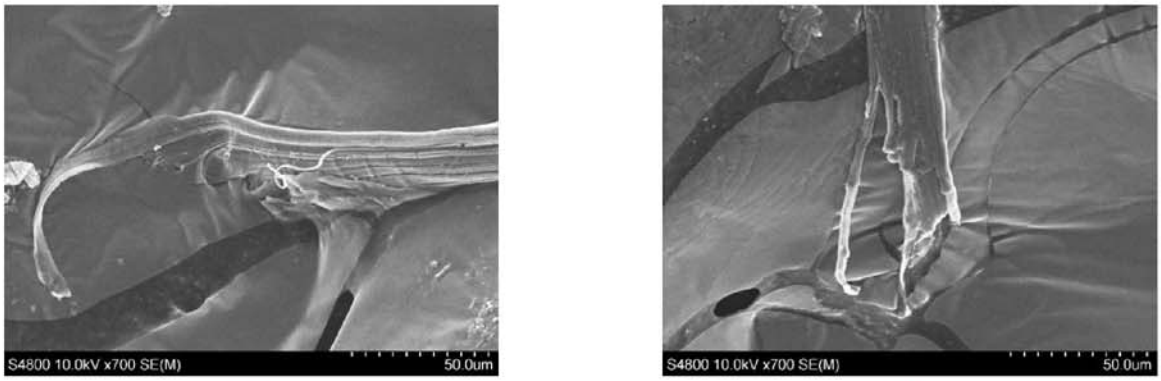

(a) (b)

A 16: SEM image of Dyneema® SK-76 fiber failure for two fibers with the razor blade at 10°.

For the razor blade indenter at 10°, there a shaved look about the fibers, almost as if the blade and fiber were held together and the blade was then pulled along the fiber until failure (Figure A16). This is very unusual, though it should be noted that the pulled ends still have a slight cut appearance. Since there are only two samples, these results should be checked through additional testing.

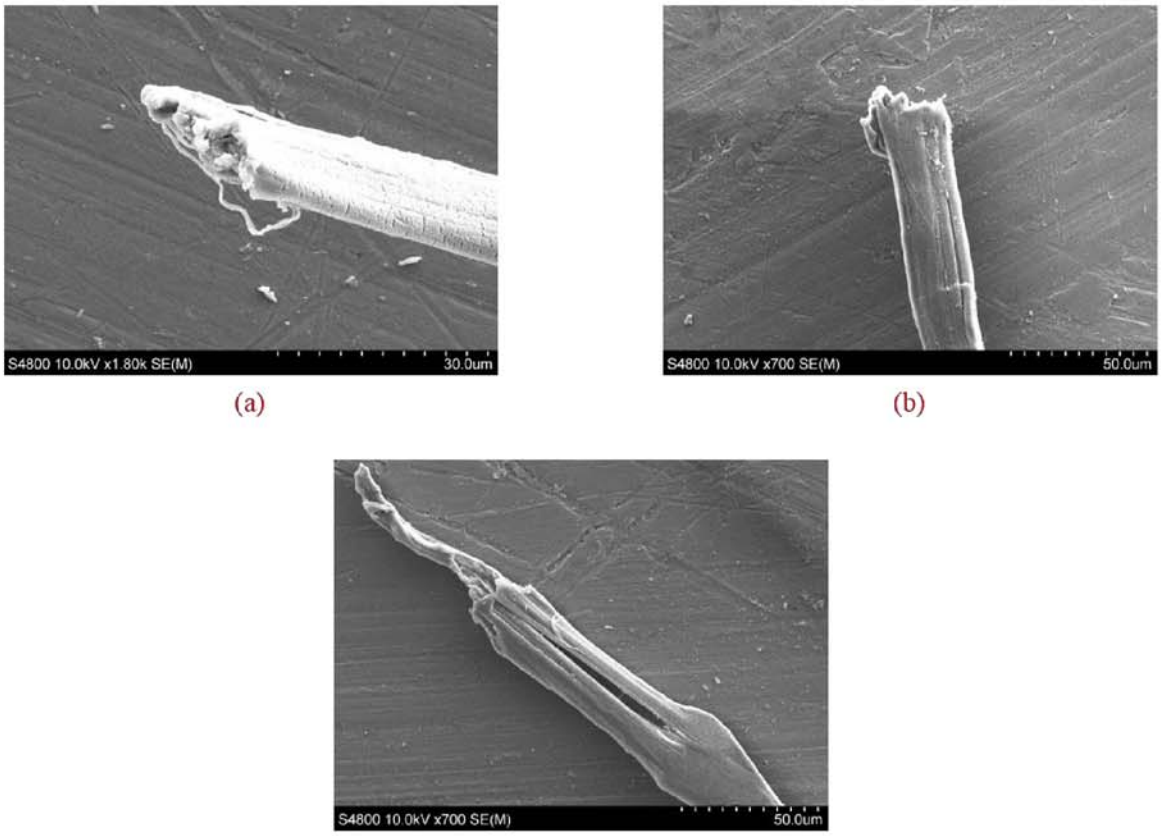

A 17: SEM image of Dyneema® SK-76 fiber failure for three fibers with the razor blade at 20°.

At 20°, the fibers, shown in Figure A17, present through thickness shearing as the main failure mechanism, though Figure A17c shows a partial cut with thinning/fibrillation on the other half. Despite this half cut appearance, it can still be concluded that the failure mechanism for these fibers is through thickness shearing.

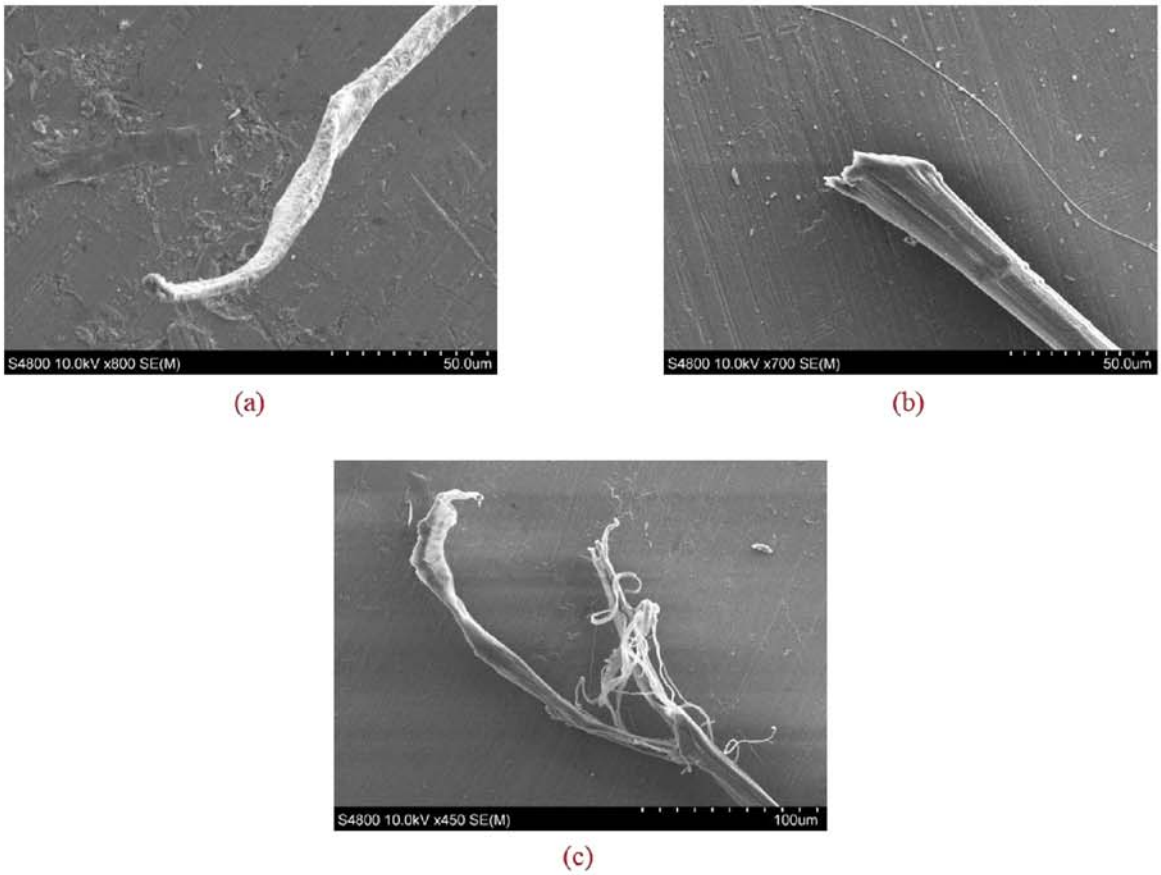

A 18: SEM image of Dyneema® SK-76 fiber failure for three fibers with the razor blade at 30°.

There is also some discrepancy in the fiber results at 30° (Figure A18). Here in can be seen that one fiber is a bit thinned with a cut end (A18a), one is just cut (A18b), and the last failed by fibrillation (A18c). However, since two of the three fibers show shearing as the cause of failure, it was concluded that through thickness shearing is the main failure mechanism for SK-76, using the razor blade at 30°.

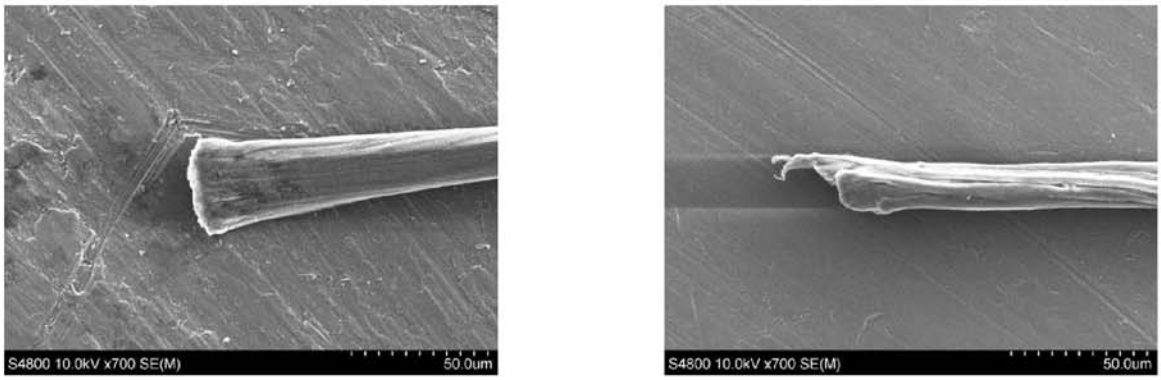

(a) (b)

A 19: SEM image of Dyneema® SK-76 fiber failure for two fibers with the razor blade at 40°.

At 40°, the images shown in Figure A19 above, show that through thickness shearing is the main failure mechanism. However, a few more tests should be done, since only two fibers were available for imaging.

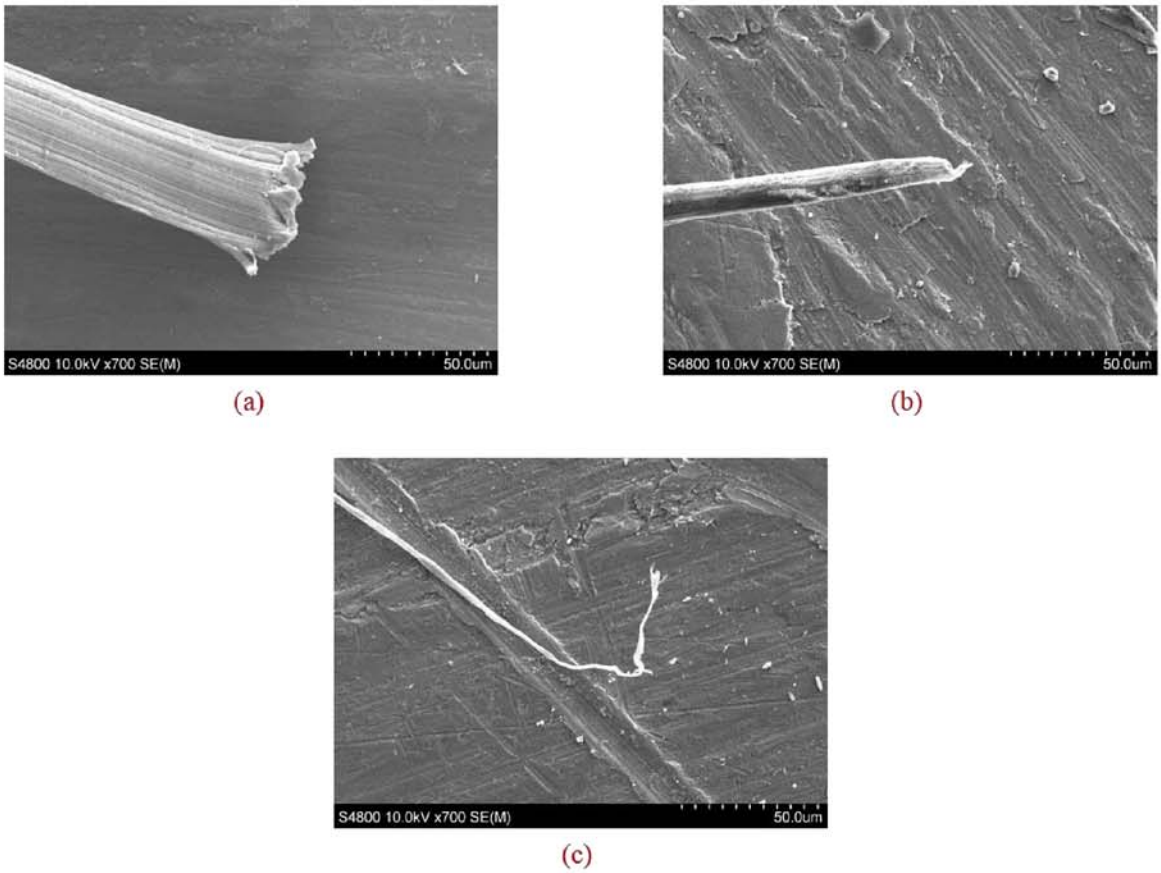

(a) (b)

(c)

A 20: SEM image of Dyneema® SK-76 fiber failure for three fibers with the razor blade at 50°.

For the highest angle of 50°, the main failure mechanism was also through thickness shearing (Figure A20). As shown, the ends of the fibers have a cut appearance, though Figure A20c, also shows a small amount of thinning before the cut end.

A.2.2 Round Indenter

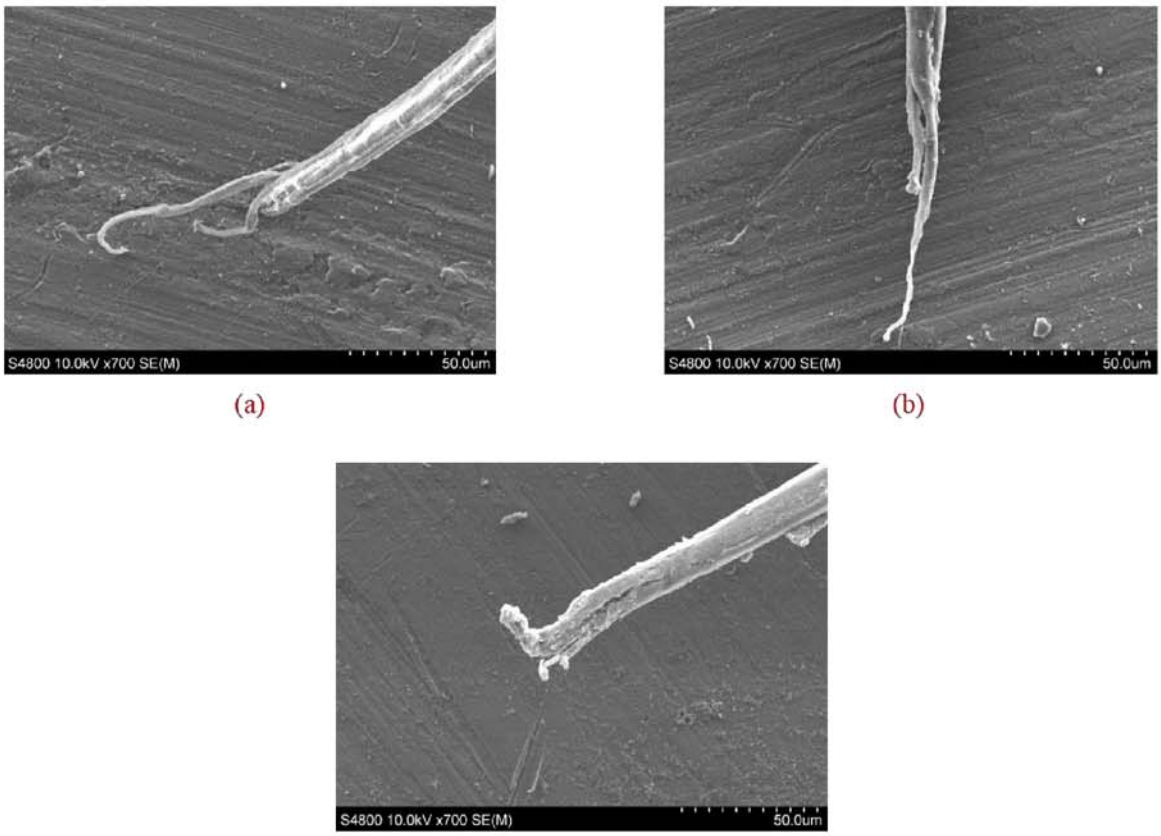

(a) (b)

(c)

A 21: SEM image of Dyneema® SK-76 fiber failure for three fibers with the round indenter at 10°.

For the round indenter at 10°, Dyneema® SK-76 shows fibrillation as the main failure mechanism, though there are only a few fibrils (Figure A21).

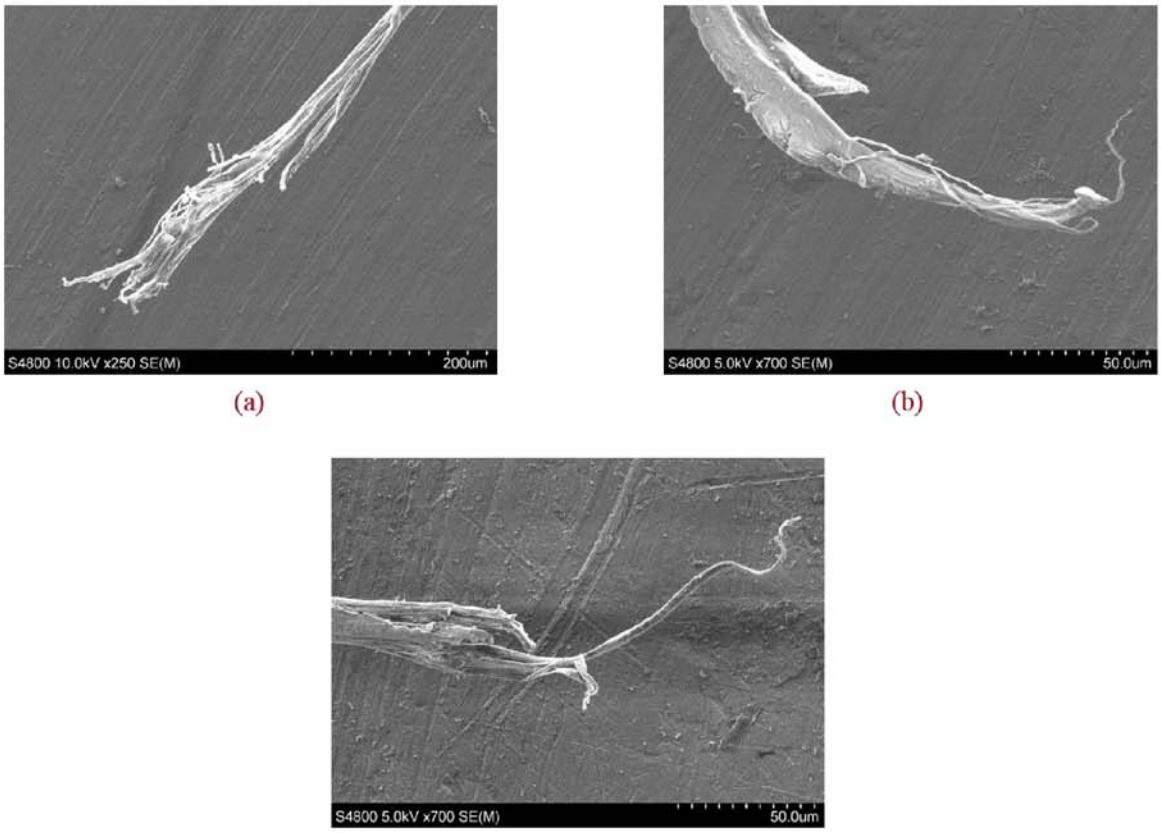

A 22: SEM image of Dyneema® SK-76 fiber failure for three fibers with the round indenter at 20°.

At 20°, fibrillation is also observed to be the failure mechanism, and is a bit more extensive than that observed at the previous angle (Figure A22).

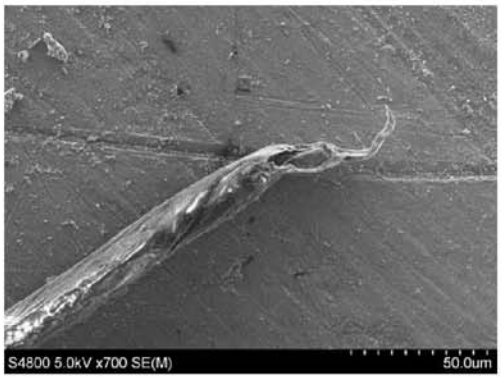

(a)

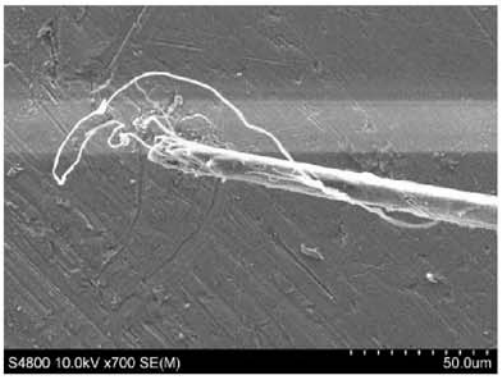

(b)

(c)

A 23: SEM image of Dyneema® SK-76 fiber failure for three fibers with the round indenter at 30°.

At 30°, fibrillation is again the main failure mechanism (Figure A23). However, it appears in the form of fiber thinning, as shown in Figure A23c, as well as in slight fibril separation as seen in A23a and A23b.

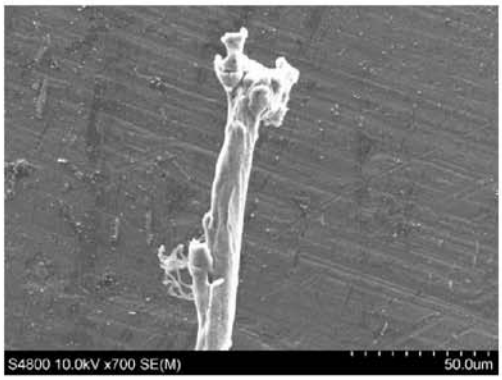

(a)

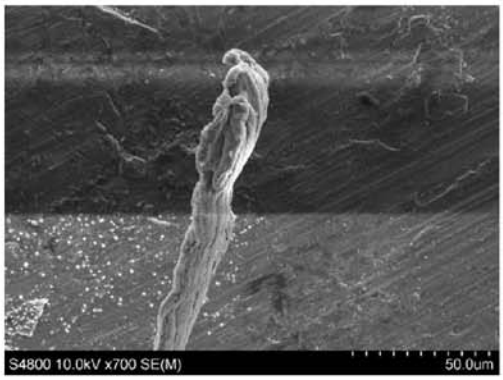

(b)

(c)

A 24: SEM image of Dyneema® SK-76 fiber failure for three fibers with the round indenter at 40°.

While, different in appearance that the fibrillation shown previously, it is nevertheless the main failure mechanism for the 40° angle as well (Figure A24). The odd shapes/balls observed on the failed ends of the SK-76 fibers are due to fibril snap back that occurred during failure. Therefore, fibrillation is still the mode of failure, despite the difference in appearance of these fibers.

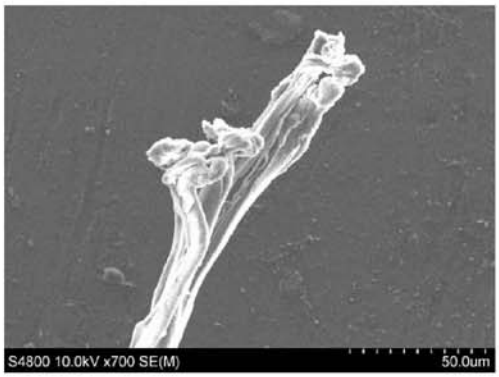

(a)

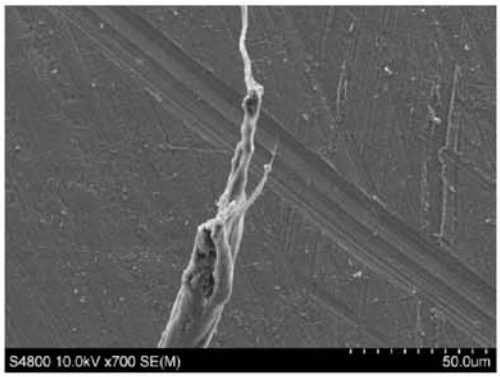

(b)

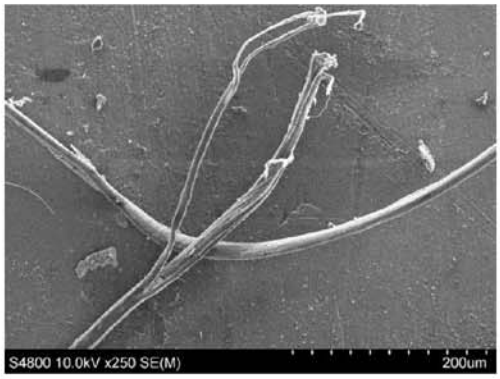

(c)

A 25: SEM image of Dyneema® SK-76 fiber failure for three fibers with the round indenter at 50°.

This balled appearance can also be observed at 50° as shown in Figure A25a, above. Here, there are two main sections with multiple balled up shapes, indicating that multiple smaller fibrils snapped back, not just a few main fibrils, as seen in Figure A24. Figure A25b and A25c, however, have a normal fibril appearance. This leads to the conclusion that failure mechanism for 50° is fibrillation.

A.2.3 FSP Indenter

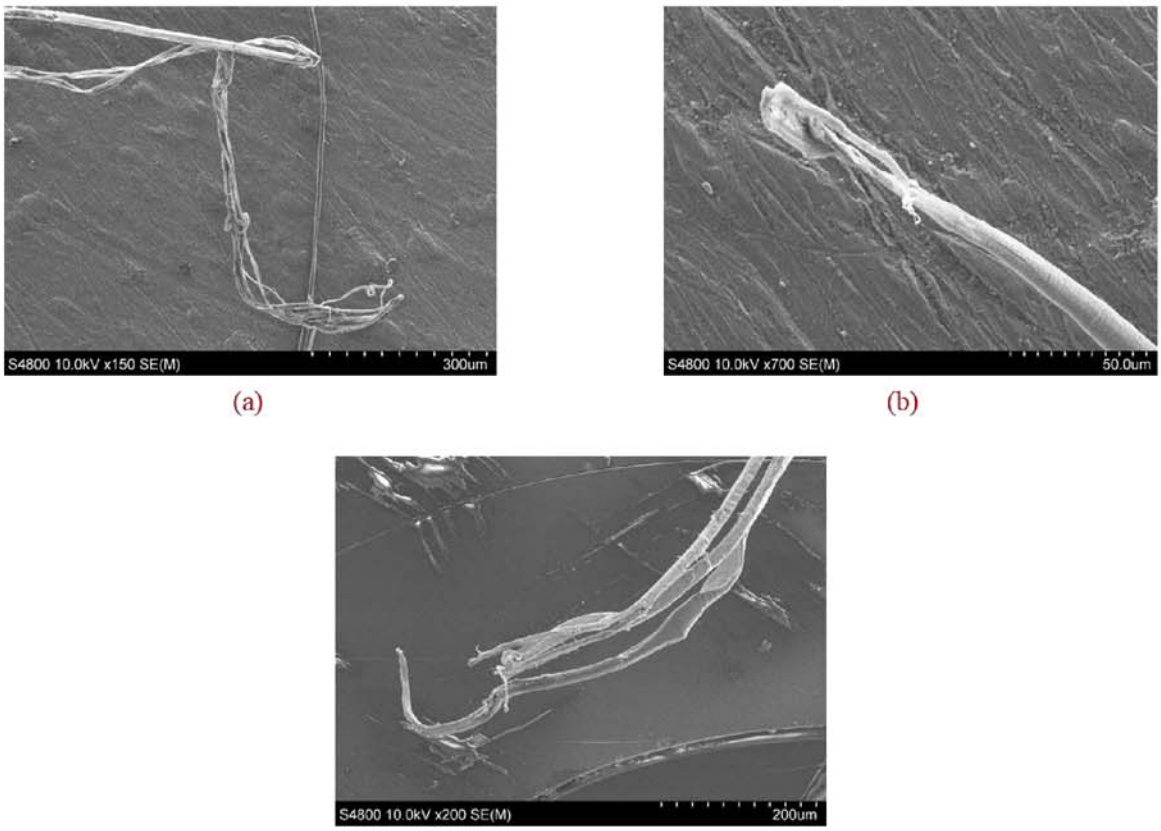

A 26: SEM image of Dyneema® SK-76 fiber failure for three fibers with the FSP indenter at 10°.

Using a FSP indenter at 10°, caused failure by fibrillation for Dyneema® SK-76 (Figure A26). All three images show this fibrillation, though in Figure A26b there is balling at the end of the fiber, most likely due to snap back that occurred at failure.

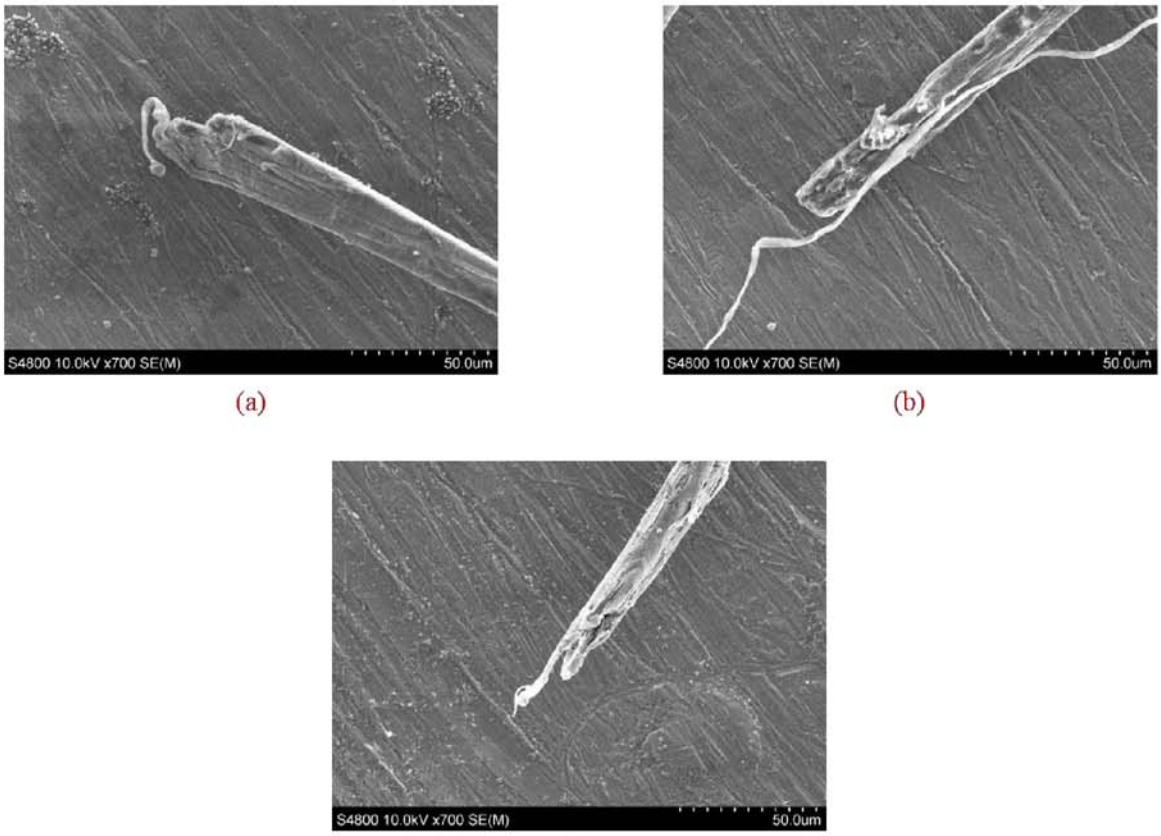

(a) (b)

(c)

A 27: SEM image of Dyneema® SK-76 fiber failure for three fibers with the FSP indenter at 20°.

At 20°, fibrillation is still present, though not as prominently as with the previous angle. As Figure A27 shows, fibrillation is present at the ends of the failed fiber, but there is a slight stretched look about the fibers, as well. Therefore, fibrillation is the main failure mechanism for SK-76 at 20°.

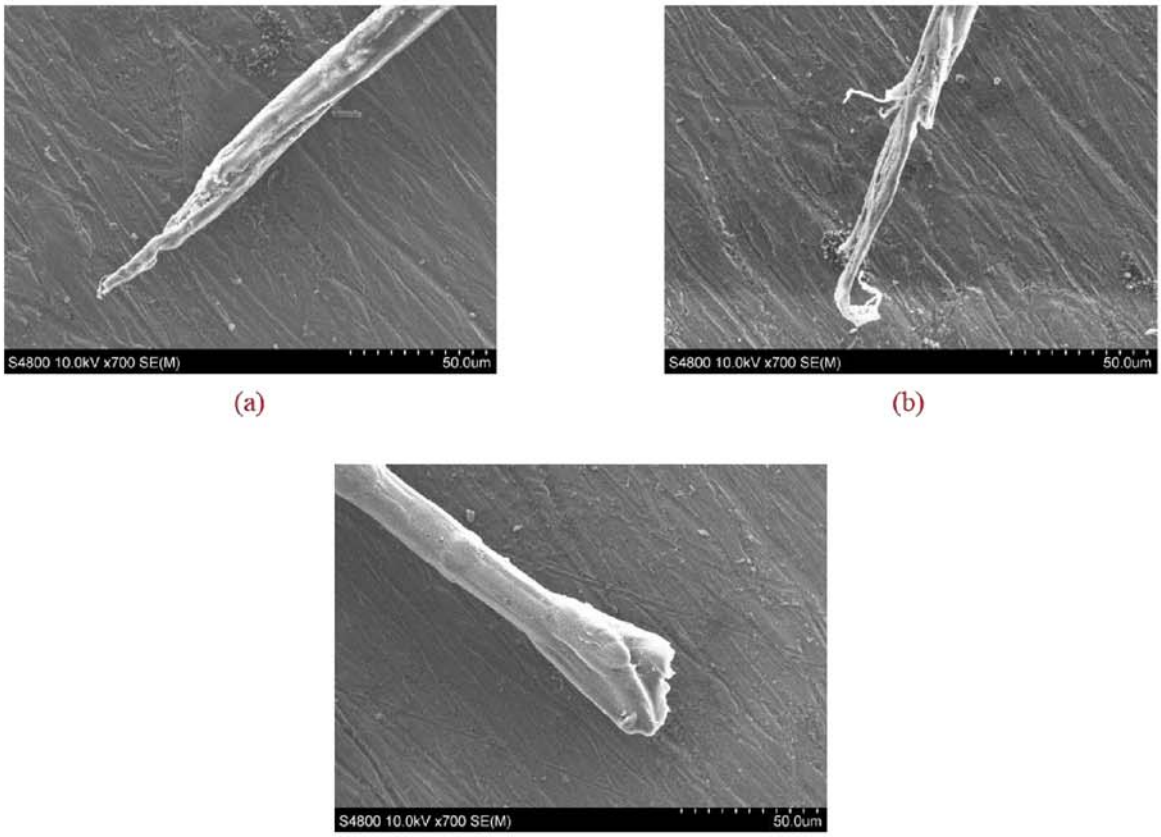

A 28: SEM image of Dyneema® SK-76 fiber failure for three fibers with the FSP indenter at 30°.

For FSP at a 30° angle, fibrillation is still the main mechanism of failure, although this is due more to thinning in the fiber than fibril separation, as seen in the 10° images above (Figure A28). Figure A28a and A28b show this thinning, with A28b having tiny fibrils protruding from the sides as well. Figure A28c, unfortunately, touched the superglue, giving the wide/flat end, and obscuring the failed end. However, it is expected that the fiber is similar to the fiber shown in Figure A28b, thus being consistent with the fibrillation failure mechanism observed.

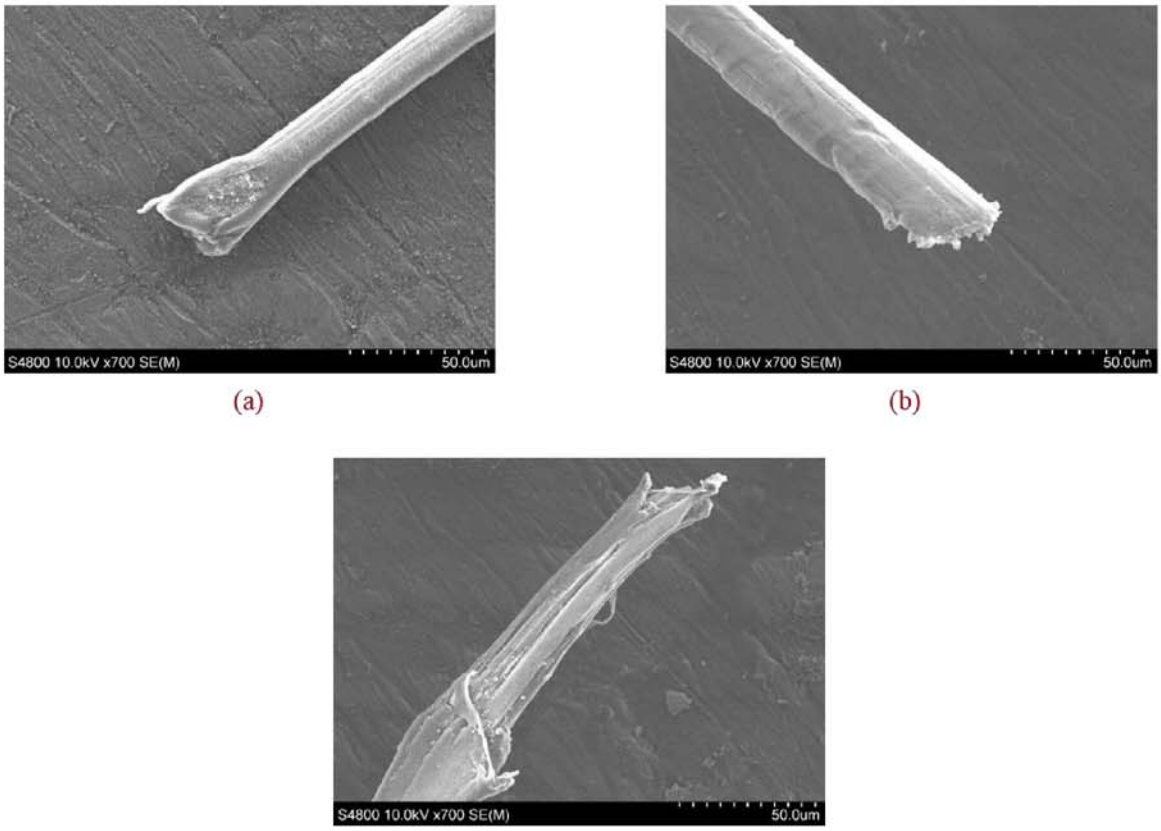

A 29: SEM image of Dyneema® SK-76 fiber failure for three fibers with the FSP indenter at 40°.

During the sample preparation at 40°, superglue also got on one of the fiber tips (Figure A29a). However, this did not obscure the failure mechanism, as it has previously (Figure A28c). For the fiber in Figure A29a, the superglue can be seen on the top surface, but the cut appearance is still readily observed. This is consistent with the other fibers imaged at this angle (Figure A29b and A29c). Therefore through thickness shearing is the failure mechanism at this angle.

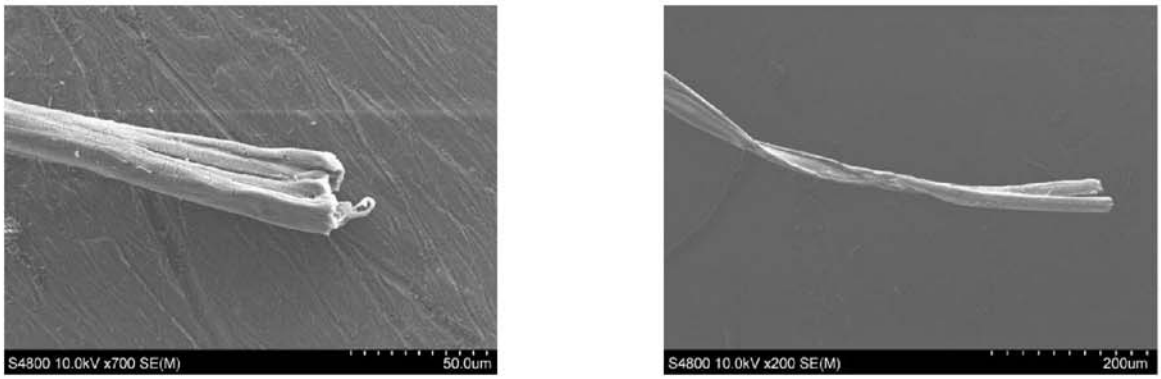

(a) (b)

A 30: SEM image of Dyneema® SK-76 fiber failure for two fibers with the FSP indenter at 50°.

For 50°, only two samples were provided (Figure A30). However, they both have sheared ends, with minimal cracking along the fiber axis. It can, therefore, be concluded that through thickness shearing is the failure mechanism for SK-76 with the FSP indenter at 50^0.

A.3 Zylon® 555 Fiber Failure

Zylon® 555 fibers were tested with the razor blade, round, and FSP indenters at angles between 10° and 50°. The failed ends of these fibers were then analyzed with a SEM to determine the failure mechanisms present.

A.3.1 Razor Blade

(a)

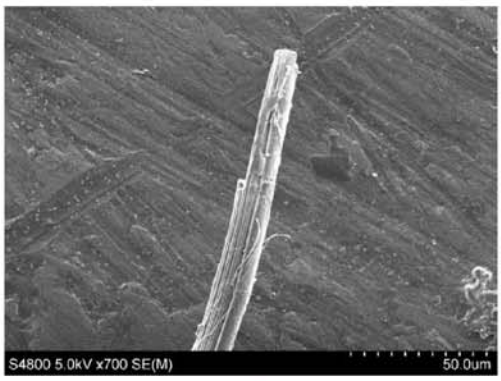

(b)

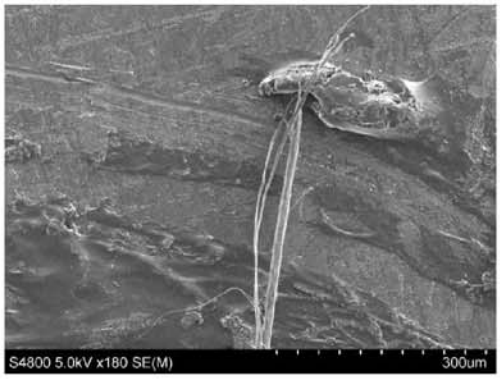

(c)

A 31: SEM image of Zylon® 555 fiber failure for three fibers with the razor blade at 10°.

The use of the razor blade indenter at 10° for Zylon® 555, caused multiple types of failure (Figure A31). In Figure A31a, the fiber exhibits partial shearing, with the skin layer still intact. Figure A31b shows fiber failure of only through thickness shearing, while Figure A31c shows fibrillation as the failure mode. Despite these inconsistencies, shear is the main mode of failure observed in these fibers, and therefore through thickness shearing is considered the main failure mechanism, though more testing should be done to confirm this.

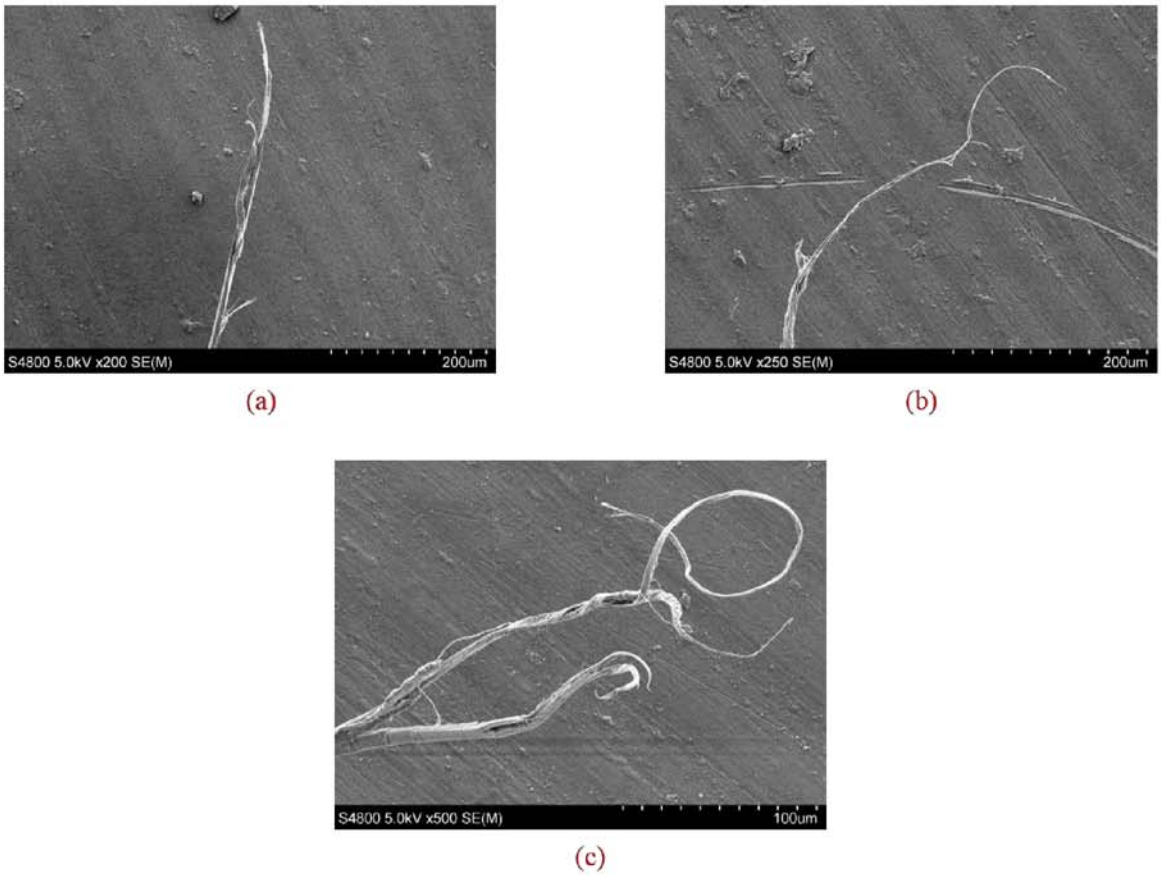

A 32: SEM image of Zylon® 555 fiber failure for three fibers with the razor blade at 20°.

Figure A32 contains the fiber results from the 20° angle testing. These results indicate that fiber thinning and fibrillation are the main failure modes observed. This is different that the observed results for KM2 and SK-76 previously discussed, and is also inconsistent with the rest of the results for Zylon® 555 discussed below.

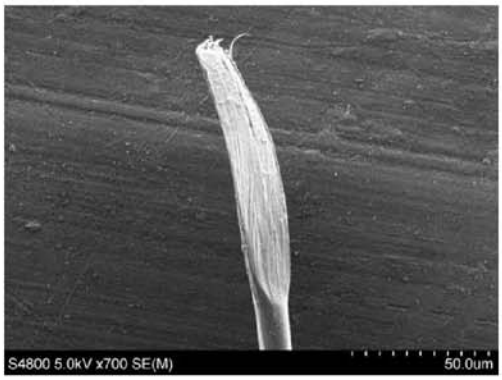

(a)

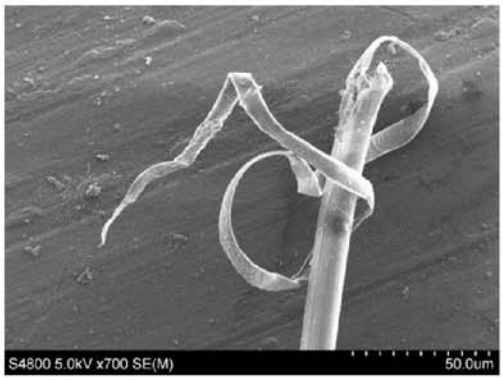

(b)

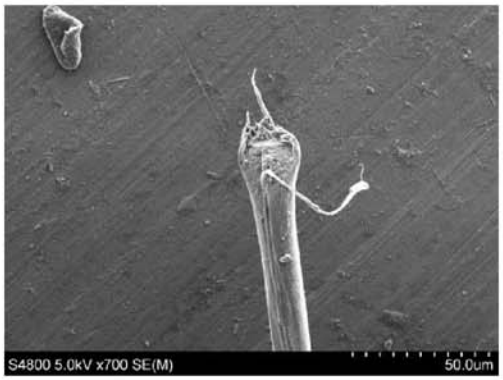

(c)

A 33: SEM image of Zylon® 555 fiber failure for three fibers with the razor blade at 30°.

For 30°, the fibers are observed to fail mainly by shearing (Figure A33). In Figure A33a, the failed fiber end has a peeled/scraped look to it, while Figure A33b has partial shearing with one, long fibril from the skin layer present. Figure A33c, however shows shearing with only the smallest of skin layer fibrils present. Regardless of these slight difference, the main failure mechanism observed is through thickness shearing.

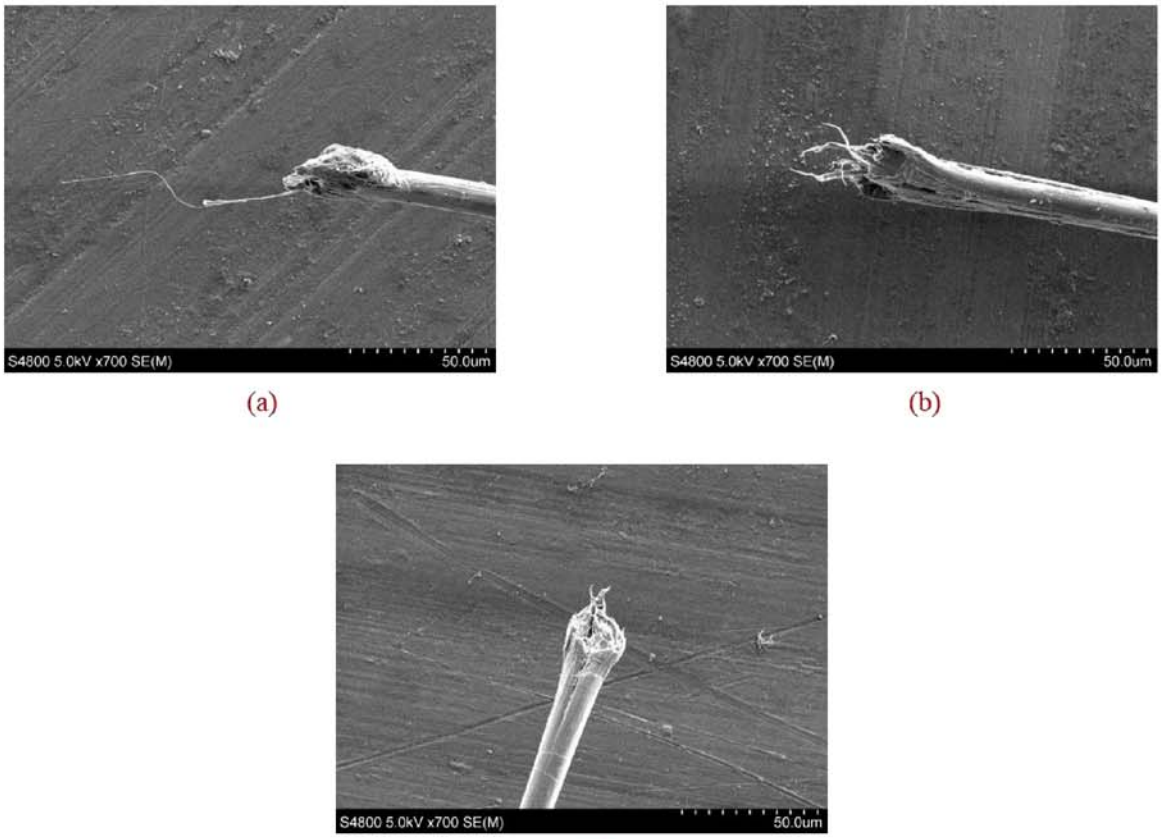

(a) (b)

(c)

A 34: SEM image of Zylon® 555 fiber failure for three fibers with the razor blade at 40°.

The 40° angle, however, produced very consistent results (Figure A34). As the images show, failure occurred due to through thickness shearing, with a small number of short, thin fibrils present at the failed end.

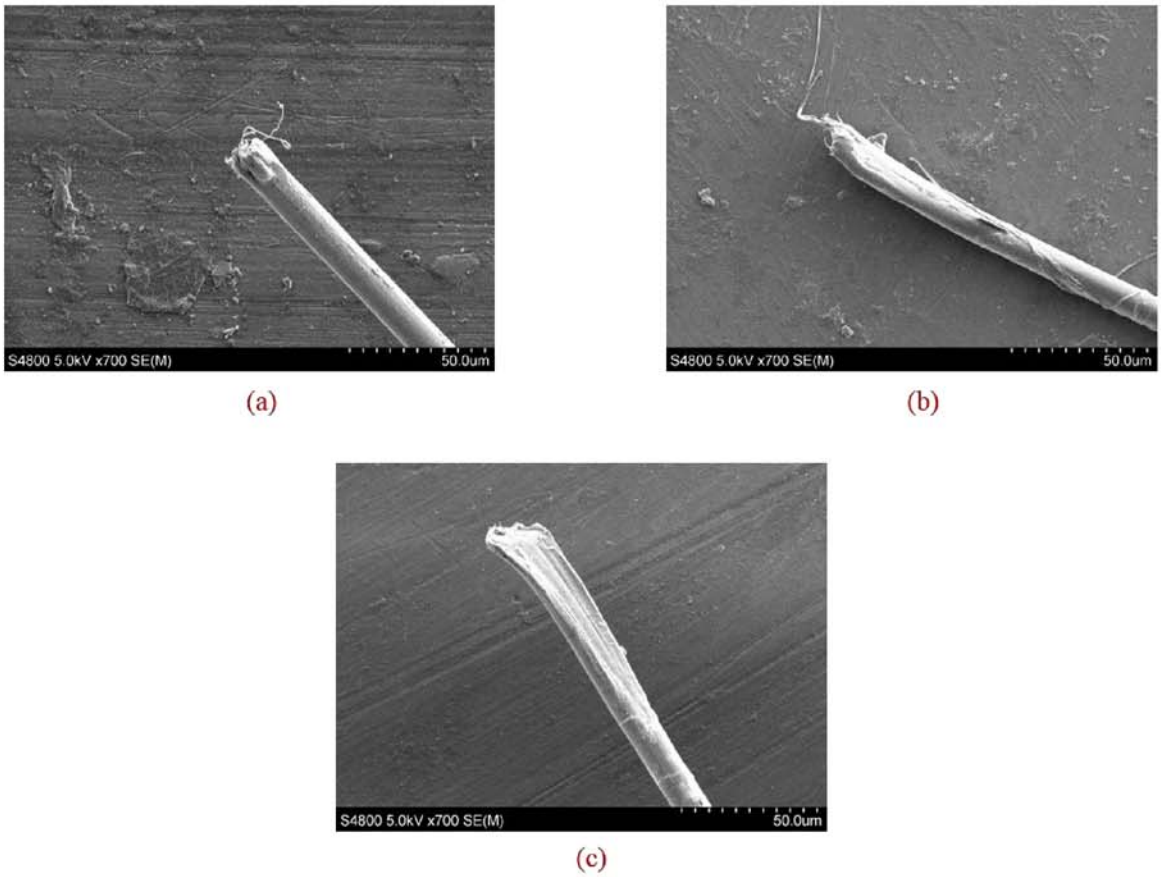

(a) (b)

(c)

A 35: SEM image of Zylon® 555 fiber failure for three fibers with the razor blade at 50°.

The results at 50°, were also quite consistent (Figure A35). Through thickness shearing is the main failure mechanism observed.

A.3.2 Round Indenter

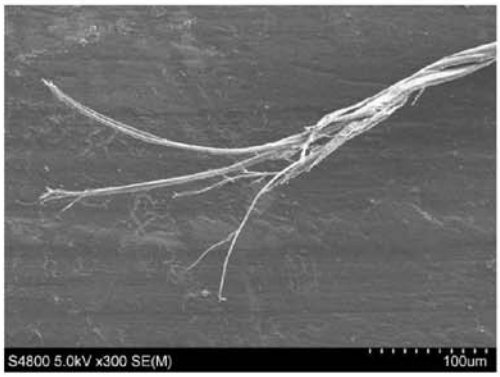

(a)

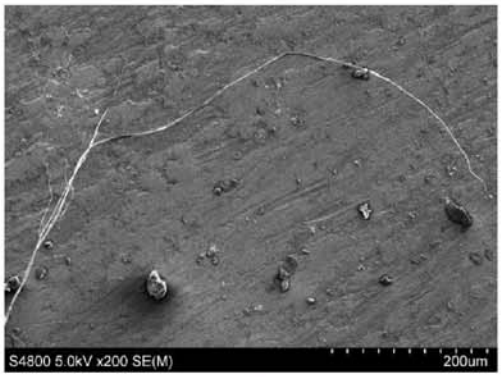

(b)

(c)

A 36: SEM image of Zylon® 555 fiber failure for three fibers with the round indenter at 10°.

The round indenter produced a difference in results for 10° (Figure A36). Figure A36a and A36b show fibrillation, while A36c shows what looks like shearing with a short, thick fibril with as slight curl towards the top of the image. In spite of this difference in failure, it was concluded that fibrillation was the predominant failure mode for this angle, though more testing should be done to confirm this.

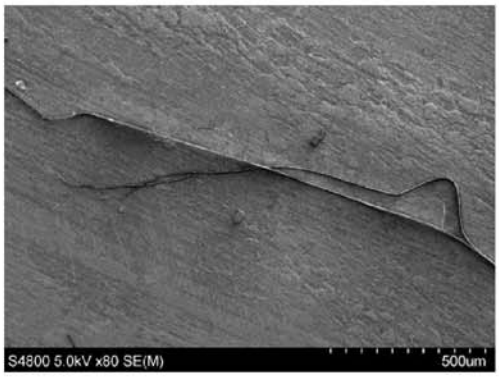

(a)

(b)

(c)

A 37: SEM image of Zylon® 555 fiber failure for three fibers with the round indenter at 20°.

For 20°, discrepancies were again observed within the failure modes. Figure A37a and A37b, both have fibrillation, though A37b also has kink band formation. Figure A37c, on the other hand, has a flattened look, with a small fibril present along the top of the fiber. Fibrillation was concluded to be the main failure mechanism, even with the discrepancies observed.

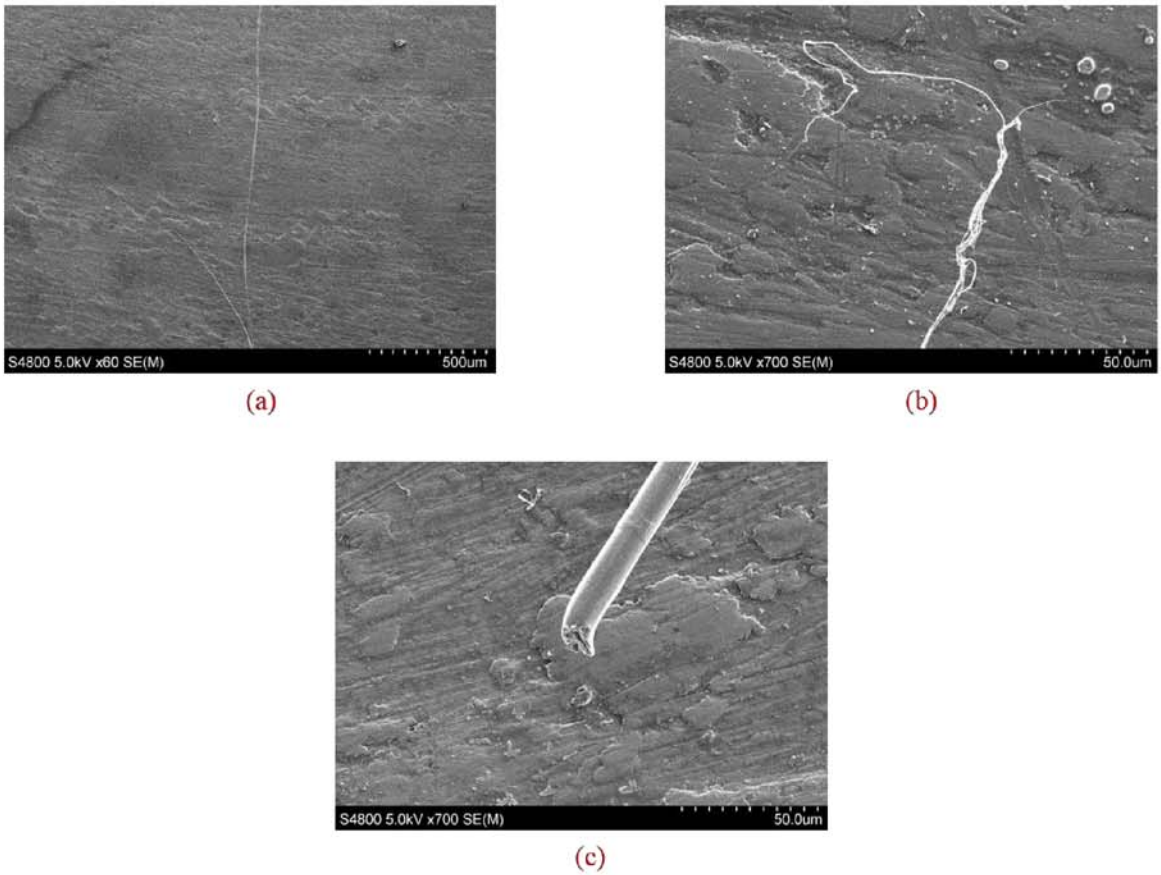

A 38: SEM image of Zylon® 555 fiber failure for three fibers with the round indenter at 30°.

There were also inconsistencies within the fibers tested at 30° (Figures A38). Figure A38c does show only through thickness shearing as the cause of failure, but A38a and A38b both show only fibrillation for failure. Therefore, fibrillation was concluded to be the main failure mechanism for this angle.

(a)

(b)

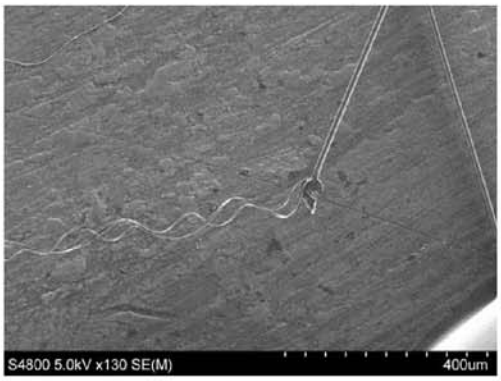

(c)

A 39: SEM image of Zylon® 555 fiber failure for three fibers with the round indenter at 40°.

Once again, inconsistencies in failure modes were observed in the fibers, this time at 40° (Figure A39). In Figure A39a, the fiber has a cut appearance, while A39b has fiber failure due to thinning as well as a small amount of fibrils. The fiber failure in Figure A39c presents with fibrillation of the skin, as well as a slightly crushed/flattened appearance. Given the similarities in Figure A39b and A39c, it was concluded that fibrillation was the main failure mode at this angle.

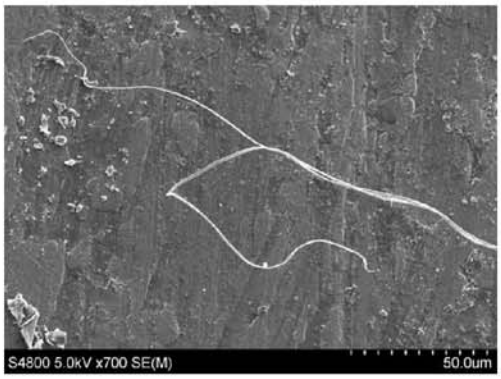

(a)

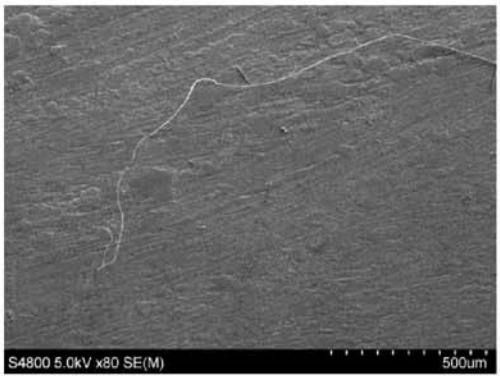

(b)

(c)

A 40: SEM image of Zylon® 555 fiber failure for three fibers with the round indenter at 50°.

For 50°, there is more consistency in the results (Figure A40). All the images show fibrillation as the failure mode, though Figure A40c contains fibril snap back (balling), while A40a and A40b do not. Regardless, fibrillation is the main failure mode for the 50° testing angle.

A.3.3 FSP Indenter

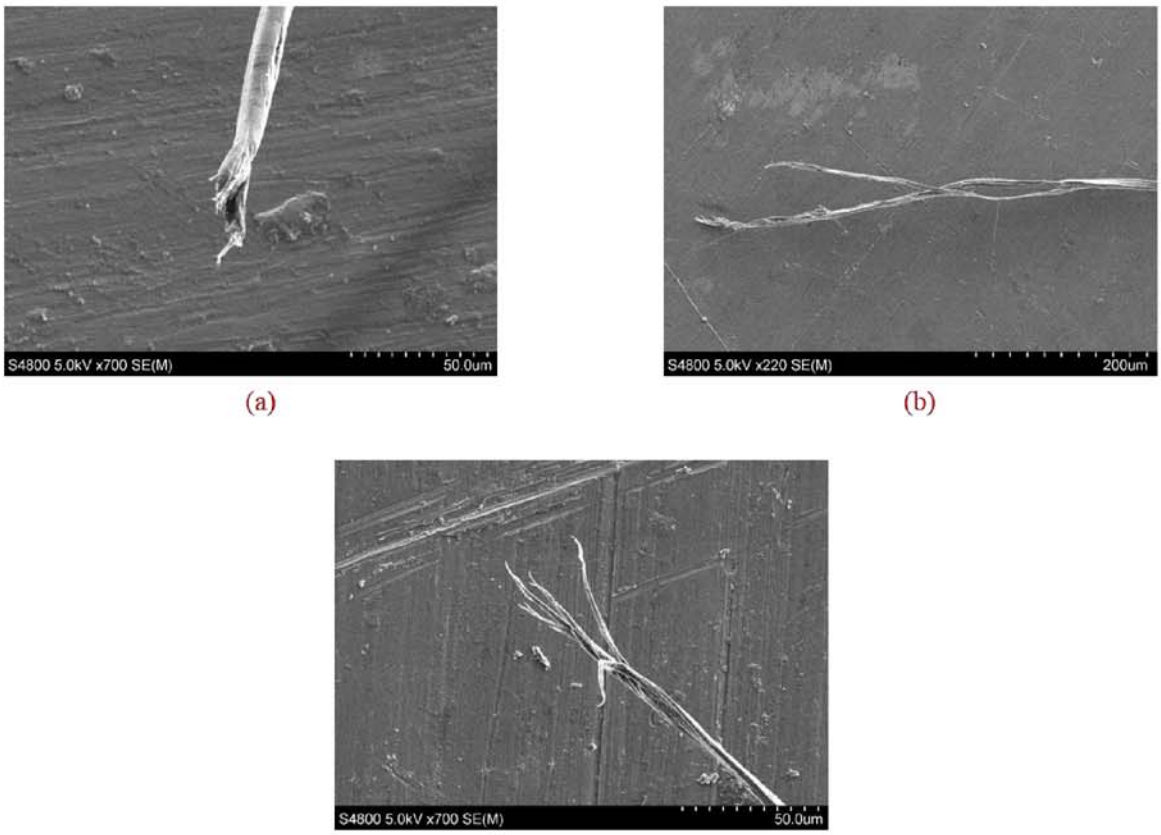

A 41: SEM image of Zylon® 555 fiber failure for three fibers with the FSP indenter at 10°.

For Zylon® 555, the FSP indenter caused varying degrees of fibrillation at the 10° angle (Figure A41). Figure A41a shows short, stubby fibrillation at the failed end, while in A41b the fiber split into two main fibrils, each with smaller and thinner fibrils extending off the ends. Figure A41c, however, has fibrils consistent in size at the end, giving the appearance of a broom. Regardless of the difference in fibril appearance, fibrillation is clearly the failure mechanism for this angle.

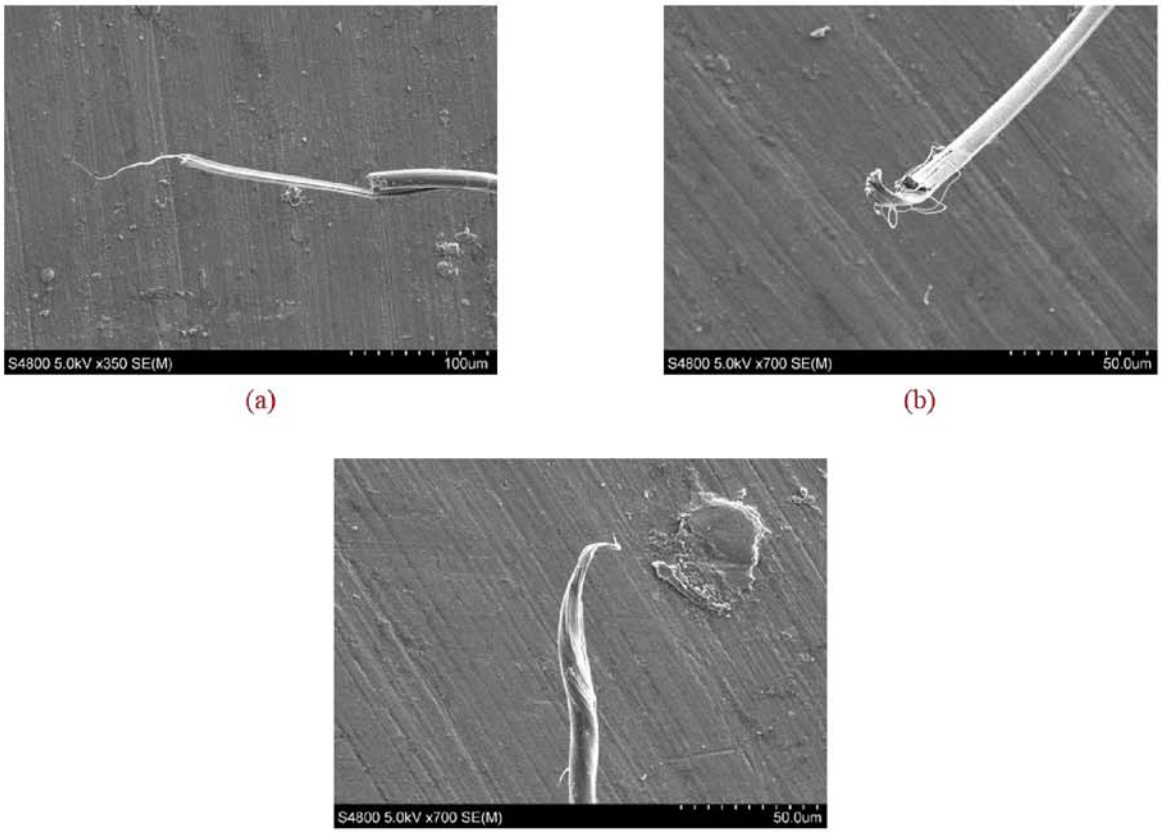

(a) (b)

(c)

A 42: SEM image of Zylon® 555 fiber failure for three fibers with the FSP indenter at 20°.

At 20°, the failure is slightly inconsistent. Figure A42a and A42b show partial through thickness shearing, with fibrillation occurring within the skin layer. However, Figure A42c shows thinning and a slight twist to the fiber, indicating that fibrillation is the failure mode. Since the majority of the images show a part shearing, part fibrillation failure mode, that is concluded to be the failure mechanism at this angle.

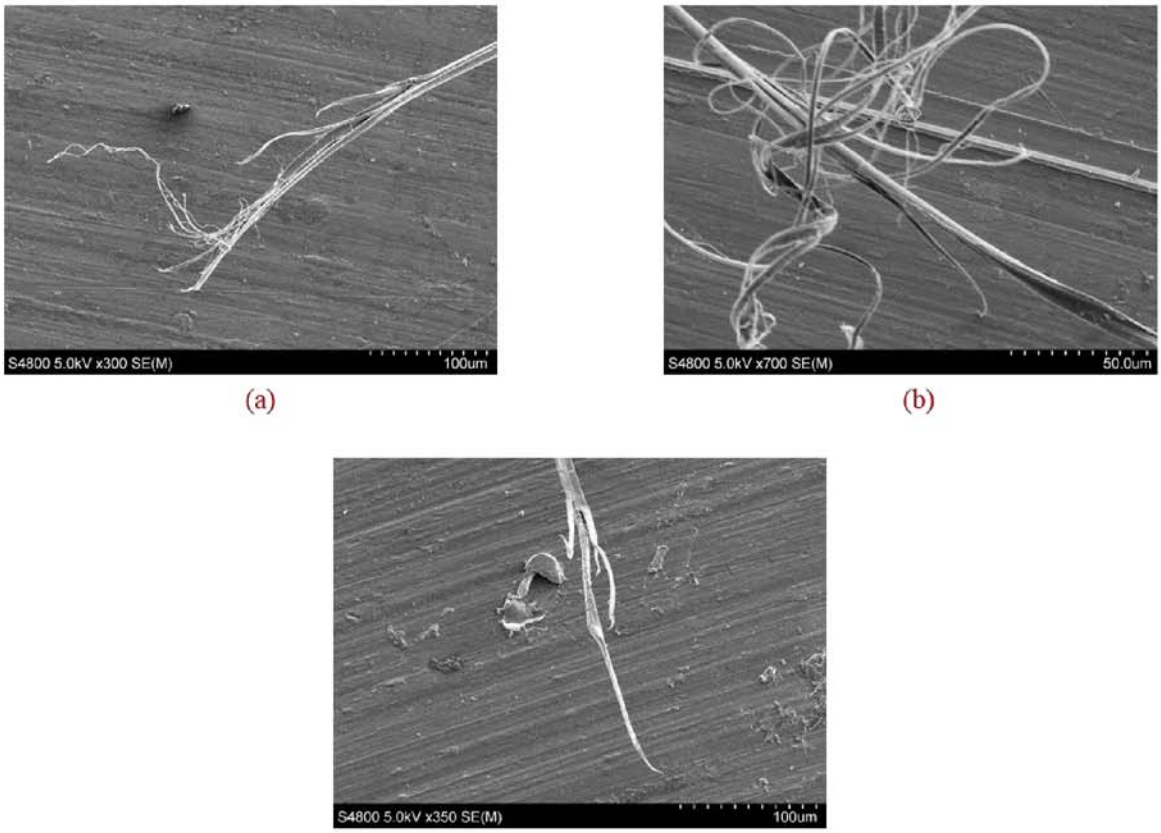

A 43: SEM image of Zylon® 555 fiber failure for three fibers with the FSP indenter at 30°.

At 30°, fibrillation is the failure mechanism observed, even more so than at the 10° angle (Figure A43). While this is made clear in the images, it is an unexpected result, and is inconsistent with the rest of the results gleaned from the other angles; it doesn't fit the pattern of transition from fibrillation to through thickness shearing. This angle should be redone, to see it these results are correct, or if some error occurred during the testing.

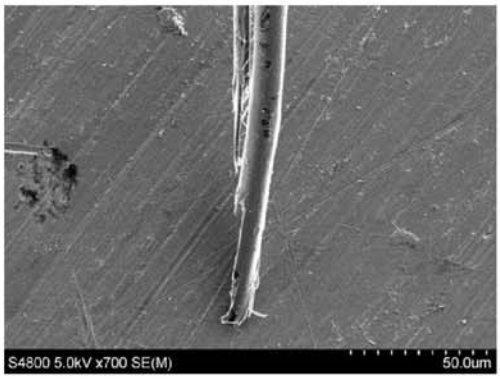

(a)

(b)

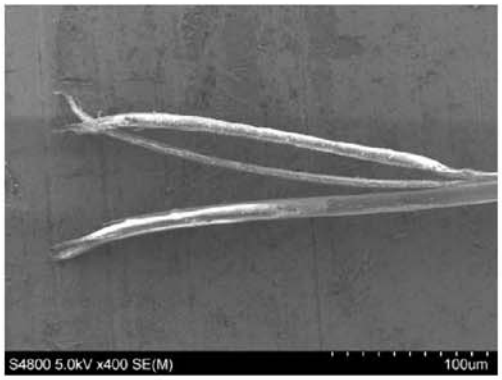

(c)

A 44: SEM image of Zylon® 555 fiber failure for three fibers with the FSP indenter at 40°.

For 40°, the fibers, once again, show inconsistency in failure (Figure A44). In Figure A44a and A44b, there is a cut look, with some fibrillation present, while in **c** there is fibrillation, with the ends of each fibril showing a slightly cut look. It was therefore concluded that the main failure mechanism is through thickness shearing, with a small amount of fibrillation present, since that is what the majority of the fibers showed.

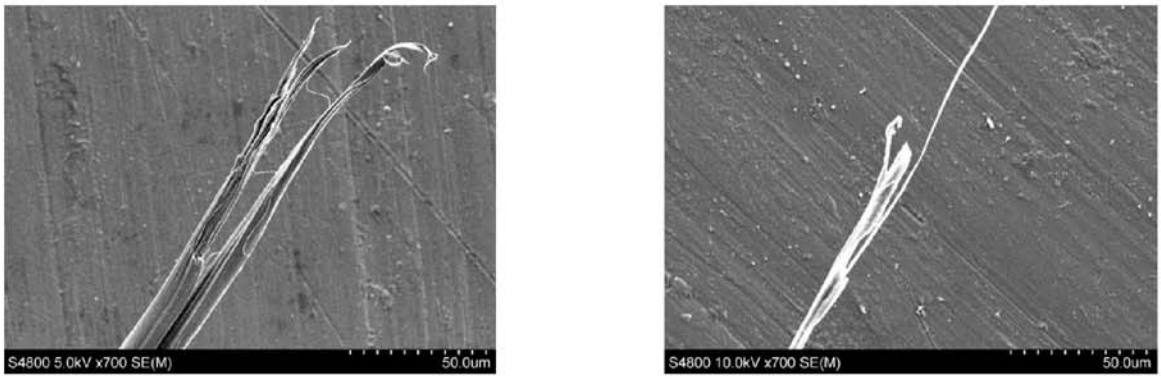

(a) (b)

A 45: SEM image of Zylon® 555 fiber failure for two fibers with the FSP indenter at 50°.

At 50°, only two fibers were available for imaging, and these show a splintered appearance, with slight fibrillation (Figure A45). Using these images, as well as the data from Part I, it was concluded that failure occurred due to incomplete through thickness shearing, with a small amount of fibrillation at the skin layer.